Computational and Physical Modelling on Saemangeum Closure Works

Report EX 4640
September 2002

Computational and Physical Modelling on Saemangeum Closure Works

Report EX 4640
September 2002

HR Wallingford

Address and Registered Office: HR Wallingford Ltd. **Howbery Park, Wallingford, OXON OX10 8BA**
Tel: +44 (0) 1491 835381 Fax: +44 (0) 1491 832233

Registered in England No. 2562099. HR Wallingford is a wholly owned subsidiary of HR Wallingford Group Ltd.

Contract - Consultancy

By a contract with the Rural Research Institute (RRI) of the Korea Agricultural and Rural Infrustructure Corporation (KARICO) dated 19th April 2002, HR Wallingford undertook to carry out computational and physical modelling of the Saemangeum Closure works. The representative of RRI was Dr Eo, Daesu. Mr Jonathan Simm, Technical Director for Engineering, was the HR Wallingford Project Manager. The computational modelling was carried out under the supervision of Dr A J Cooper of the Hydrodynamics and Metocean Group. The physical modelling was carried out under the supervision of Mr M A Littlewood of the Estuaries and Dredging Group. HR Wallingford's job number for the project was CDR3268.

Prepared by ....

(name)

....

(Title)

Approved by ....

(name)

....

(Title)

Authorised by ....

(name)

....

(Title)

Date ....

Summary

Computational and Physical Modelling on Saemangeum Closure Works

Report EX 4640
September 2002

HR Wallingford was commissioned by The Rural Research Institute of the Korea Agricultural and Rural Infrastructure Corporation to carry out various studies relating to the final closure of the Seamangeum project offshore dikes currently under construction on the western coastline of South Korea. In addition to the numerical modelling of the complete closure works, reported separately, a schematised physical model of one of the closure gaps was constructed to investigate the flow regime during the final 100m of dike closure.

Contents

Tables

Figures

Contents *continued*

Contents continued

Plates

Appendices

1. INTRODUCTION

By a contract with the Rural Research Institute (RRI) of KARICO dated 19th April 2002, HR Wallingford undertook to carry out computational and physical modelling of the Saemangeum Closure works.

The Saemangeum project comprises the construction of 33 km of sea dikes, which will enclose an area of reclaimed tidal flats of 282.4km^2 and a desalinised reservoir of 117.6km^2. During the closure of the dikes, very high flows will develop through the gaps. Studies carried out at RRI anticipate that these could exceed 6 m/s. The purpose of the consultancy services is to resolve the hydraulic conditions around the open section, using state of the art computational models, and to review the stability of the bed protection in the gaps and at the heads of the dike embankments.

The first phase of work involved the setting up and calibration of the TELEMAC flow model of the area around Saemangeum and the carrying out of an agreed 3 tests using the model. In an interim report, the substance of which is also included in this report, HR Wallingford examined and concluded on three Scenarios proposed by KARICO, recommending that one of the three gaps in the dike should be closed early (say 2003 rather than 2006).

During the period of this study, Mr Y.W. Park attended HR Wallingford for a period of 3 weeks training in the use of TELEMAC (27th May to 15th June inclusive). As part of this training, Mr Park was involved in discussions and work on the modelling described in this report.

Following approval of the interim report, HR Wallingford were provided by KARICO with the proposed final closure of the remaining two gaps and then conducted both numerical and physical modelling on the final closure procedures examining both velocities and stability of bed protection and dike materials.

A draft final report was submitted to KARICO in September at the commencement of a visit by Mr Simm of HR Wallingford. During this visit Mr Simm presented a seminar on the studies by HR Wallingford and answered questions from attendees, including representatives from RRI, from the Saemangeum project office and from KARDI.

This final report commences with descriptions of the computational modelling methodology and results in Chapter 2. The physical modelling is similarly described in Chapter 3. In Chapter 4, an engineering interpretation of the results is provided, taking account of the strengths and weaknesses of both physical and computational modelling approaches. Conclusions and recommendations are then provided in Chapter 5. All figures can be found at the rear of the report, followed by appendices describing the computational models.

2. COMPUTATIONAL MODELLING

2.1 Model set up and calibration

2.1.1 The area covered

The area covered by the TELEMAC model is shown in Figure 2.1, with co-ordinates referred to the UTM system. It includes the Kumgang estuary, the reclamation areas of the Kunsan Industrial Complex Zone, and the Janghang Industrial Complex Zone, together with the Saemankeum barriers. To the north, the model extends as far as Anmyondo Island, and to the south, as far as the inlet at Kumjongsan.

In order to prevent any distortion to the flow, the seaward boundary is well removed from the area of interest, and was chosen to coincide with the positions where boundary conditions are well known (see below).

The present modelling has been carried out in two dimensions as 3D flows are only expected to be significant during the final closure phases.

2.1.2 The model mesh

The average mesh spacing in the area of interest is approximately 500m, but in the immediate vicinity of the gaps, it is much finer, down to about 25m in some cases. Towards the model edge, the spacing widens to the order of 3000m. This can also be seen in Figure 2.1.

2.1.3 Bathymetry

The original model bathymetry was taken from a previous model (Delft model), and additional survey data in the region near the barriers was provided by the client (in the form of AutoCAD drawings). A detail of the bathymetry is shown in Figure 2.2. All levels are referred to mean sea level (MSL) as this is the convention used in the Client's data.

2.1.4 Boundary conditions

Boundary conditions at the seaward limit of the model were applied using tidal harmonics. These harmonics were supplied by the client, from observations made at 46 positions around the perimeter of the model area. 25 of these locations were chosen to apply boundary conditions, with 21 tidal constituents being used at each location.

A preliminary test was made by comparing the elevations generated by the model with those calculated from an additional set of harmonics for the year 2001, also supplied by the client.

2.1.5 Flow model calibration

The flow model was calibrated against five sets of field data, all obtained during the 9th and 10th of April, 2001. Tidal elevations during this period were recorded at Kunsan Outer Port, and at a position labelled WLR7, on the north coast of Sinsi Island, close to the junction with the barrier. Current measurements were made at a position in the middle of each gap. All of these positions are shown in the higher resolution view of Figure 2.3.

This period of time included tides of range similar to that of the maximum spring tides – we estimate that during the course of a year only about 20 tides would have amplitudes greater than or equal to the test case tides of 9/10 April 2001.

The model calibration is presented for runs with a bed roughness coefficient of 0.01m and using the Elder formula to describe the turbulent viscosity (the Elder formula gives a value for the turbulent viscosity that depends varies in proportion to the product of the local current speed and water depth). Within the gaps, the raised sills are assigned a local bed roughness coefficient of 1.0m, to represent the scale of the rocks used in building them up.

The model was started at midnight on the 9th April, and run for a period of approximately two tides before the comparison with field data was made. The calibration plots are shown in Figures 2.4 to 2.8. The tidal levels show very good agreement indeed, and the currents in the gaps are well within the tolerances normally associated with numerical models.

In carrying out the calibration, fully slip boundary conditions were applied on all parts of the sea dykes.

Figures 2.9 and 2.10 show vector plots of the currents at the peak flood and ebb tides.

We considered it was unnecessary to calibrate the model against other tides because we had selected one of the more extreme and thus more onerous tides for the calibration process. The model had all tidal constituents embedded within it and hence once calibrated for spring tides should represent neap or other tides accurately.

2.2 Tests to select overall closure strategy

2.2.1 The test conditions

Several different sets of test conditions have been defined. They are summarised in the table below. (Measurements in metres; 'depth' denotes sill depth below MSL.)

Test	Gap 1 width, depth	Gap 2 width, depth	Gap 3 width, depth	Garyeok sluices	Sinsi sluices
calibration	2500, 10	1300, 23	3600, 6.8	closed	closed
0	1600, 10	1100, 16	1800, 6.8	open	open
1	1600, 10	1100, 16	closed	open	open
2	closed	1100, 16	closed	open	open

The 'calibration' case reflects the situation at April 2001, when the calibration with the field data was made. At this time, Gap 1 was 2500m wide, and the bottom was built up to a maximum depth of 10m. In places, the water was shallower, due to variations in the natural bathymetry. The width and depth for Gaps 2 and 3 may be seen from the table. There were no sluice gates open at this time.

Test 0 is a preliminary case to the main tests. Here, each gap (1 and 2) has the width and depth which will be correct for the later tests. Gap 3 has width and depth which will be representative of the long-term situation before it is filled in. Both sets of sluices are opened.

Test 1 has Gap 3 closed, but is otherwise identical to Test 0.

Test 2 has Gap 1 closed also, but is otherwise identical to Test 1.

For all of the tests 0,1 and 2 fully slip boundary conditions were applied on all of the sea dykes.

2.2.2 The test results

Plots of current speed and water level are shown for each gap in Figures 2.11 to 2.13, for tests 0, 1 and 2. As one would expect, the currents increase as the gaps are closed. By the condition of test 2, the peak value has reached 6.5 m/s on the ebb tide. The result for test 0 is not the same as that reported in the interim report for the current speed at gap 3. This resulted from the change of the sill level from –8m to –6.8m and from the fact that in the case reported here the extra friction along the sill that was applied in gaps 1 and 2 and previously in gap 3 was not applied in this simulation. When this version of test 0 was run again with the same friction in gap 3 as before then the result was closer to the earlier result.

Figure 2.14 shows the profiles of the distribution of maximum velocity across each gap - these plots do not correspond to a particular time; rather, the highest value found at any time during the run is shown for each point in space. The horizontal axis is calibrated as the distance along the gap, starting from the south end. The profiles are quite flat, tailing off towards either end, but reveal that there exists a higher maximum velocity in Gap 2 - the value reaches 6.8 m/s during Test 2.

Figure 2.15 plots the maximum velocity along lines perpendicular to the gaps, running in the on-shore direction. Figures 2.16 to 2.24 are vector plots of the current velocity at the times of peak flood and ebb, and colour contour plots of the maximum speed.

2.3 Tests on final closure of gaps 1 and 2

Further 2D simulations have been run representing different stages of the closure of gaps 1 and 2. The following table gives the size in metres of gaps 1 and 2 for each test (gap 3 is closed in all cases).

	Test 3	**Test 4**	**Test 5**	**Test 6**	**Test 7**	**Test 8**	**Test 9**
Gap 1	1300	800	500	100 neap	560	200	50 neap
Gap 2	850	700	500	100 neap	310	200	50 neap

The mesh used for these runs was usually the same as that used for Test 0. The extra walls were modelled by raising the bathymetry to 4m. MSL

The resolution of the models in the gaps was as follows:

- Usually 30m or 35m in the direction of the flow (true for all cases) and 50m perpendicular to the flow.
- 100m gaps had a spacing of 25m perpendicular to the flow
- 50m gaps has a spacing of 12.5m perpendicular to the flow.

In carrying out these closure tests the model was run using a slip boundary condition for the gaps in the sea dykes. However, at the ends of the wall the shape of the partially constructed sloping sea wall was represented so that the water was in contact with the slope of the dyke. At this location the water depth is zero and consequently the current velocity must also be zero. In this way an effective no-slip boundary condition was experienced by the water in the model, although a no-slip boundary condition was never implemented in the model. This feature did not occur in the calibration or tests 0,1 and 2.

Because it appeared that the effectively no-slip boundary condition at the ends of the gaps affected the current speeds the runs of some test cases were repeated using a slip condition (vertical rather than sloping walls so depths of zero were not encountered in the gaps). The comparison of these results is shown in Figures 2.37 to 2.40. The effect on the current near to the centre of the gap is summarised in the following table

Gap width	**Gap No**	**Maximum current near to centre of gaps**			
		flood no slip	**slip**	**ebb no slip**	**slip**
500m	gap 1	7.2	7.0	8.0	6.6
	gap 2	7.3	7.0	7.8	7.5
100m	gap 1	5.2	5.0	5.9	5.6
	gap 2	5.3	5.1	6.1	5.8

The change to the result due to the use of the slip condition is to make the pattern more uniform across the gap on the ebb in the 500m gap case with higher currents than before near to the ends and lower currents in the centre of the gap. For the 100m gap the differences are less marked. In this case the effect of the side slopes in the slip case makes the total gap width greater than 100m. Although the results were affected by the change to a slip condition the local maximum expected of the current at the ends of the gaps was still not found. A sensitivity test to the model resolution was attempted in case the reason was that resolution was inadequate to show the local maxima near to the ends of the gaps. The result was not noticeably changed by this.

So a further test was carried out. In the original set of tests the recommended scheme for advection of momentum (the characteristic scheme) was used. This scheme is known to be first order accurate and therefore numerical viscosity is present in the solution. The TELEMAC scheme that overcomes the numerical viscosity is a finite element advection scheme known as Streamwise upwind Petrov Galerkin (SUPG). By implementing this scheme for the advection of momentum we found that local maxima did sometimes appear near to the ends of the gaps. However the model runs were insufficiently stable to run for a whole simulation, errors built up near to the model seaward boundary and eventually the runs failed.

Comparisons of the results with slip condition and the SUPG run (during the period before it failed) are shown for the 500m gaps, spring tide run in Figure 2.41. This shows the desired greater current near to the ends of the gaps, and also shows a lack of symmetry with a higher current at one end of the gap compared with the other.

The tables below show maximum speeds over time for each test from the original tests. Values are given at the North, middle and South parts of the gaps, as well as the maximum average values over the width of the gap. The units are metres per second. The first table shows values for the calibration run and test 0. The second table shows values for tests 1 to 9. The final closure tests with a gap of 100m and 50m will exist as stages during the final two days when neap tides are expected.

		Gap 1				Gap 2				Gap 3			
		Ave	Nor	Mid	Sou	Ave	Nor	Mid	Sou	Ave	Nor	Mid	Sou
Cal	Fld	2.81	2.01	3.07	2.76	2.21	1.68	2.42	2.72	2.20	2.49	2.08	1.93
	Ebb	2.27	1.71	2.35	2.28	1.76	1.40	1.92	1.77	2.04	2.11	2.03	1.96
Test 0	Fld	3.44	2.73	4.06	3.68	3.84	3.31	4.18	2.81	3.36	3.20	3.48	2.67
	Ebb	2.97	2.19	3.83	2.01	3.47	2.60	3.84	2.32	3.63	3.19	4.48	3.21

		Gap 1				Gap 2			
		Average	North	Middle	South	Average	North	Middle	South
Test 1	Flood	3.94	3.10	4.58	4.16	4.65	4.08	5.00	3.23
	Ebb	3.74	2.72	4.75	2.60	4.68	3.29	5.28	2.87
Test 2	Flood	closed	closed	closed	closed	6.13	6.03	6.88	4.45
	Ebb	closed	closed	closed	closed	6.08	4.51	6.58	4.14
Test 3	Flood	4.52	3.58	5.58	4.60	4.94	4.02	5.88	3.44
	Ebb	4.52	3.51	5.94	3.41	5.21	3.56	6.21	3.98
Test 4	Flood	4.94	4.51	6.54	4.48	5.37	4.19	6.49	3.99
	Ebb	5.00	3.79	6.93	4.44	5.75	4.08	7.05	4.64
Test 5	Flood	5.38	5.12	7.21	4.86	5.57	5.15	7.27	4.41
	Ebb	5.76	4.02	8.03	5.19	5.90	4.53	7.83	5.50
Test 6 neap	Flood	4.60	4.03	5.17	3.93	4.69	3.84	5.26	4.25
	Ebb	5.51	4.25	5.85	4.66	5.47	4.37	6.09	4.84
Test 7	Flood	5.73	5.55	7.97	4.63	5.27	5.78	7.40	5.03
	Ebb	6.20	4.77	7.98	5.66	5.47	5.17	7.98	6.06

		Gap 1				Gap 2			
		Average	North	Middle	South	Average	North	Middle	South
Test 8	Flood	6.46	5.37	7.48	4.82	6.99	6.03	7.60	5.59
	Ebb	6.96	5.53	7.91	6.71	7.09	5.35	8.26	5.86
Test 9 neap	Flood	4.74	3.95	5.01	3.41	5.14	4.30	5.33	3.76
	Ebb	5.48	4.38	5.65	4.45	5.78	4.61	6.04	4.83

A number of 3D simulations were performed. Two spring tide simulations were performed, one with gaps 1 and 2 of width 500 m, the other with 100 m gaps. Also, a neap tide simulation was done with 100 m gaps. The results of the 3D model test runs are depicted in Figures 2.42 to 2.47. All of the runs carried out with the 3D flow model use free slip conditions at the ends of the gaps. From these figures it can be seen that there were no flow phenomena, such as extra circulations in either horizontal or vertical that appear in the 3D results but are absent from the 2D results. For this reason it is considered that the 3D simulations add no important extra information beyond the 2D modelling.

The following table gives maximum speed values for these 3D runs. The values shown are for the depth average current in each case.

		Gap 1				Gap 2			
		Average	North	Middle	South	Average	North	Middle	South
500 m Spring	Flood	5.4	5.5	6.2	5.0	5.6	4.6	6.2	5.4
	Ebb	5.8	4.7	7.3	5.8	6.8	6.7	8.0	5.8
100 m Spring	Flood	4.9	4.2	5.1	6.2	4.4	3.2	4.9	4.2
	Ebb	8.2	7.3	9.6	12.3	8.0	8.4	8.3	7.8
100 m Neap	Flood	5.2	4.6	5.4	6.7	4.8	3.5	5.3	4.6
	Ebb	5.9	5.4	6.2	7.4	5.6	5.6	6.1	5.2

In the event that the Saemangeum project office find that part of the final closure is likely to take place during intermediate tide conditions, interpolation can be made between the runs for 100m spring and 100m neap conditions.

3. PHYSICAL MODELLING

3.1 Introduction

HR Wallingford was commissioned by The Rural Research Institute of the Korea Agricultural and Rural Infrastructure Corporation to carry out various studies relating to the final closure of the Saemangeum project offshore dikes currently under construction on the western coastline of South Korea, approximately 200 km south of Seoul. On completion, the Saemangeum project will encompass an area of 400 km^2 in total, 280 km^2 of which will be reclaimed tidal flats and about 120 km^2 of desalinised reservoir. The location of the project is shown in Figure 1.1. In addition to the numerical modelling studies of the complete closure works, a schematised physical model of one of the closure gaps was constructed to investigate the flow regime during the final 100m of one of the dike closures. In the event Closure Gap No 2 was selected for modelling. This report describes the schematised physical model tests.

All dimensions given in this report are in prototype units unless specifically stated otherwise.

3.2 Model design and methodology

As gravitational forces predominate in this particular case, the physical model was designed to comply with Froude's similarity law, i.e. for all conditions the Froude number in the model being equal to the Froude number in the prototype ($F_r = V(gD)^{-½}$). The model was constructed to a natural scale of 1:50 resulting in the following scale relationships between model and prototype:

Length	1:50
Speed	1:7.0711
Discharge	1:17677.67

Scaling of the mass of the elements used in the model to represent the dike and bed protection layer was achieved using the following relationship:

$M_m = (F * M_p) / I^3$

Where M_p is the mass of the prototype element, M_m is the mass of the model element, I is the model scale and F is given by:

$F = ((\rho_p/\rho_s-1)/(\rho_m/\rho_f-1))^3 * (\rho_m/\rho_p)$

Where ρ_p is the density of the prototype rock, ρ_m the density of the model stone, ρ_s prototype water density and ρ_f the density of the water in the model.

This relationship makes suitable allowances for the density differences between the materials and the water in the both the model and prototype. It has been assumed that the rock used at Saemageum has a density of 2650 kg/m^3 and that the seawater has a density of 1025 kg/m^3. The model was filled with fresh water, density assumed 1000 kg/m^3, and the limestone chippings used in the model were known to have a density of 2710 kg/m^3.

To convert from the mass of the required elements to a size of limestone chipping required in the model the following relationship (Ref 1) was used:

$L = (1/0.87) * (M_m/\rho_m)^{\square}$

Where L is a typical size (m) of a model element of mass M_m kg and density ρ_m kg/m^3.

In the time available to carry out these tests it was not feasible to construct a model which accurately represented both the dike and adjacent bathymetry in the vicinity of Gap No 2. As a compromise it was decided that the physical model would have to be schematised and encompass as large an area as possible, whilst providing a good understanding of the flow regime and its impact on the integrity of the dike. The model was therefore constructed in a large basin that was capable of generating the longitudinal and consequential lateral flows, this being the flow along the dike wall caused by the flows ingressing to or egressing from the dike closure gap. Water was circulated around the basin by computer controlled axial flow pumps. The pumping system extracted water from a sump at the downstream end of the basin and returned the water into sumps at the upstream end. A temporary wall was built across the width of the basin. The floor of the basin upstream of the model dike was covered in a layer of shingle; this was to encourage full development of the flow in the approach to the dike. A 5 m (model measurement) gap was left in the middle of this temporary wall in which a 250 m length of the dike was modelled.

Only the construction phase of the dike was modelled. The core of the model dike was formed from concrete blocks and suitably sized limestone chippings used to complete the dike to the required profile. A 100 m long closure gap was left in the middle of the dike. The proposed bed protection layer downstream of the dike was also represented on the model using scaled materials. Figure 3.1 shows details of the schematised physical model. In Figure 3.1 the equivalent modelled mass of the elements used to construct the model dike are shown in brackets alongside that of the actual construction materials.

It was initially assumed that the gap in the dike would be closed using material that would be end-dumped from the top of the dike. In the absence of any further information the 1:1 slope at either end of the dike were formed with suitably sized limestone chippings representing previously dumped materials. A number of model elements representing this dumped material were manufactured from chippings enclosed in a “sack” of plastic mesh, these elements would be used in the tests to close the gap in the model in the absence of suitable rock equivalents. The scaled weight of these elements ranged from 3 to 7 tonnes with a median weight of 5.7 tonnes

Measurements in the schematised model were limited to water surface flow patterns, mean current speeds and water levels. A Braystoke BFM002 current meter aligned with the mean flow direction was used to measure current speeds. Single current speed measurements of the depth-mean speed were made at each point with the impeller set at the mean speed height, (a height of 40% of the total water depth). Water levels were measured relative to the floor of the basin. Surface flow patterns were recorded using floats and timed exposure photography from a camera mounted above the model. The camera was fitted with a flat field wide-angle lens to maximise the area covered whilst minimising distortion.

3.3 Model tests

Input flow for the physical model tests were obtained from the numerical model test results. It was initially decided that the worst condition that could be expected to occur would be at a time of peak current speed through the gap. The numerical model results for spring tide conditions with Gap No 2 closed to 100 m showed that the peak depth-averaged water speed in the gap occurred when the offshore water level was at approximately low water. Similar conditions were also established from neap tide numerical model tests. The test conditions are summarised in Table 3.1 as are the equivalent conditions simulated on the model.

The model was therefore set-up to reproduce the peak spring tide condition by estimating the required static water level in the model and adjusting the total pump discharge to give the required current speed in the gap. Increasing pump discharges was carried out slowly to prevent any possible damage to the modelled dike and gap. When the correct current speed in the gap was achieved the water levels in the model were then measured and compared to that required. This technique was repeated until the correct conditions were achieved. It was during these initial setting-up tests that it was found that there was flow through the model dike, resulting in a current speed of approximately 0.3 m/s close to the surface immediately downstream of the structure. This was thought to be totally unrepresentative of likely prototype conditions. Modification was therefore made to the model to minimise the through-dike flow.

When the correct model conditions were achieved a series of measurements of the current speeds and water levels were made on a three by three matrix of positions, with a separation of 50 m, around the gap. In addition a photographic record was made of the surface flow patterns in the vicinity of the gap. The results of the measurements made at peak spring tide conditions are shown in Figure 3.2. It can be seen in the photograph in Figure 3.3 that there is a considerable contraction of the flow through the gap and that there has been considerable scouring of the bed protection layer by the flows exiting from the dike. The contraction in the flow is generated as a boundary layer that originates from the upstream corners of the dike. Current speeds in the order of 8.5/s were measured at the separation point on the upstream corner of the gap and 7m/s in the middle of the gap.

Trials were then carried out in which closure of the gap in these conditions was attempted. The simulated end-dumping of the single model elements specifically manufactured from the end of the dike is shown on Plate 3.1. This test was totally unsuccessful, the modelled material being washed away from the gap immediately on entering the flow, the failure being most noticeable in the deepest waters. Plate 3.2 shows the results of these trials where a “stream” of this material can be seen downstream of the closure gap. A small amount of the material can be seen to be in place on the end of the dike above, or just below, the water surface.

A number of model gabions, weighing approximately 10 tonnes, were manufactured and similarly these also failed to maintain position in the gap

The client’s representatives visited HR Wallingford on completion of the above trials. During this visit the client’s proposed strategy and methodology for final closure of the dikes were clarified. In essence, it was proposed that final closure would be carried out at a rate of 20 m during each “slack” water period on suitable tides which occur between falling and rising mean tides (Note: - “slack” water taken to be when flows in the gap <1.0m/s). As well as end-dumping from the top of the dike, bottom- and side-dump barges (approximately 400 tonne loads) would be employed to deliver large quantities of a mixture of 80% 5 tonne maximum weight rocks and 20% 3 tonne gabions directly into the gap.

A series of indicative tests were quickly planned and carried out in the presence of the client’s representatives.

The main test would be to simulate the dumping of a large quantity of material into the gap at a time of “slack” water and gradually increasing the pump flow in the basin to give peak neap tide conditions as predicted by the numerical model. Initially the physical model had to be set-up to simulate the numerical model results for peak neap tide conditions in order to determine the target settings on the pump controls. The results of this model set-up are summarised in Table 3.1 and presented in Figure 3.3. Limestone chippings were selected to give the required size and mix for the material to be used for closure. To simulate the dumping of the closure materials as reasonably as possible, the scaled material was tipped into the model using a method representative of dumping from barges and simultaneously the same mix of materials was end-dumped from the top of the dike. However, complete closure of the gap was not attempted.

This test proved successful, as there was negligible movement of the dumped material, or the bed protection, as the water speed in the basin was increased up to peak neap tide conditions.

At the client’s representatives request further tests were carried out while they were in attendance. The discharge from the pumps was increased further in steps past the peak neap tide flow speed. At each discharge increment, as well as visual observations of the dike and bed protection, current speeds were measured in the centre of the closure gap and at one of the upstream corners of the gap. The results of these measurements are shown in Figure 3.4. The information presented on this figure shows that there is a good linear relationship between the two current speeds, the speed on the upstream corner of the gap being 13% higher than the gap speed. It should be noted that the flows in the centre of the gap were much less turbulent than those at the corner. This being the case peak current speed at the corner position could be expected to be at least 10% higher than the recorded mean. Further increase in current speed through the dike beyond a mid gap current speed of 6.5m/s initiated motion of some of the individual elements of the dike and the test was stopped. The downstream bed protection was observed to be under motion towards the end of this test and it was estimated that the threshold of motion of the proposed bed protection layer was achieved at a flow speed of 6 to 6.5 m/s.

At several stages of this phase of the test programme it was noted that a few of the dumped rocks either moved or, in a few cases, were displaced from the dike when flow speeds were increased. This is not considered significant as the percentage of “lost” rocks would be low (<5%) before the next period of dumping.

The width of the closure gap was then reduced by 40 m to see how the flow in the gap would be affected, especially when the convergence of the flow contraction occurred nearer to, and if possible on, the gap sill. The purpose of this test was to determine whether the flow turbulence within the convergence zone would have a greater influence than the smoother flow in that area when the dike gap was larger. The reduction in width was achieved by roughly constructing the dike using limestone chippings. These chippings represented rocks sizes between 6.5 and 10.5 tonnes with a mean mass of 8.75 tonnes and as such should be considered unrepresentative of prototype materials.

The flow in the basin was gradually increased. Flow through the newly constructed dike closure was observed and when the flow in the gap exceeded 6.5 m/s the downstream face of the newly constructed reduction collapsed, undoubtedly due to the pressure of flow through the dike. The observations made during this test are summarised in Table 3.2. This failure was of interest as individually the rocks were larger than will actually be used. However, the lack of smaller units mixed with the larger rocks meant that the void ratio was large. This allowed flow to pass through the dike and hence cause the failure. As a consequence of this failure it is clear that the void ratio of the constructed dike must be kept to the least possible to reduce minimise flow through the dike to the absolute minimum. This issue was not addressed as part of the described test programme.

3.4 Bed protection

The bed protection layer, downstream of the dike was observed to scour in many of the trials carried out, the estimated threshold speed at onset of motion to be between 6 and 6.5 m/s. However, the current speed was estimated from current measurements in the horizontal plane and it is likely that close to the toe of the dike there could well be a considerable component of speed acting vertically downwards. This downward flow could have the effect of undermining the bed protection, causing the material to be become mobile at a lower horizontal speed than would be expected.

3.5 Conclusions

The following conclusions can be drawn from the schematised test programme:

1. Closure of a 100 m gap in the spring tide conditions tested using end-dumped material having a weight range 3 to 7 tonnes is not feasible. Considerable erosion of the bed protection also occurs under these conditions.
2. Using a mixture of 80% 5 tonne rocks and 20% 3 tonne gabions as closure material and placing during “slack” water conditions, large quantities of have been shown to withstand gap speeds in the order of 8 m/s. This material being placed by both bottom or side dump barges close to the existing dike and also from the crest of the dike.
3. Bed protection can only withstand speeds of 6 to 6.5 m/s, typical of conditions just in excess of neap tides.

4 It was noted that a few of the side or end-dumped rocks placed during periods of “slack” water either moved or, in a few cases, were displaced from the dike when flow speeds were increased. This is not considered significant as the percentage of “lost” rocks would be low (<5%) before the next period of dumping.

5 The void ratio of the constructed dike must be kept to the least possible to reduce flow through the dike to the absolute minimum. Although this issue was not addressed as part of the principal test programme the failure test carried out at the completion of the test programme indicated that through-dike flow could seriously impact on the integrity of the dike if not adequately restricted.

3.6 References

1 River and Channel Revetments; A Design Manual. Escarameia, M. (1998). Thomas Telford Ltd., London, 1998.

Table 3.1 Summary of test conditions

		Peak spring tide conditions		**Peak neap tide conditions**	
		Numerical model (Target)	**Physical model**	**Numerical model (Target)**	**Physical model**
100m Upstream	Level (m MSL)	- 0.20	+2.25	-0.05	0.00
	Speed (m/s)	2.32	1.75	2.05	1.06
Centre of Gap	Level (m MSL)	-2.23	-0.50	-1.66	-1.50
	Speed (m/s)	7.45	7.45	6.09	6.22
100m downstream	Level (m MSL)	-1.97	-0.50	-1.48	-1.50
	Speed (m/s)	5.46	8.02	4.48	6.22

Table 3.2 Reduced width gap, summary of observations

Pump speed setting (Nominal)	**Current speed in centre of gap (m/s)**	**Observations**
1.0	3.8	No movement in any element of dike
1.3	4.8	No movement in any elements of dike
1.6	5.4	Rocks on dike sill rocking. Flow through the dike. Perceptible head loss through dike.
2.0	6.3	Increased rocking on dike sill. Some movement of rocks on sill. Increased low through the dike with noticeable head loss. No material loss from downstream toe of dike. Movement in the bed protection layer.
2.4	No measurements made	Downstream face of dike failed in rocks added to reduce gap length.

NOTE This test carried out with closure gap width reduced by approximately 40% using non-representative rocks

4. INTERPRETATION OF COMPUTATIONAL AND PHYSICAL MODELLING

4.1 Overall closure strategy 2003 to 2006

KARICO Scenarios 1 and 2

- *Gap 3 is closed in March 2003*

- *In March 2006, Gaps 1 and 2 are closed either simultaneously (Scenario1) or Gap 1 is closed 14 days before Gap2 (Scenario2)*

The effect of closing Gap 3 is to increase peak depth-averaged velocities over the sill at Gap 2 by about 25%.

- Over the top of the sill (at –16m MSL), the depth-averaged velocity increases from a maximum of about 4 m/s to about 5 m/s. Here, using information in Escarameia & May (1992) and Pilarcyzk (1990), we have concluded that the 3 tonne gabions and 4 to 5 tonne rock should probably be stable as bottom protection, assuming that the depth of water and the width of the gap is such that excessive local turbulence will be avoided;

- Over the deeper sea bed areas (level approx. –25m MSL), the velocities increase from about 2.2 m/s to a maximum of about 3.3 m/s. The rock sizes here are smaller, ranging from 0.5 –1 tonne, with some gabions of 3t, but should be able to cope with the less severe velocities here without difficulty.

The effect on velocities through Gap 1 is smaller (increase of about 15% from 4 to 4.6 m/s) and does not give rise to significant cause for concern.

KARICO Scenario 3

- *Gap 1 and Gap 3 are closed in March 2003*

- *Gap 2 is closed in March 2006*

The effect of closing Gap 3 is to increase peak depth-averaged velocities over the sill at Gap 2 by about 65%.

- Over the top of the sill (at –16m MSL), the depth-averaged velocity increases from a maximum of 4 m/s to about 6.8 m/s. Here, the information in Escarameia & May (1992) and Pilarcyzk (1990), suggests that the 3 tonne gabions and 4 to 5 tonne rock may well be starting to move. Whilst this might be acceptable for a short period of time during final closure in 2006, we consider it would be undesirable for the extended period from 2003 to 2006 as there would be a significant risk of significant amounts of material being moved during that time. In this regard it is important to note that when the effect of wave action is added, the shear stress on the sill stones is increased and loss of stability is more likely. Gap No. 3 is particularly vulnerable here because it has the highest cill level (-6.8 m MSL).

- Over the deeper sea bed areas (level approx. –25m MSL), the velocities increase from about 2 m/s to a maximum of about 3 m/s. The rock sizes here are smaller, ranging from 0.5 –1 tonne, with some gabions of 3t, but should be able to cope with the less severe velocities here without difficulty.

4.2 Final closure of Gaps 1 and 2

A comparison of the numerical modelling results in Section 2.3 of this report suggests that Gap No. 2 is generally the most severely affected by tidal velocities and so our report has concentrated on addressing this gap.

There are two main issues to consider – stability of bed protection and stability of the material being used to form the temporary ends of the dikes.

Bed protection

Our physical modelling results show that this would generally be stable up to bed velocities of 6 to 6.5 m/s, i.e., to velocities in excess of those that would be experienced during neap tide conditions on the 3rd stage closing.

Under spring tide conditions, especially during the final waiting period after the second stage closing, bed velocities exceed those under the neap tide conditions on the 3rd stage closing. In fact, velocities during the final waiting period can be up to 20% higher than neap tide velocities for the KARICO scenario and even higher for the KARDI scenario. This suggests that bed velocities may exceed 7m/s in places, in which case the bed protection would start to erode in these locations. Consideration should be given to increasing the bed protection, possibly doubling the stone weight. However, it must be appreciated that the additional stability offered by gabions in the bed protection was not modelled by HR Wallingford and hence there may in fact be adequate reserves of strength to cope with the peak velocities at mid-tide conditions.

It is understood that the bed protection has been designed as a "falling apron," with a length calculated as 6 times the depth of the soft material down to the underlying rock. Since the bed material is so fine, this is very prudent as there is no doubt that the bed material will erode on both sea and reservoir sides of the gap and could easily erode in places right down to the underlying rock.

As the bed scours and the apron falls, the velocities over the bed protection will fall and this may well provide adequate compensation for the concerns about limits on stability being exceeded under the highest velocities during spring tide waiting periods.

Rocks (and gabions) at end of dikes

The 80% 5-8 tonne rock and 20% 3 tonne gabion combination was found to be stable at the end of the dikes for velocities up to about 8 m/s.

Some attempt has been made to use this information to interpret the likely stable stone weights required under other conditions by assuming that the stone weight varies according to the 6th power of velocity.

The results are shown in Table 4.1 and indicate that the rock sizes suggested by KARICO are generally satisfactory under neap tide conditions, but will not be stable under spring tide conditions at the south side of Gap No. 2 and the north side of Gap no. 1.

This result must be interpreted with some caution for two reasons:

i. The critical velocity for 5-8 tonne rock might be as high as 8.5 m/s.

ii. KARICO intend to provide gabions for the temporary ends of the dikes during the spring tide waiting periods and experience has shown that these are generally more stable.

However the increase in velocity determined at these locations strongly suggests that it is necessary to revise the design.

Table 4.1 Interpretative table of stable stone weights at end of dikes for Gap No. 2

Project Stage	Width of gap No. 2	Tidal condition	Mid gap velocity from numerical model		Equivalent gap edge velocity [1]	Stone weight	
			Primary runs (no slip boundary)	Runs with slip boundary		Predicted stable value [2] (tonnes)	Average value provided (tonnes)
Completion of vertical closure	850	Spring	6.21	-	6.7 (7.5)	2 (4)	1.0
After 1st stage closing	700	Spring	7.05	-	7.6 (8.5)	5 (9)	2.25
After 2nd stage closing	500	Spring	7.83	7.5	8.4 (9.4)	9 (17)	4.0
After 2nd stage closing (KARDI alternative)	310	Spring	7.98	-	8.6 (9.6)	10 (19)	4.0
During 3rd stage closing	100	Neap	6.09	5.8	6.6 (7.3)	2 (4) [3]	6.5
During 3rd stage closing	50	Neap	6.04	-	6.5 (7.2)	2 (4) [3]	6.5

---

[1] The first gap edge velocity is based on a symmetrical flow pattern and uses the 13% increase in velocity from the gap centre velocity derived from the physical modelling. (The gap centre velocity is calculated as 5% smaller than the peak mid-gap velocity, based on a comparison of the runs with and without a "slip" boundary). The second velocity (in brackets) takes account of the flow assymetry identified in the final SUPG numerical modelling described in Section 2.3 (see Figures 2.27 to 2.30) which suggests that velocities at the south edge of Gap No. 2 and the north edge of Gap No. 1 could be up to twice this value (i.e. about 25%) higher.

[2] The stable stone weights correspond to the velocities in the previous column. Because of the flow assymetry, there is evidence that the velocities at the north edge of Gap No. 2 and the south edge of Gap No. 1 will be of the same order as the gap centre velocities. In this case, the stone weights already provided KARICO appear to roughly correspond to the stable stone weights for all spring tide conditions and no change will be necessary.

[3] Under no circumstances should the stone weights required for neap tide conditions be reduced from those already provided for by KARICO. The weights give a reserve of stability and will provide some capacity in the event that the gap has to experience intermediate tides between neaps and springs.

5. CONCLUSIONS

1. The TELEMAC model has been set up for the Saemangeum project and calibrated against observations made during a spring tide in April 2001. Initial tests for the overall closure strategy were run with a representative large spring tide, being that of 9/10 April 2001, but representative of the 20 largest range tides in any year. Subsequent tests to predict velocities during the final closure of Gaps 1 and 2 have been run for the relevant spring or neap tides of March / April 2006. The work on predicting final closure conditions has been complemented by physical modelling of a schematised version of Gap No. 2 when the Gap width was 100m. This permitted assessments of stone stability.

<u>Overall closure strategy 2003 to 2006</u>

2. It is understood that KARICO are considering (Scenarios 1 and 2) closing Gap 3 in 2003 rather than 2006. HR Wallingford's modelling for the interim report suggested that the resulting increase in velocities in Gap 2 would be about 25% with a resulting maximum depth averaged velocity of about 5.0 m/s. Assessments of the bed protection provided by KARICO in Gaps 1 and 2 suggest that it would be able to withstand the increased velocities over the period 2003 to 2006.
(HR Wallingford was not in a position to make a recommendation as to whether Scenario 1 or Scenario 2 is to be preferred and this is probably more a matter of construction programming than anything else).

3. As an alternative KARICO have contemplated (Scenario 3) a situation in which both Gaps 1 and 3 would be closed in 2003 leaving only Gap 2 open during the period 2003 to 2006. HR Wallingford's modelling has suggested that the resulting increase in velocities in Gap 2 would be about of the order of 65%, with a resulting maximum depth averaged velocity of about 6.8 m/s. HR Wallingford advises KARICO not to adopt this scenario as the bed/sill protection in Gap 2 would be vulnerable to significant movements during the period 2003 to 2006.

4. The effect of Garyeok and Sinsi sluices being open or closed during 2003 to 2006 is small. This appears to be because the combined width of the dike gaps is much larger than the combined width of the open sluices. The open sluices will be much more important in reducing velocities through the gaps during the final closure procedures.

5. There are two main groups of practical and engineering reasons that also suggest it would be appropriate to close Gap 3 in 2003 rather than in March 2006

   (A) The vulnerability of Gap 3

   (i) Gap No 3 has a high sill (-6.8m MSL) and hence is particularly vulnerable to the additional instability introduced by wave action. The gabion wire in the sill protection material is corroding and it is risky to allow a further 3 years with that corrosion and the related risk of gabions disintegrating.
   (ii) If Gap No. 3 remains for 3 more years, there is a risk that a significant tidal channel may develop in the deep soft bed on the reservoir side of the dike. This would compromise future land and water area use, in comparison to Gaps Nos 1 and 2 where existing deep tidal channels were in existence prior to the commencement of the Saemangeum project.
   (iii) It is risky to close Gap No. 3 during the winter period (which includes March 2006). This is because (see HR Report EX 3668), Dike No. 4 in which Gap No. 3 is located is subject to direct attack from North Westerly waves during this period. Stable stone weights would need to be much higher to resist this additional action.

(B) Other opportunities and advantages related to the early closure of Gap 3

- (i) As the construction programme permits Gap No. 3 to be closed in 2003, it makes sense in a general way to proceed with the closure as soon as possible. Reducing the amount of material to be placed during 2006, reduces the risks in case of unpredictable problems during final closure - it is easier to be closing 2 gaps rather than 3 as less quantity of material is needed.
- (ii) Most of the construction work for the Sinsi sluices will be made during 2004 to 2005. If Gap 3 is closed in advance, this opens up a direct land access route to this site from the north to allow construction materials to be brought to the Sinsi site from the north.

6. It is suggested that final closure of Gap No. 3 is not carried out in *March* 2003, but deferred until a time in 2003 when the wave climate is more benign for Dike No.3

Final closure of Gaps Nos. 1 and 2

7. Computational modelling of the final closure of Gaps Nos. 1 and 2, suggests that mid gap speeds of flow through the gaps will reach 6 m/s on neap tides and nearly 8 m/s during spring tide waiting periods.

8. Adoption of the alternative closure scenarios by KARDI will slightly increase velocities in Gap No.2.

9. Bed protection material appears to be generally stable until towards the end of the final closure. Under final closure, neap tide conditions, the "vena contracta" convergence of flow and the generally increased turbulence means that it is at its limit of stability. During the final spring tide waiting periods, velocities occasionally exceed the limit of stability. For this reason, KARICO may wish to consider increasing stone weight (see Section 4.2) or reassessing the additional stability offered by the gabions in the bed protection.

10. KARICO's falling apron concept for the bed protection, allowing it fall as the seabed scours at the edge of the protection, seems entirely reasonable. As it lowers, it may also helpfully reduce velocities over the bed protection.

11. The stone weights suggested by KARICO for the ends of the dykes during closure are generally satisfactory during neap tide conditions, assuming they are placed in still water conditions.

12. During the spring tide waiting periods, the stone weights suggested by KARICO for the ends of the dikes at the north end of Gap no.2 and the south end of Gap No.1 are believed to be satisfactory.

13. During spring tide waiting periods, the stone suggested by KARICO for the South side of Gap No.2 and the north side of Gap No.1 appears to be unstable. Here it would be preferable to use only single gabions or gabions linked together in a robust way together to form weights approaching those estimated by HR Wallingford's calculations:

    - 2 to 4t after completion of vertical closure
    - 5 to 10t after 1st stage closing
    - 10 to 20t after 2nd stage closing

    It is considered that further investigations of stable gabion weights by RRI/KARICO are essential in order to derive the final design for these locations.

14. Velocities along the faces of the dikes adjacent to the sea and reservoir could not be found to cause a problem for stone stability from interpretation of either the numerical or physical model. However, unforeseen turbulence effects cannot be ruled out.

6. REFERENCES

Escarameia, M. and May, R. W. P. (1992). Channel protection downstream of structures. Report No SR313, April 1992, HR Wallingford.

Pilarcyzk, K. W. (1990). Stability criteria for revetments. Proc of the 1990 National Conf. on Hydraulic Engineering, ASCE. Eds H. H. Chang and J. C. Hill. San Diego, USA.

Figures

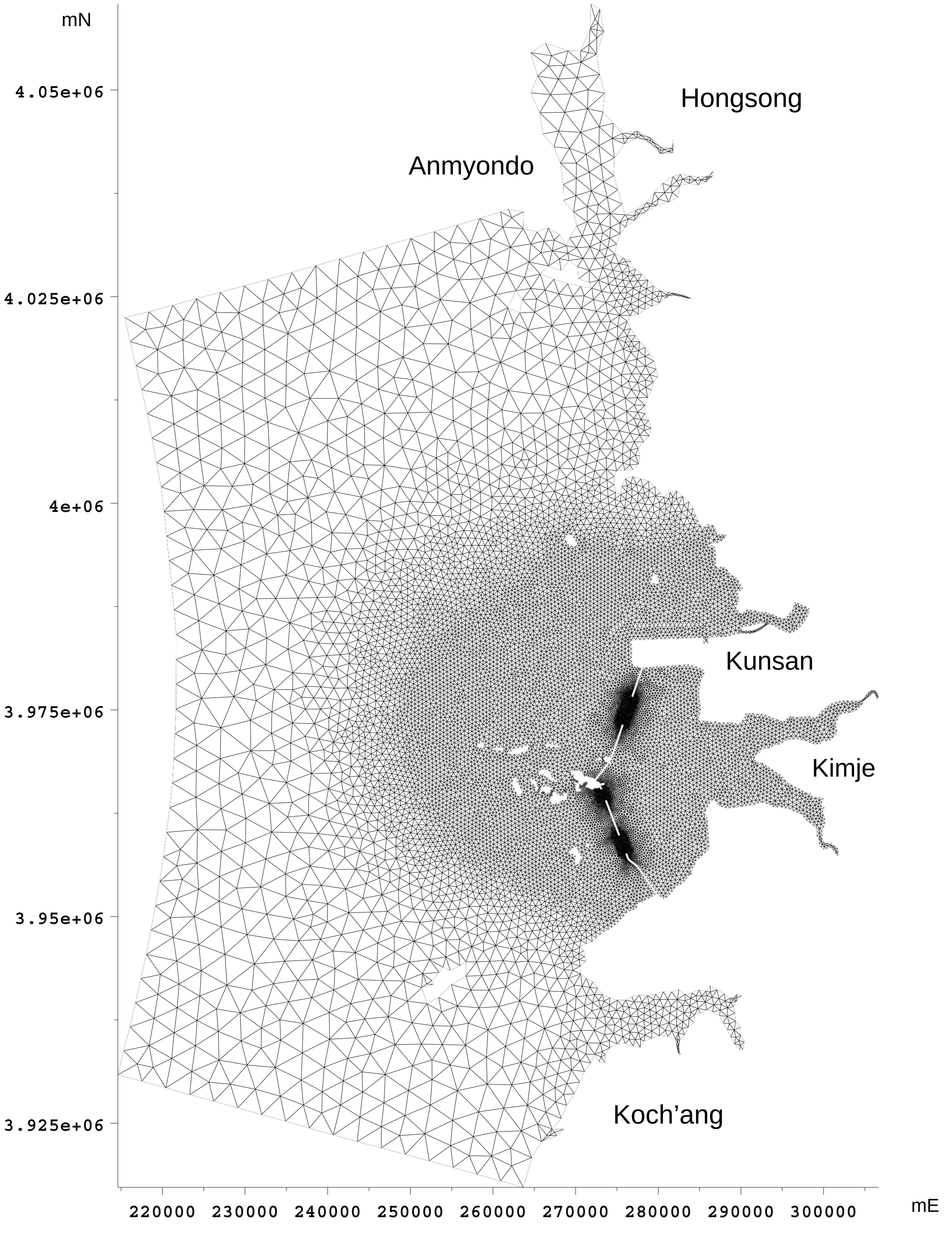

Figure 2.1 Numerical model mesh

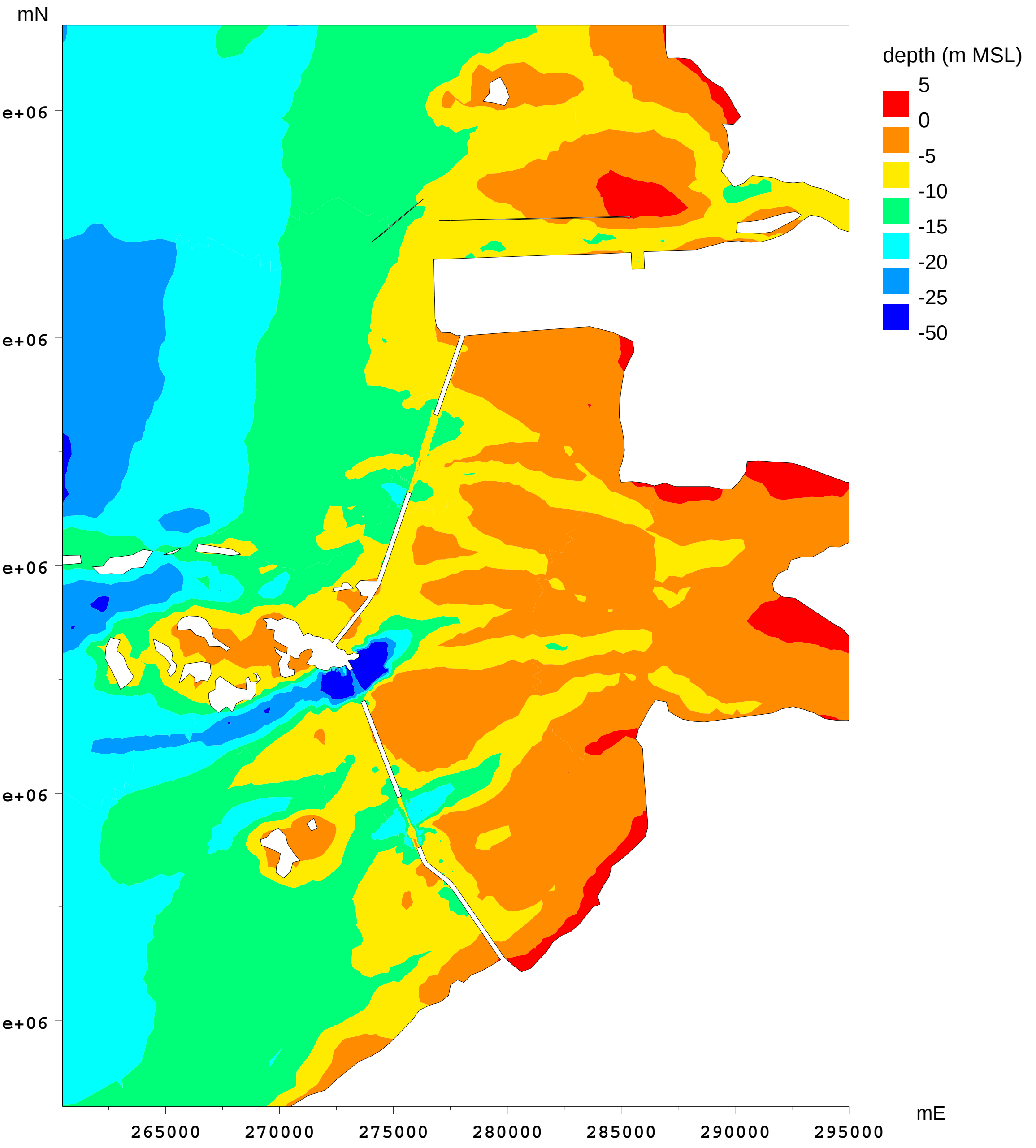

Figure 2.2 Model bathymetry in the area of interest

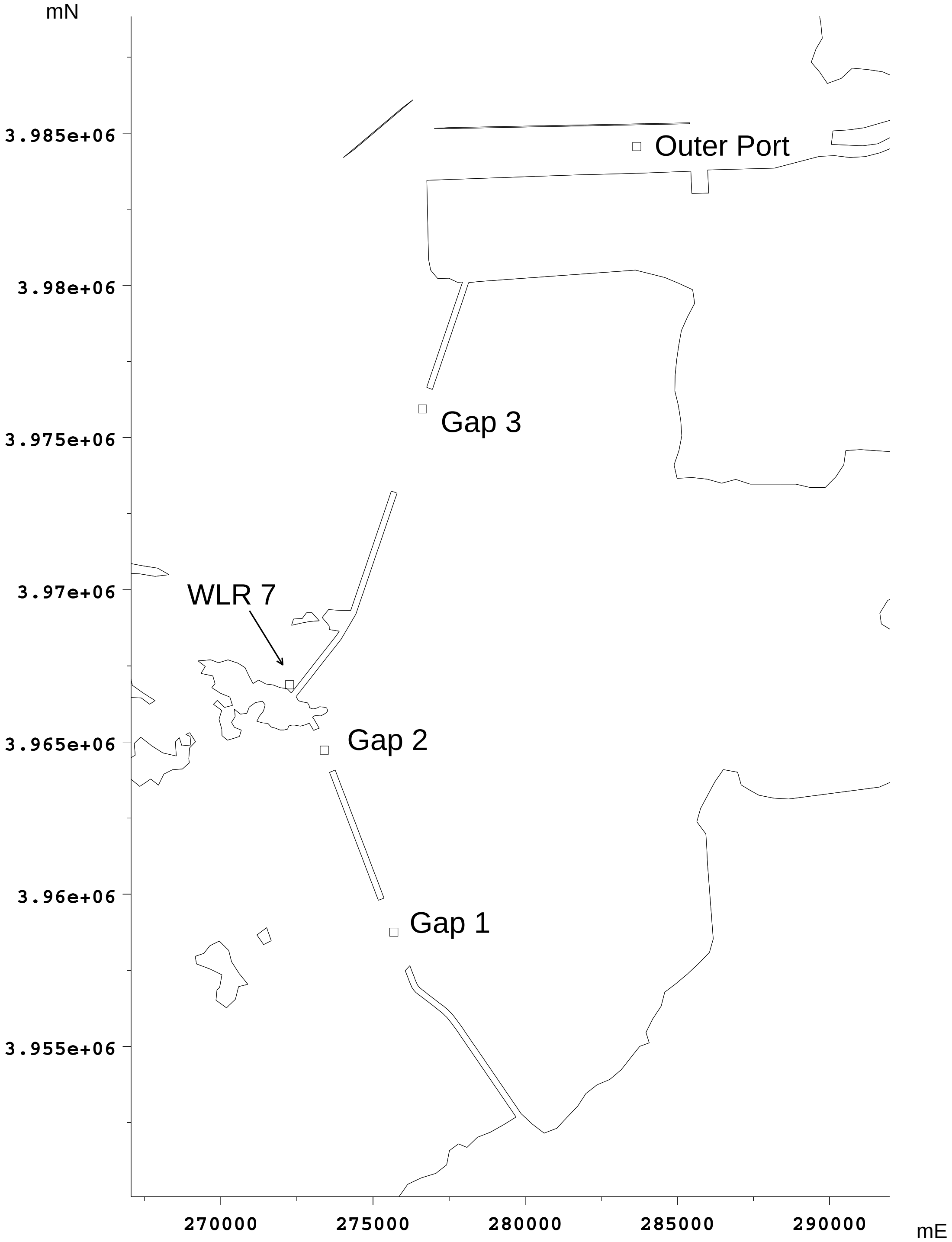

Figure 2.3 **Detail of model showing positions for field measurements**

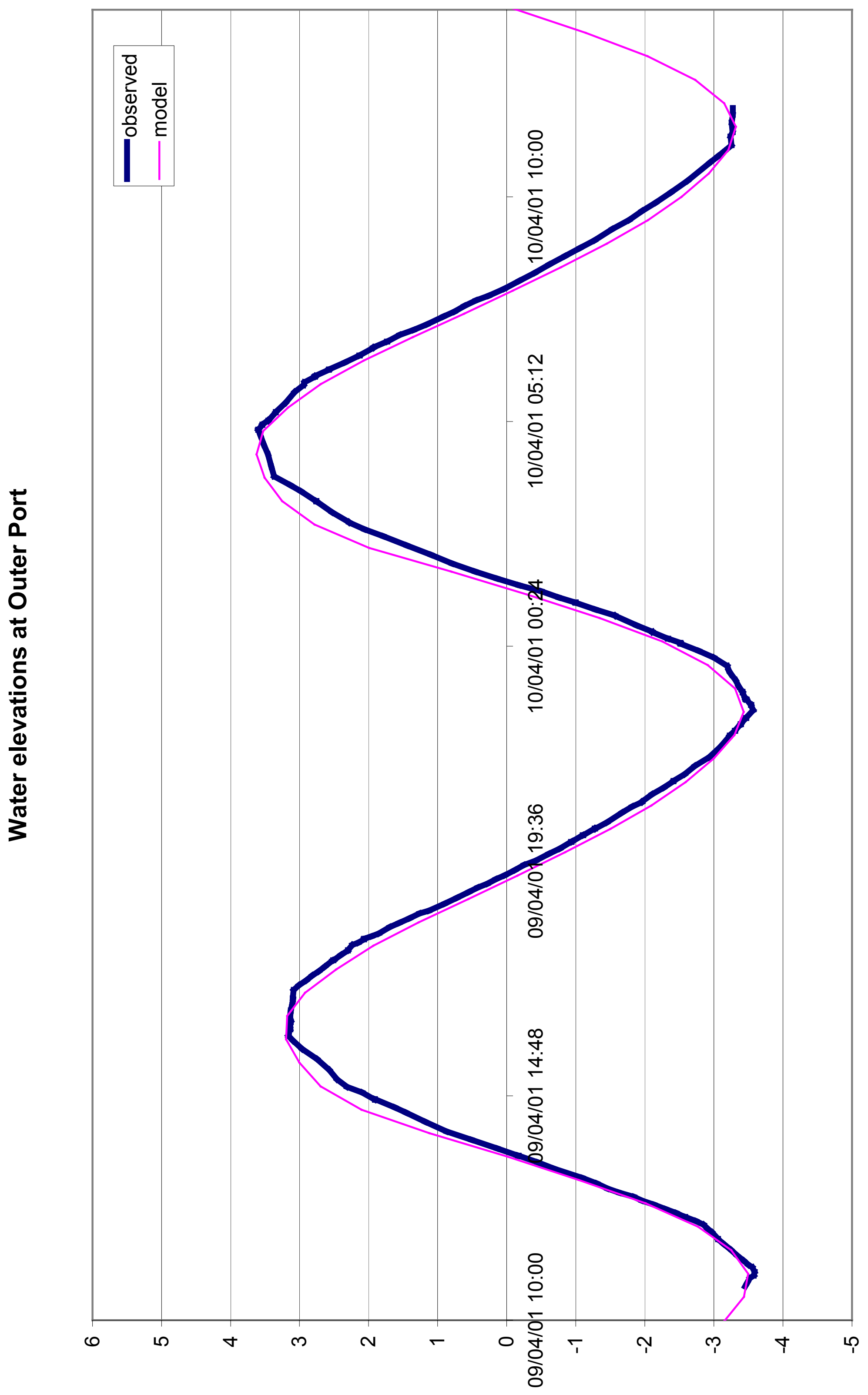

Figure 2.4 Calibration plot of tidal elevations at Kunsan Outer Port

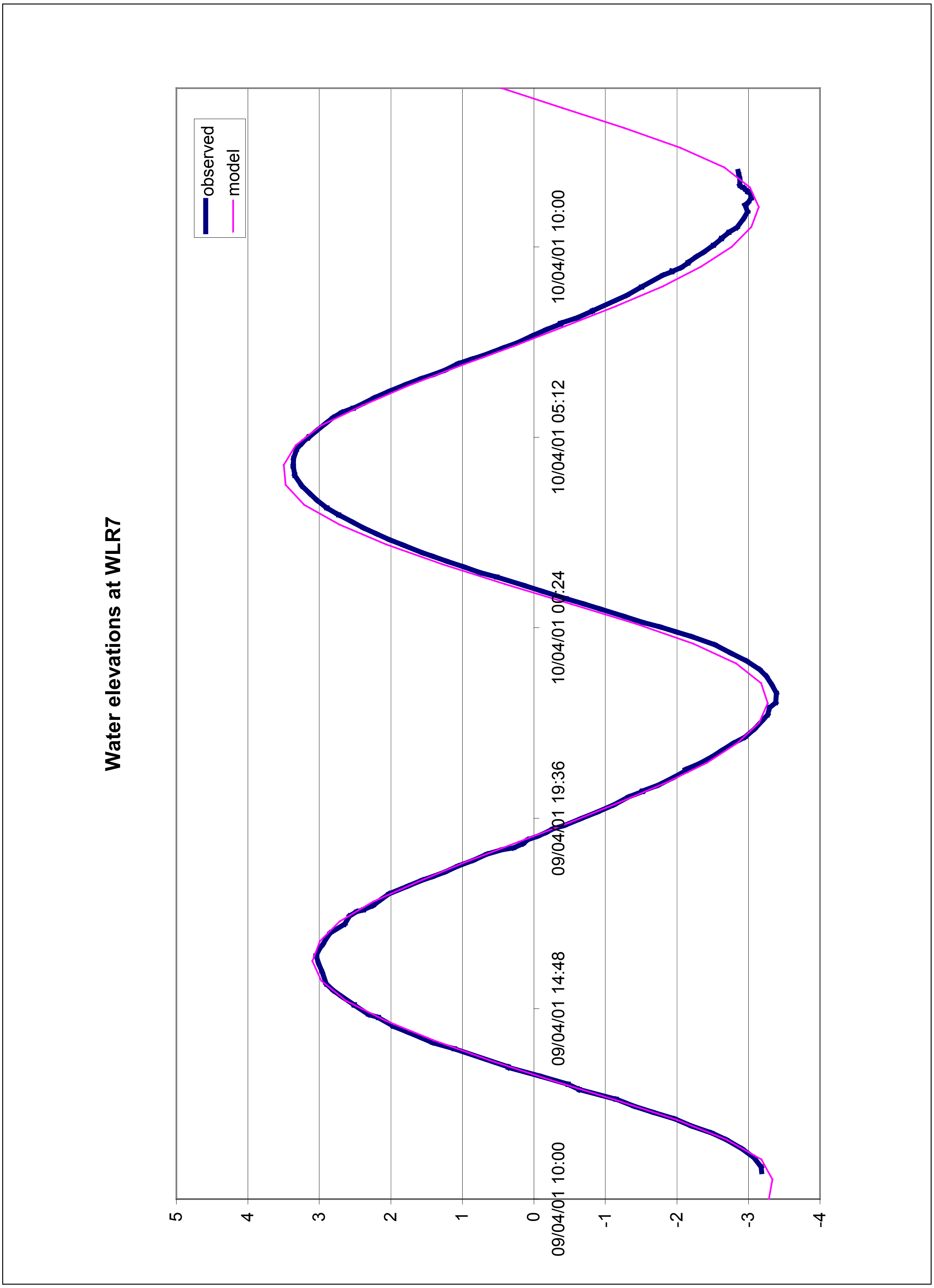

Figure 2.5 Calibration plot of tidal elevations at WLR7

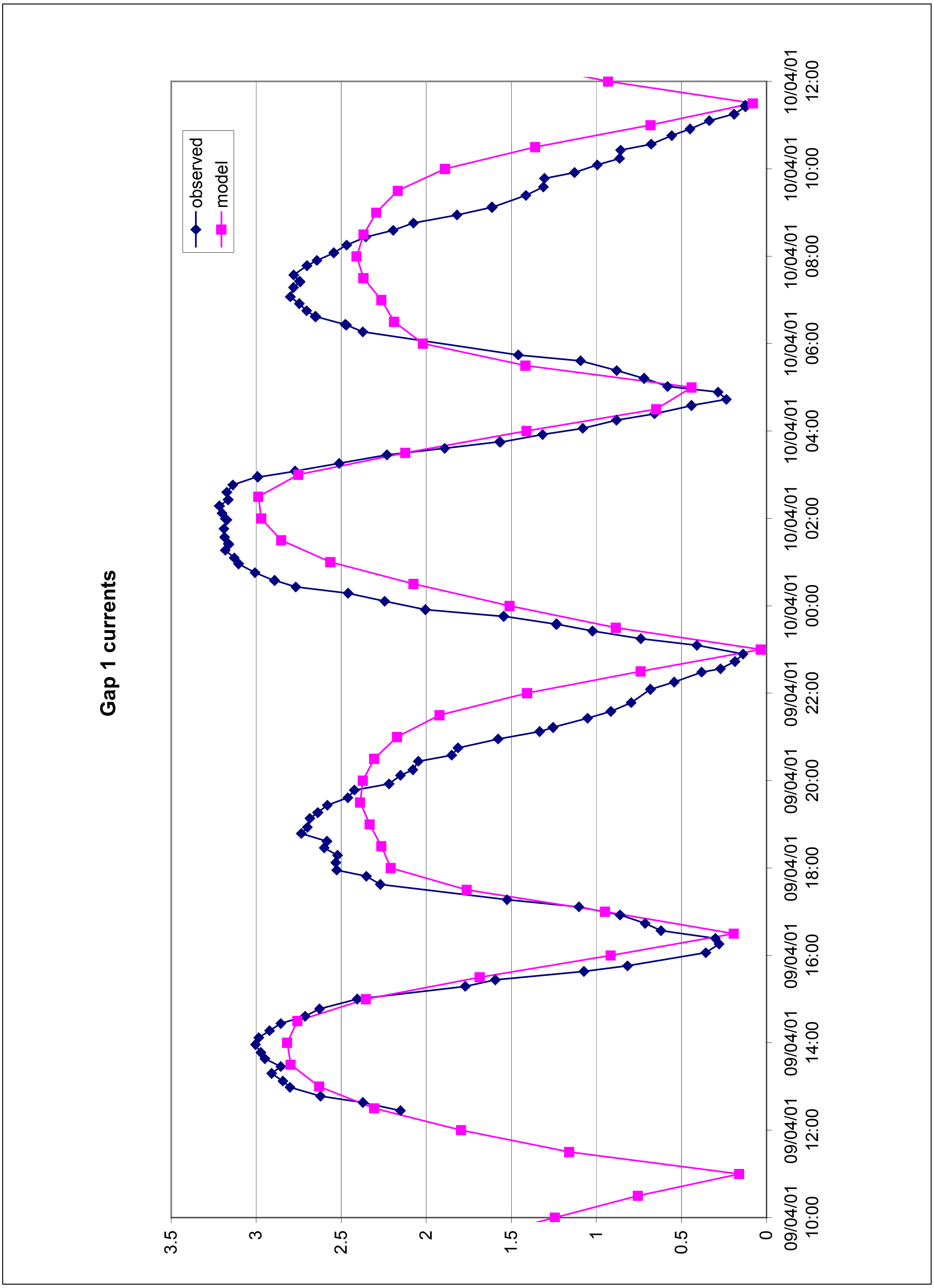

Figure 2.6 Calibration plot of current speed in gap 1

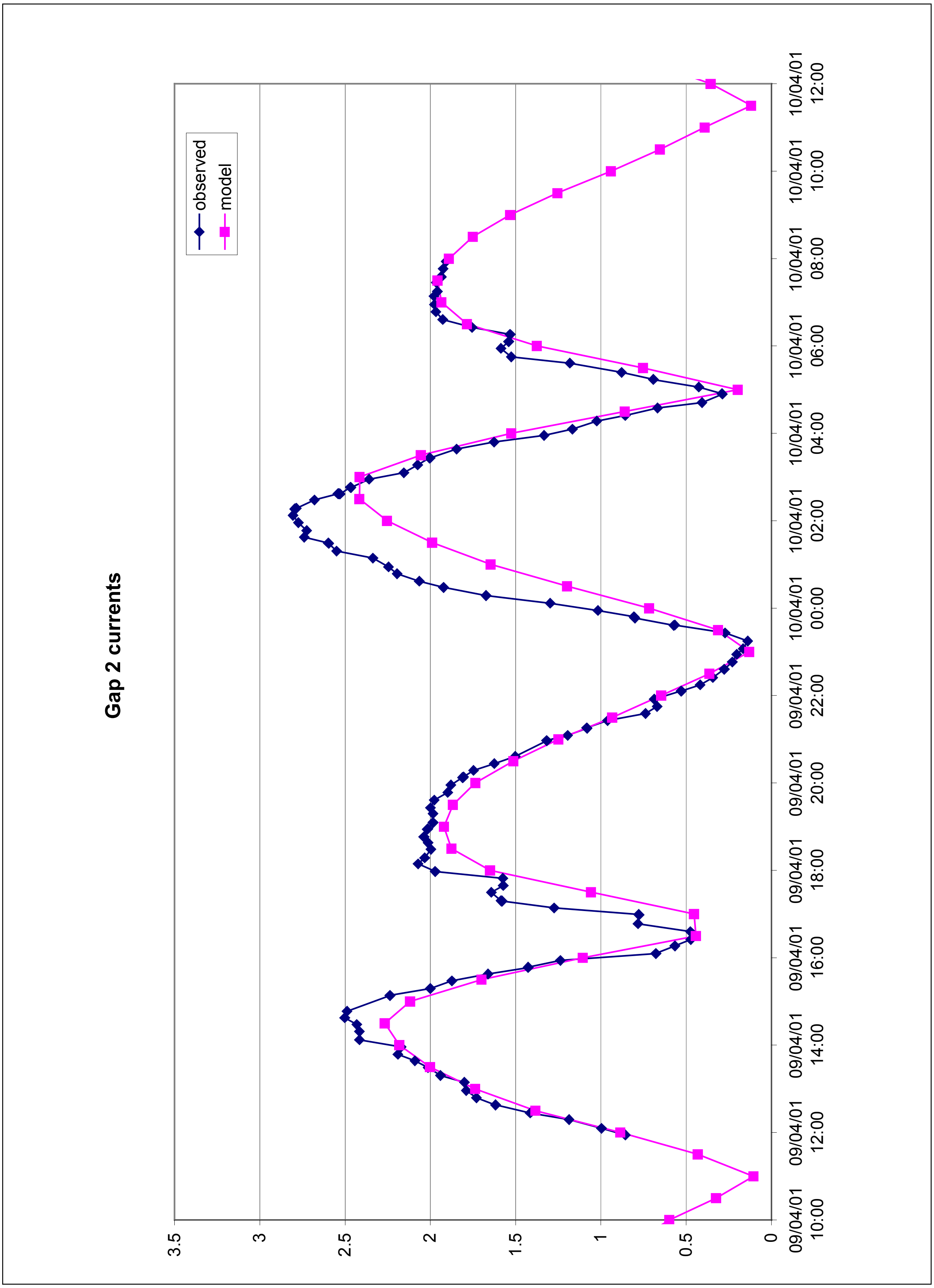

Figure 2.7 Calibration plot of current speed in gap 2

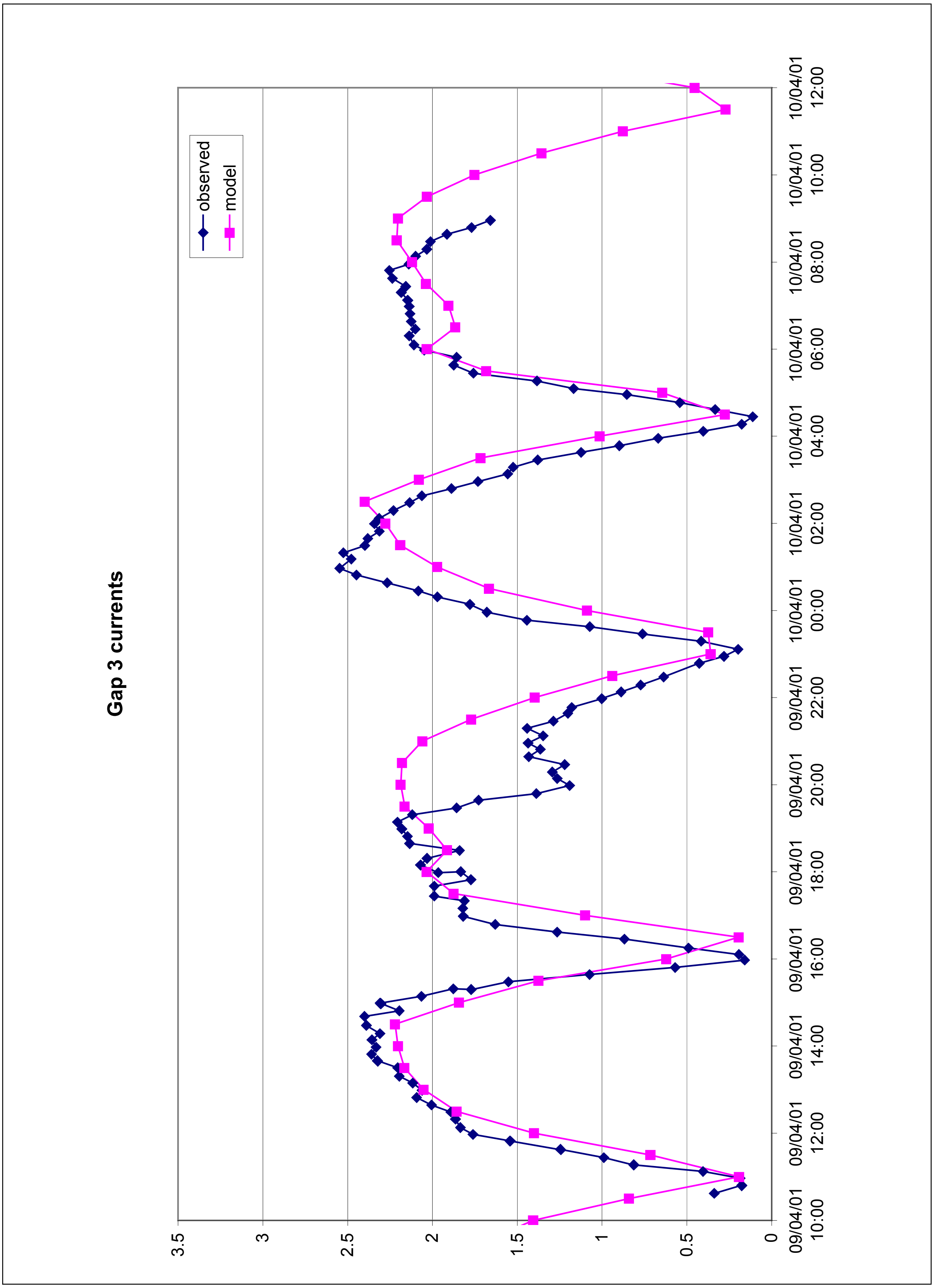

Figure 2.8 Calibration plot of current speed in gap 3

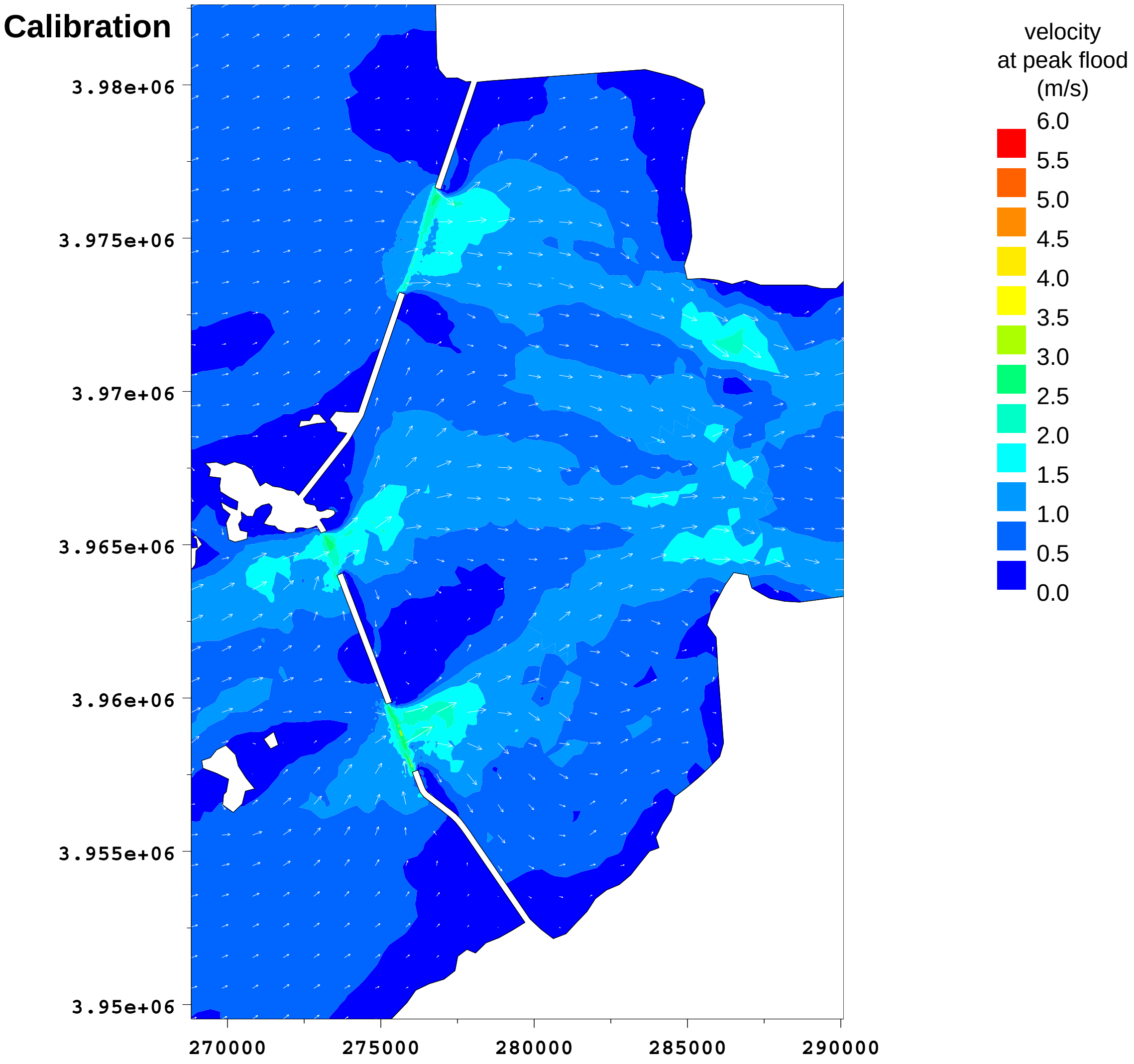

Figure 2.9 **Calibration plot of current velocity vectors at peak flood**

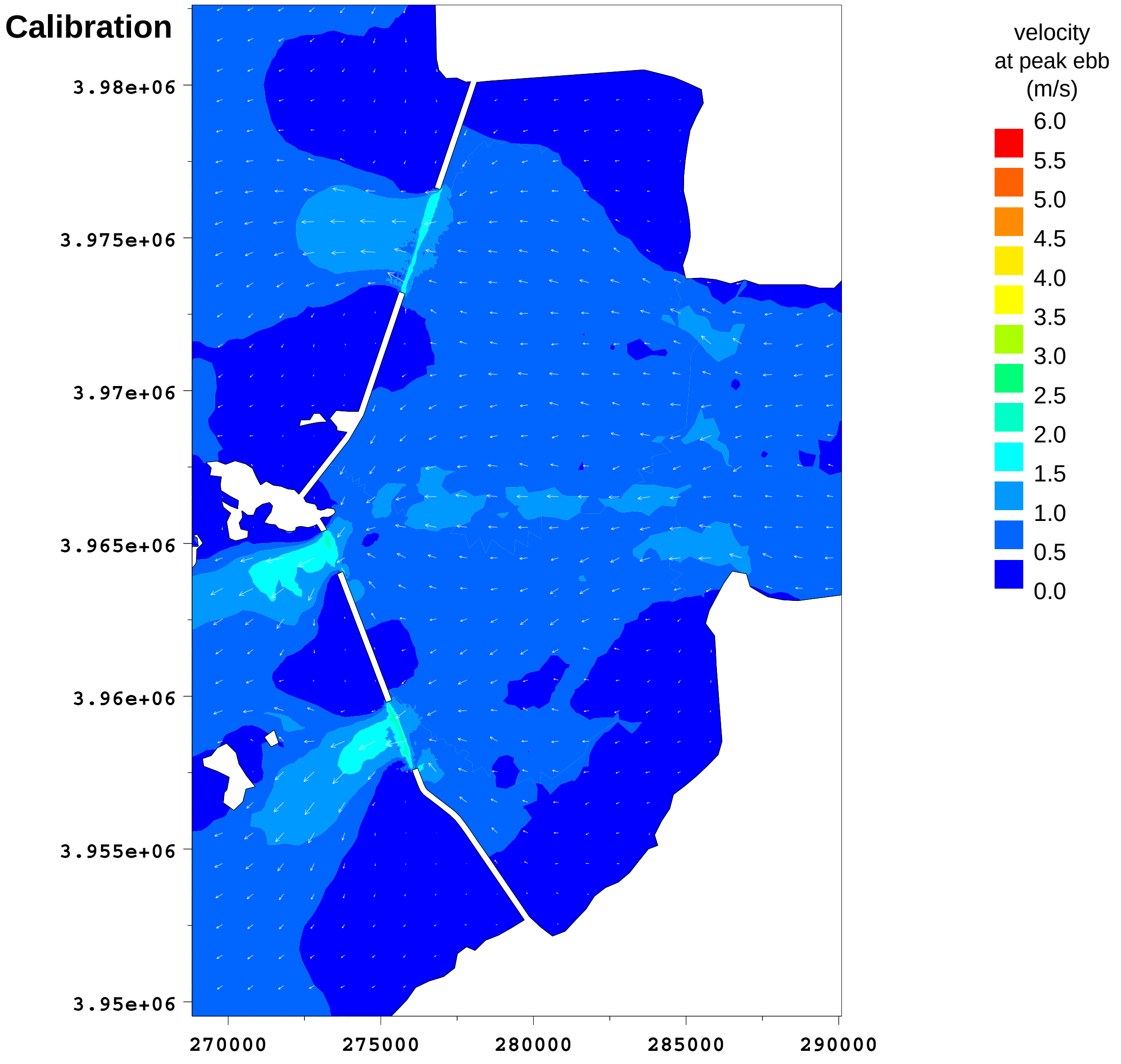

Figure 2.10 Calibration plot of current velocity vectors at peak ebb

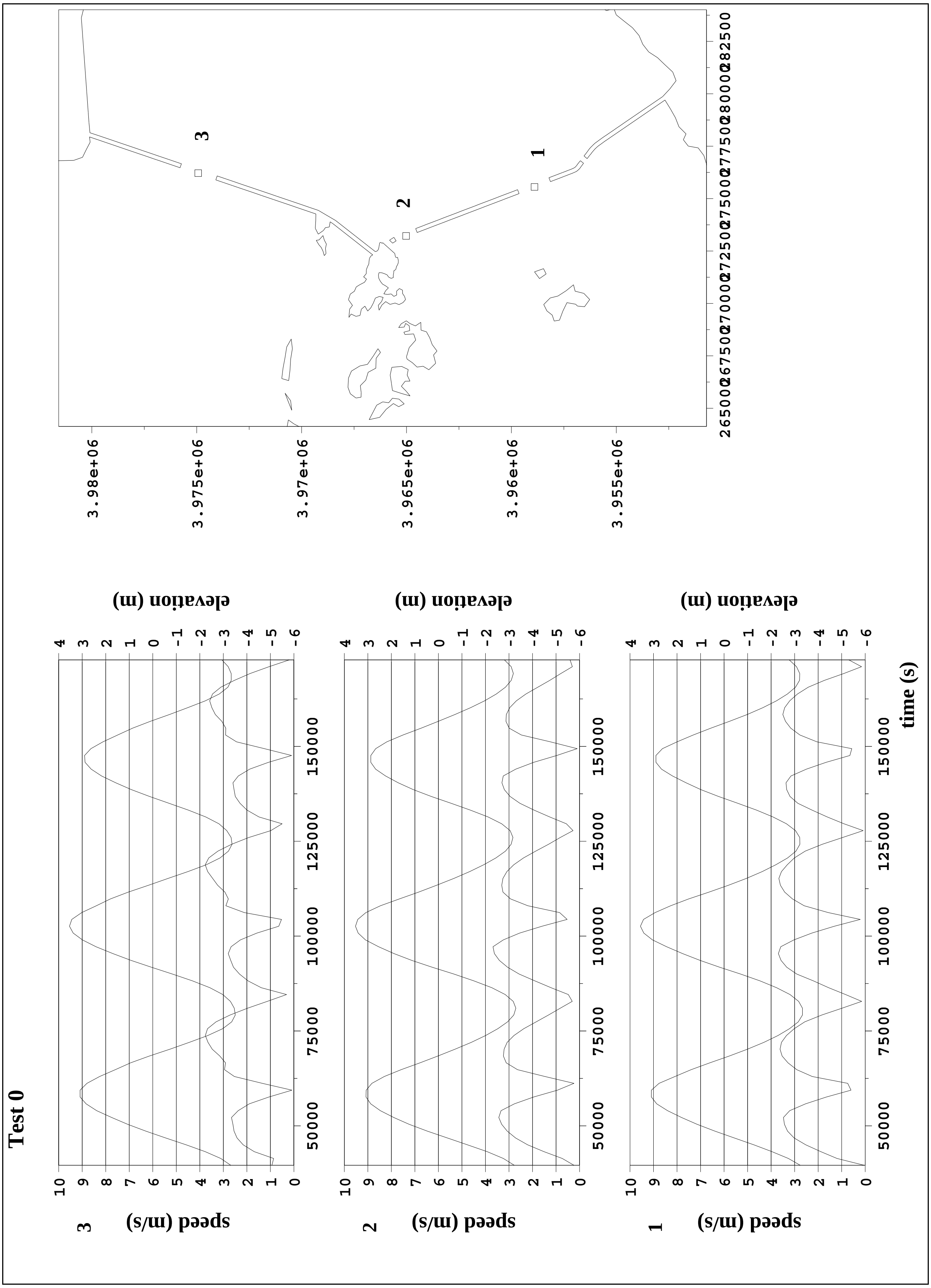

Figure 2.11 Water elevation and current speed for Test 0

Test 1

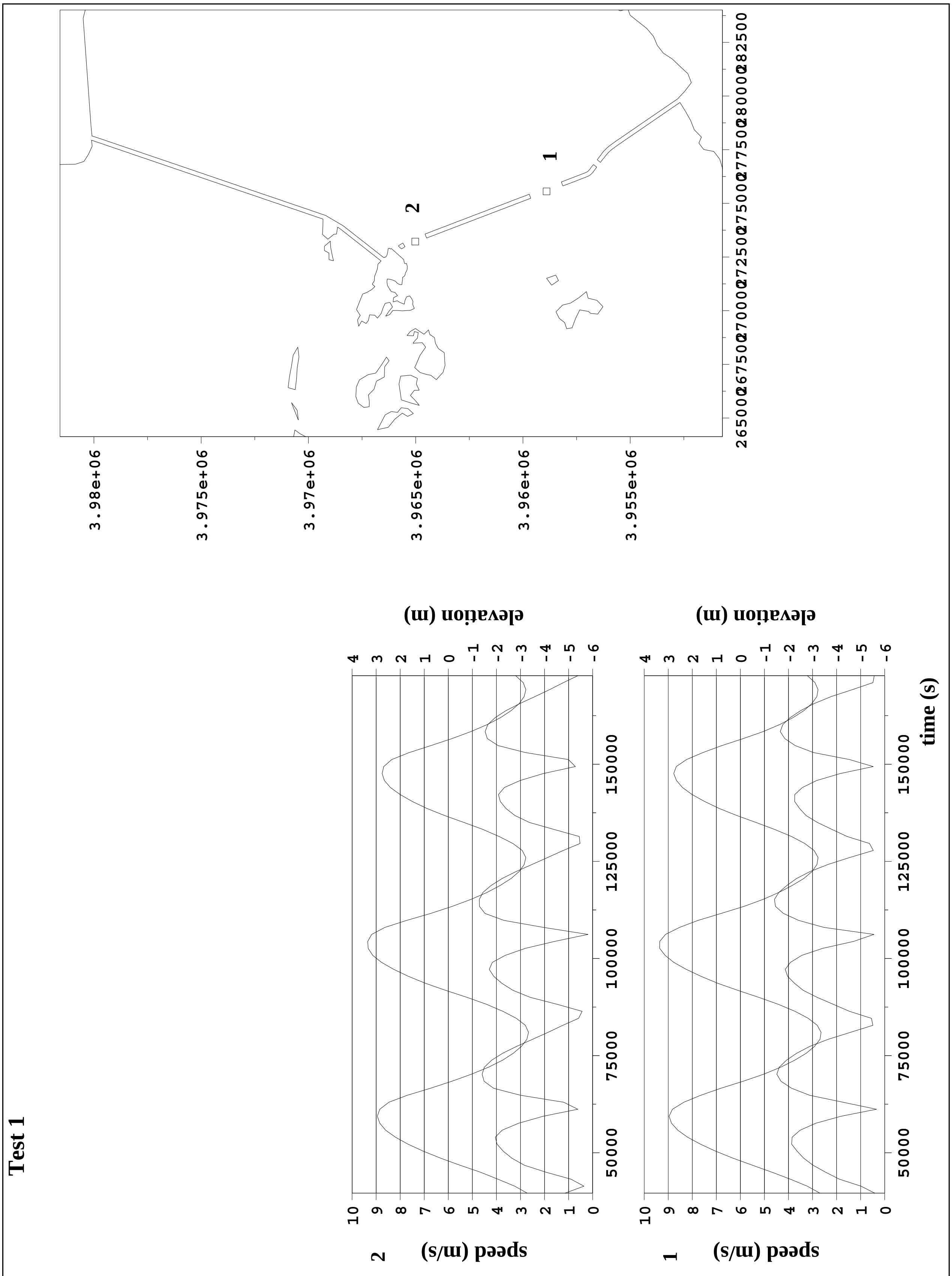

Figure 2.12 Water elevation and current speed for Test 1

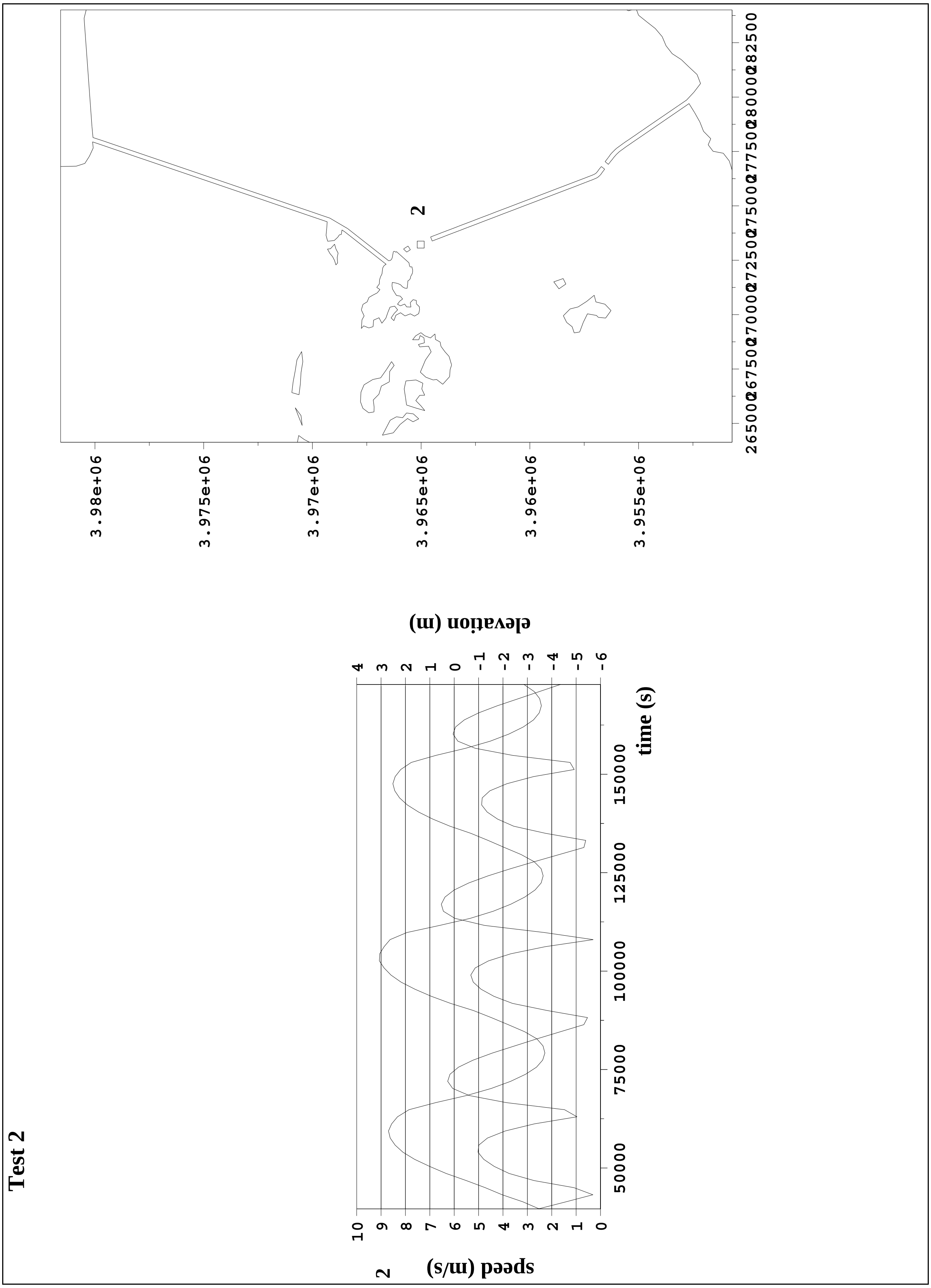

Figure 2.13   Water elevation and current speed for Test 2

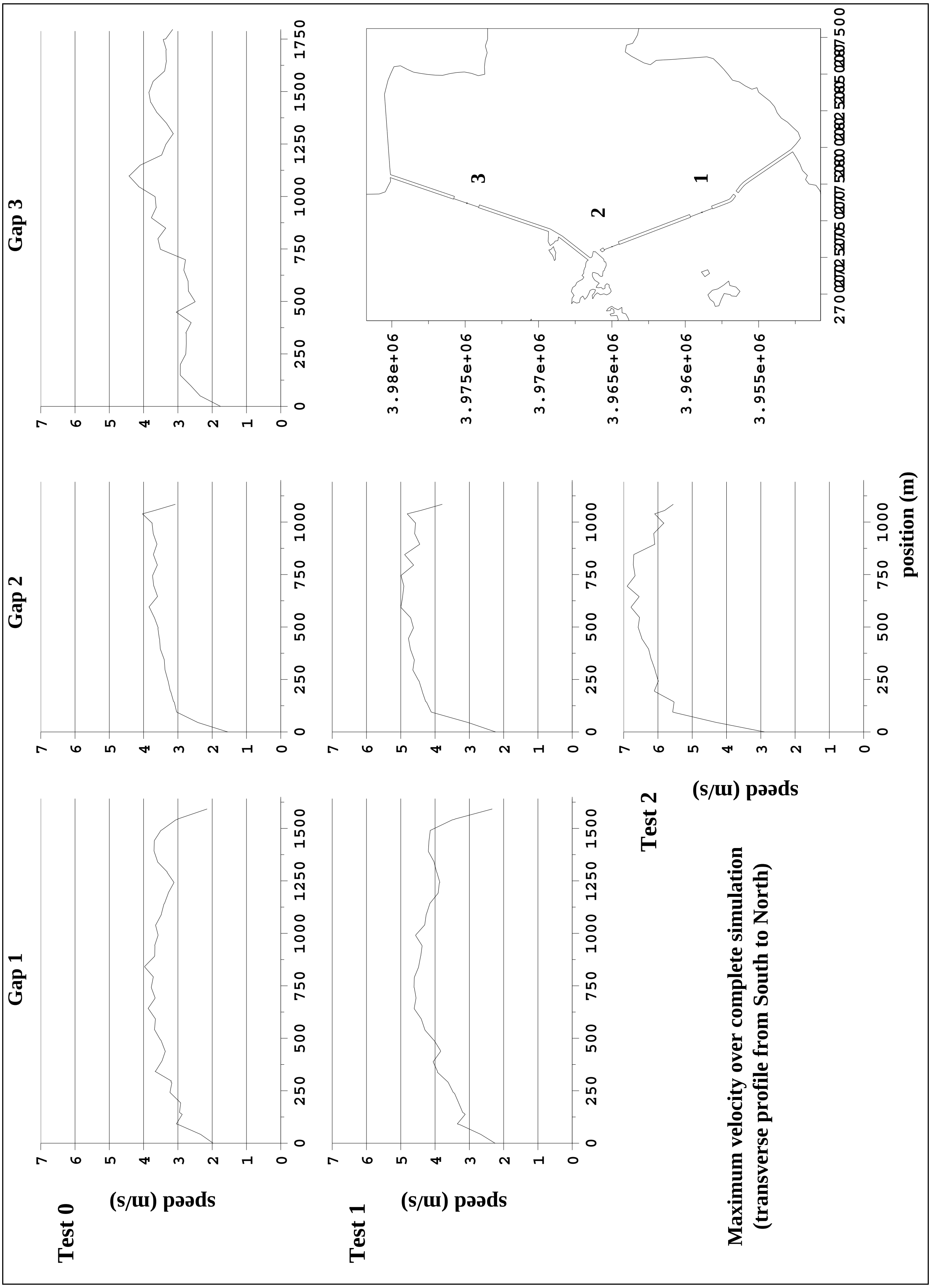

Maximum velocity over complete simulation
(transverse profile from South to North)

Figure 2.14 Transverse profiles of maximum velocities in the gaps

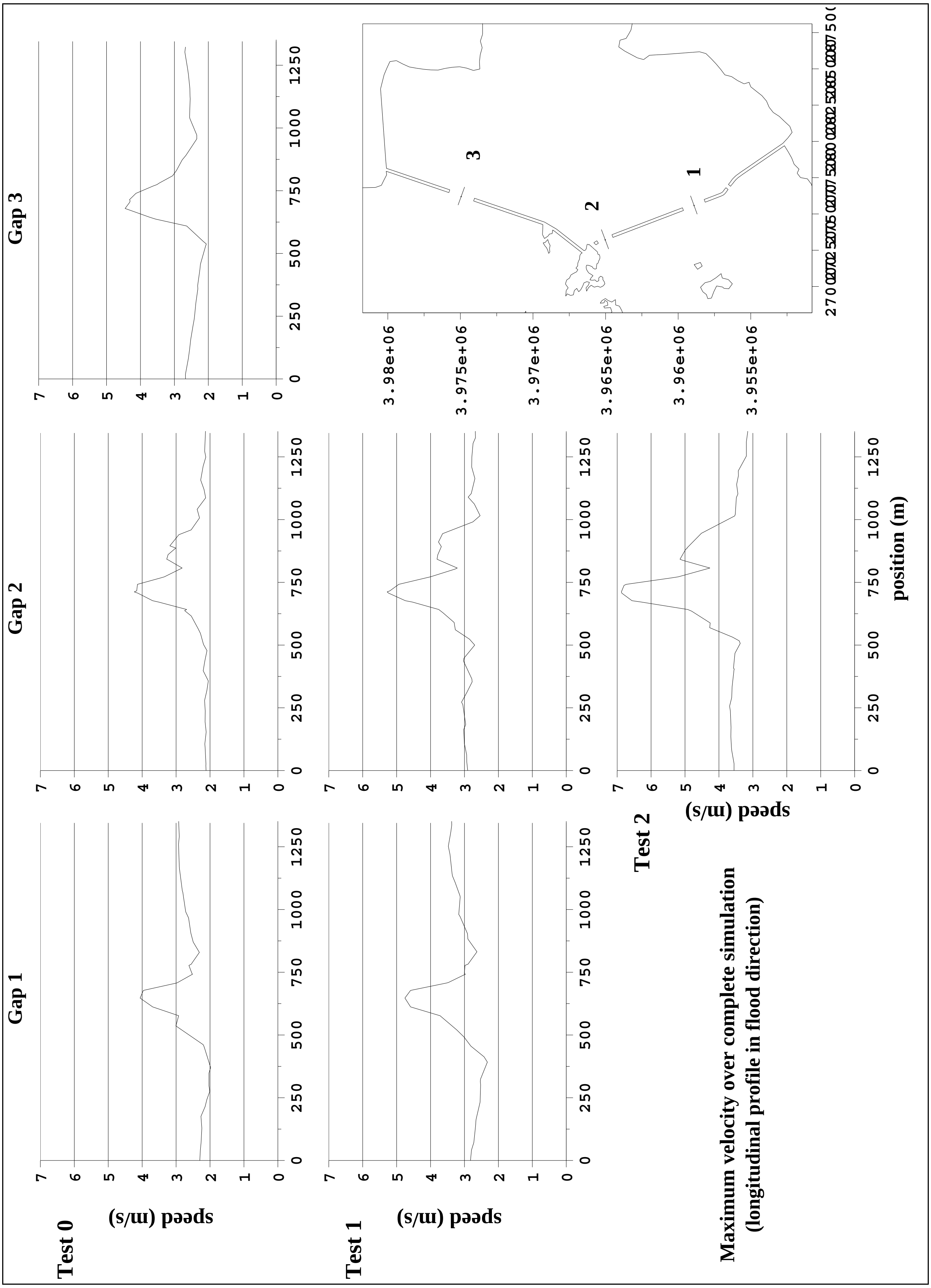

Figure 2.15 Longitudinal profiles of maximum velocities in the gaps

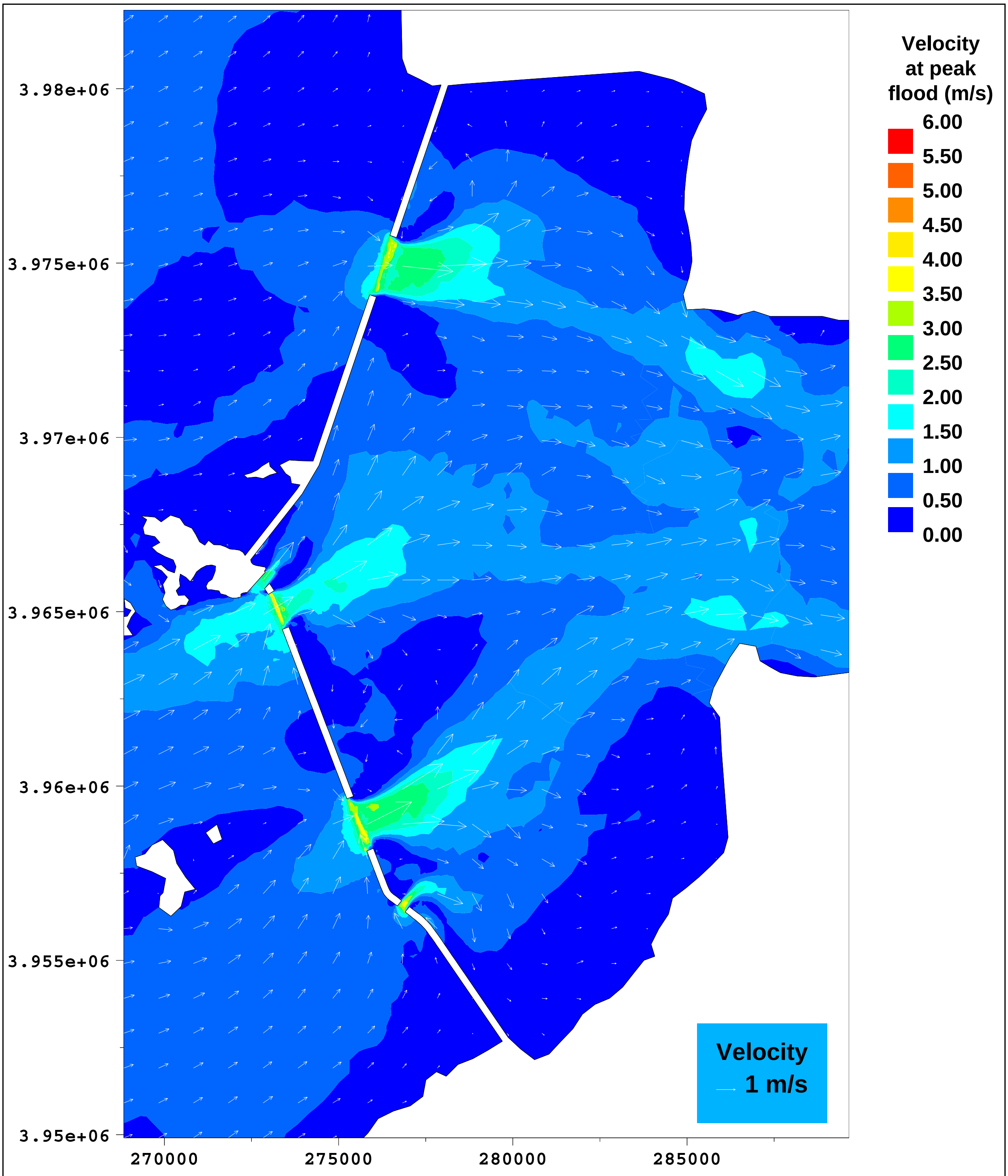

Figure 2.16 Current velocity vectors at peak flood, Test 0

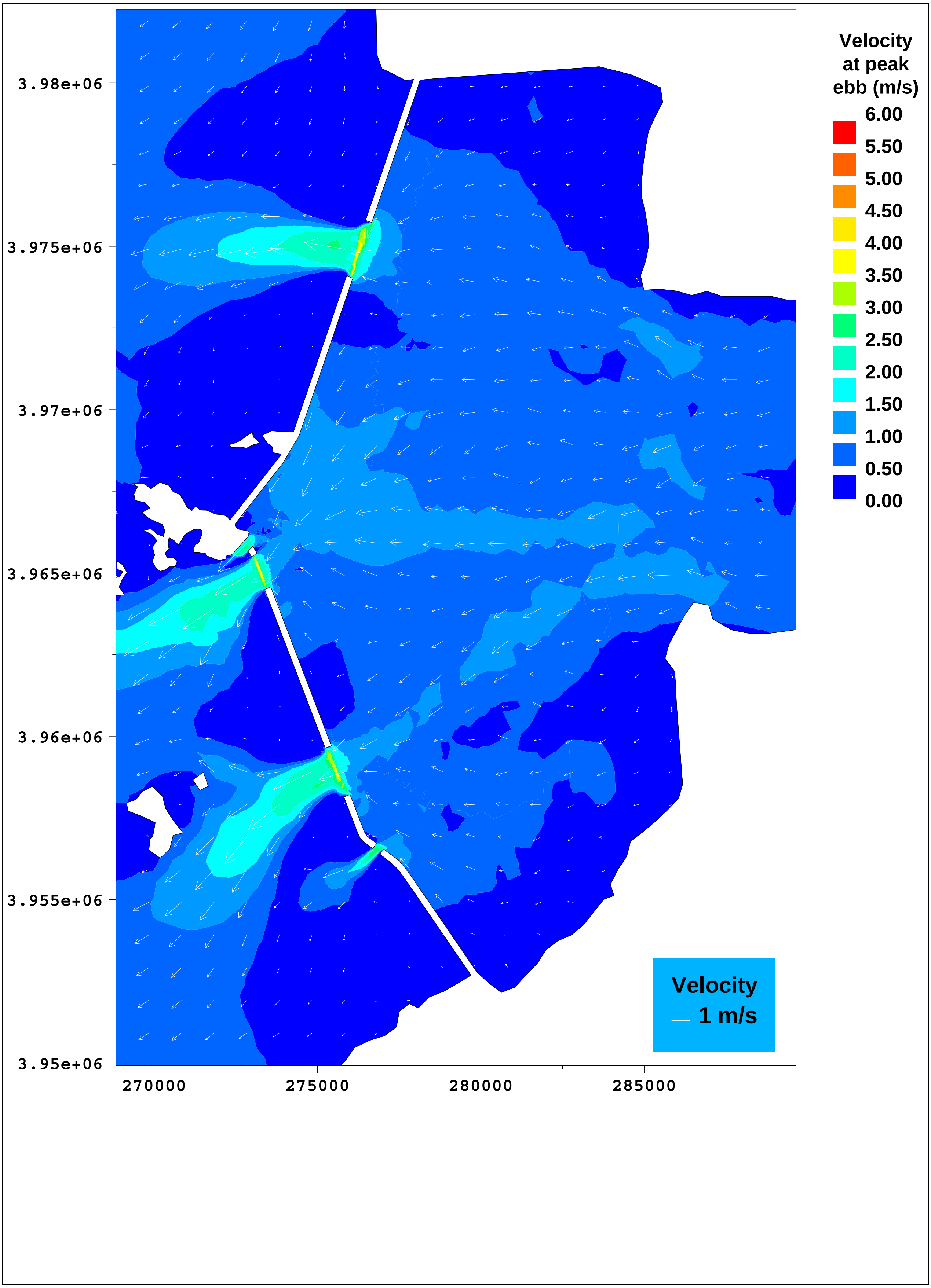

Figure 2.17 Current velocity vectors at peak ebb, Test 0

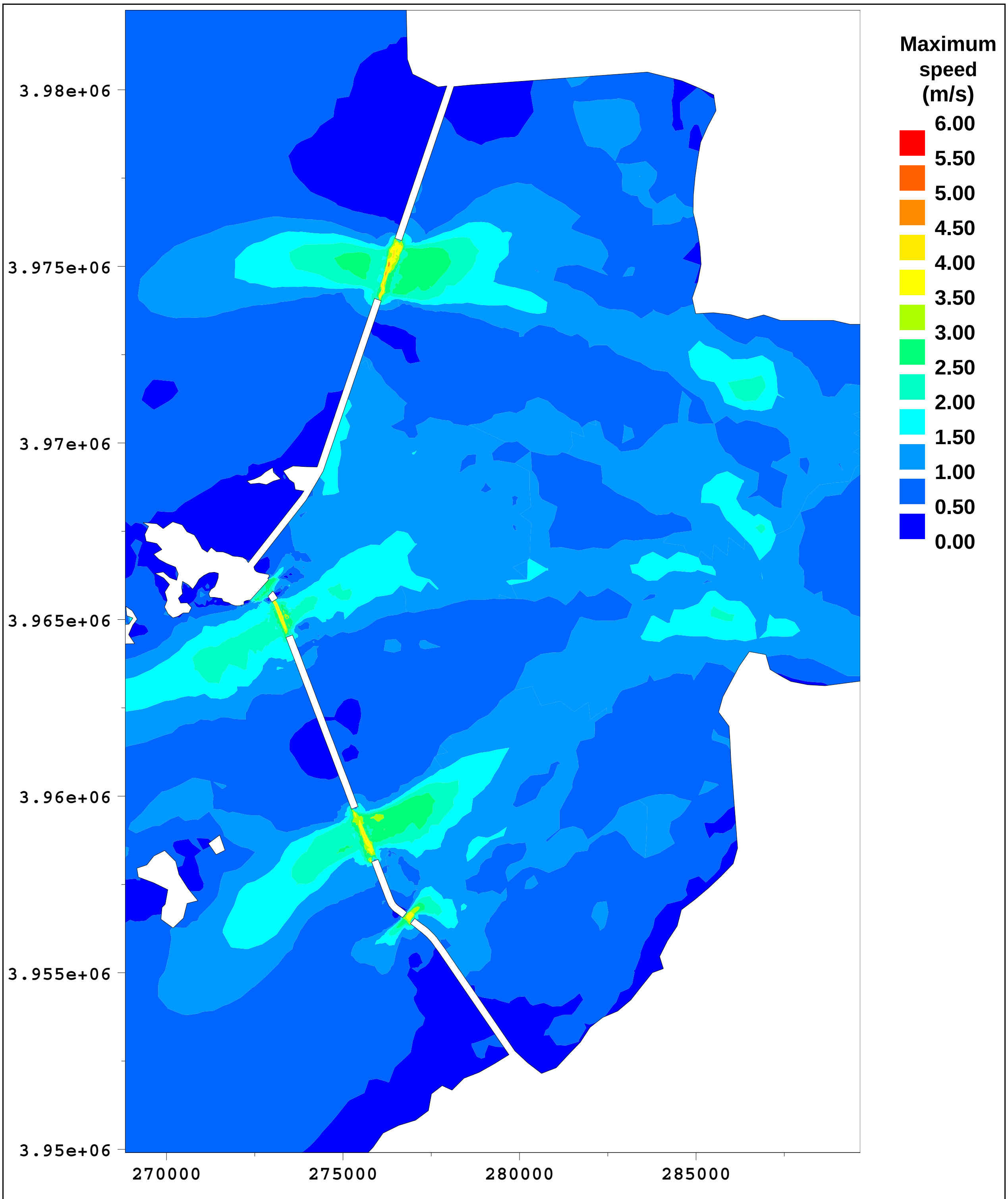

Figure 2.18 Maximum velocity distribution, Test 0

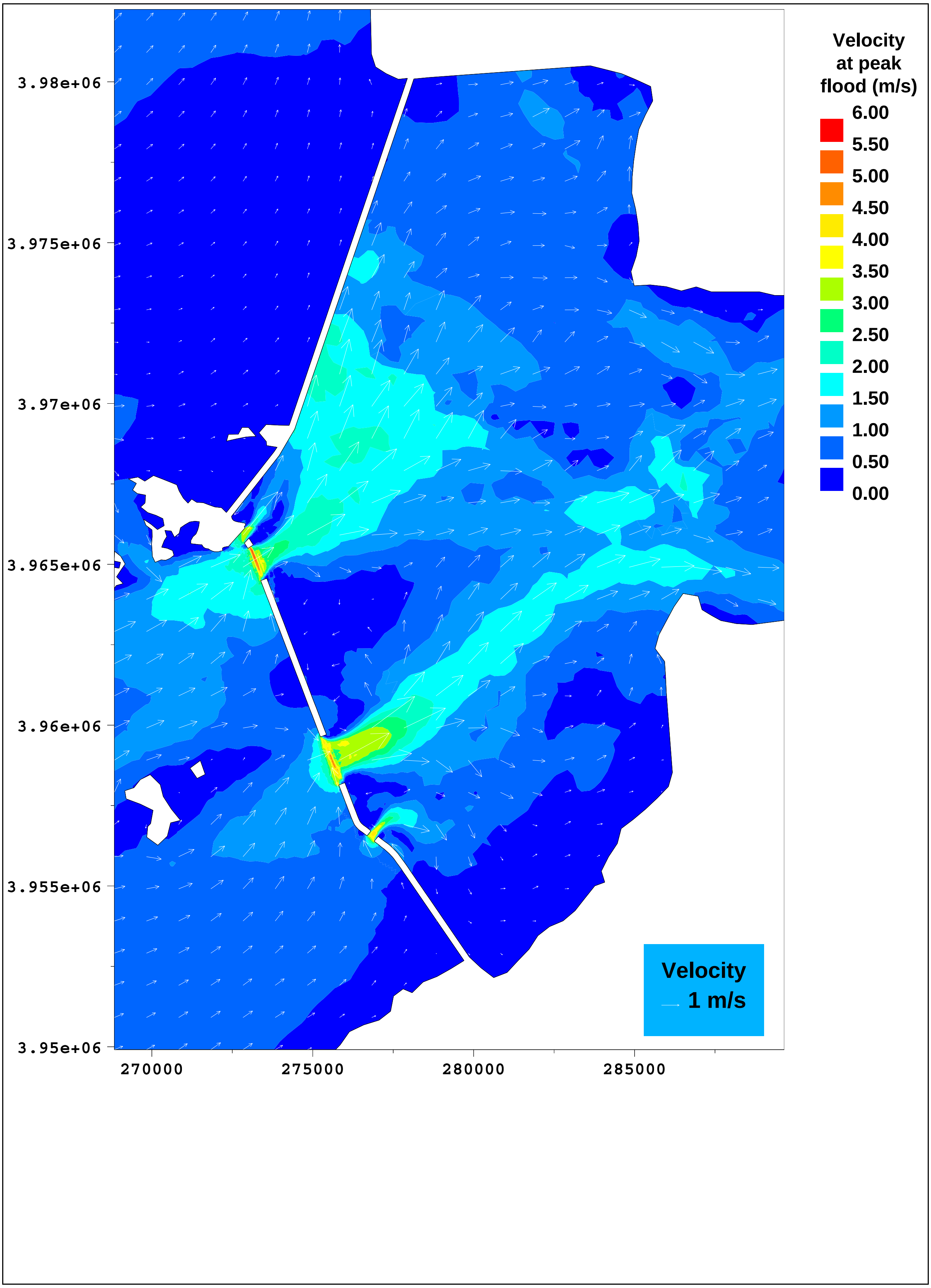

Figure 2.19 Current velocity vectors at peak flood, Test 1

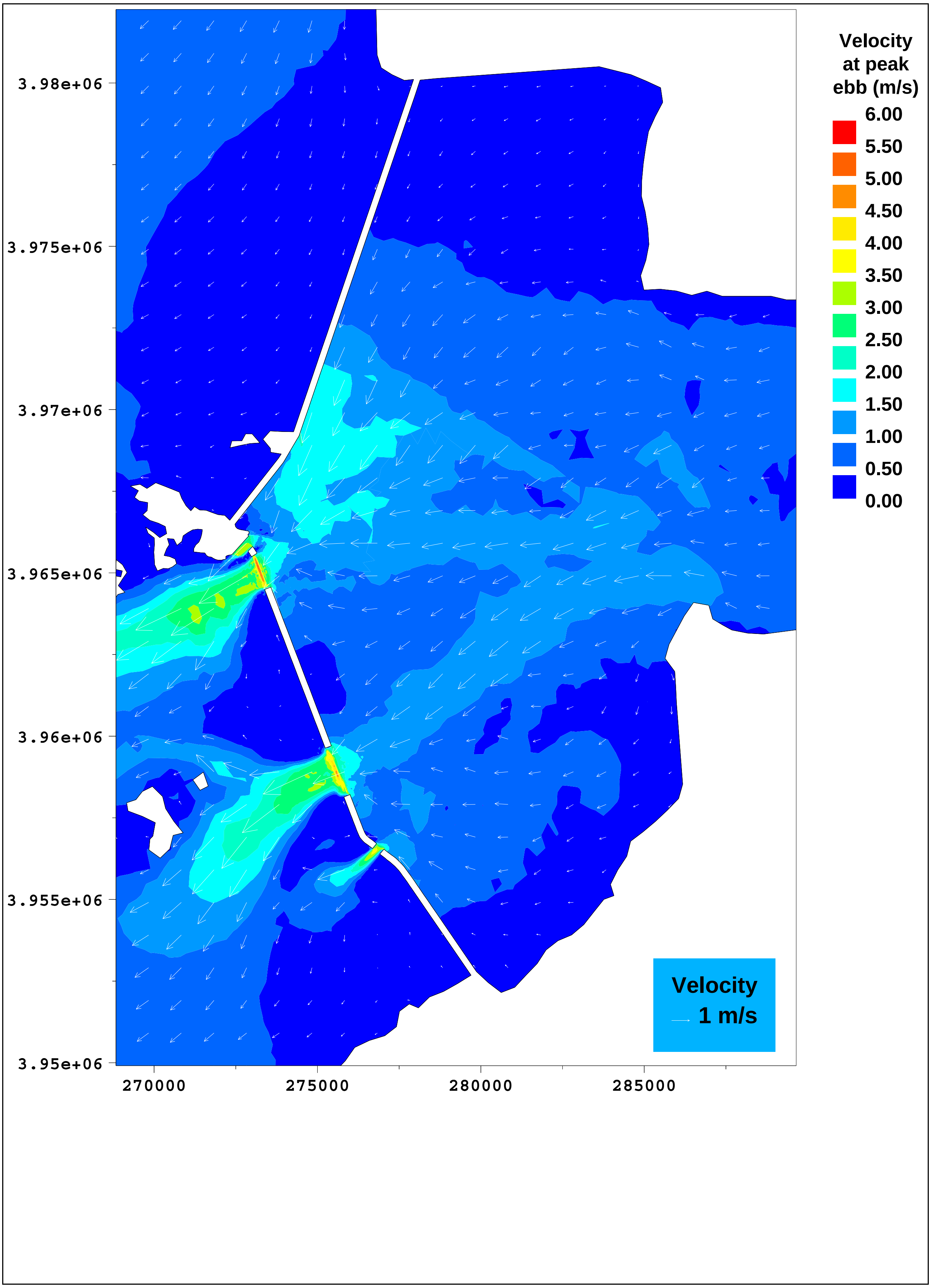

Figure 2.20 Current velocity vectors at peak ebb, Test 1

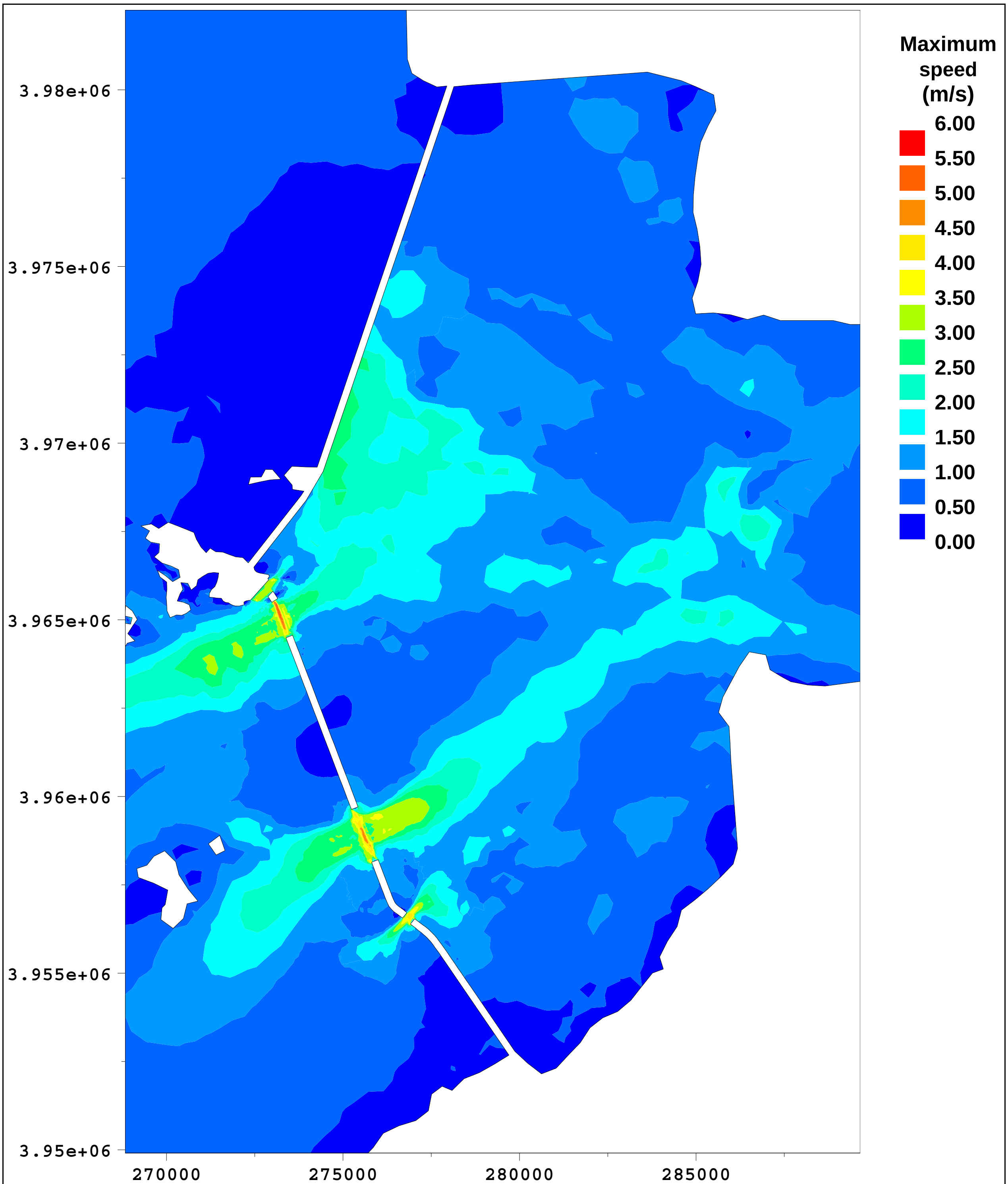

Figure 2.21 Maximum velocity distribution, Test 1

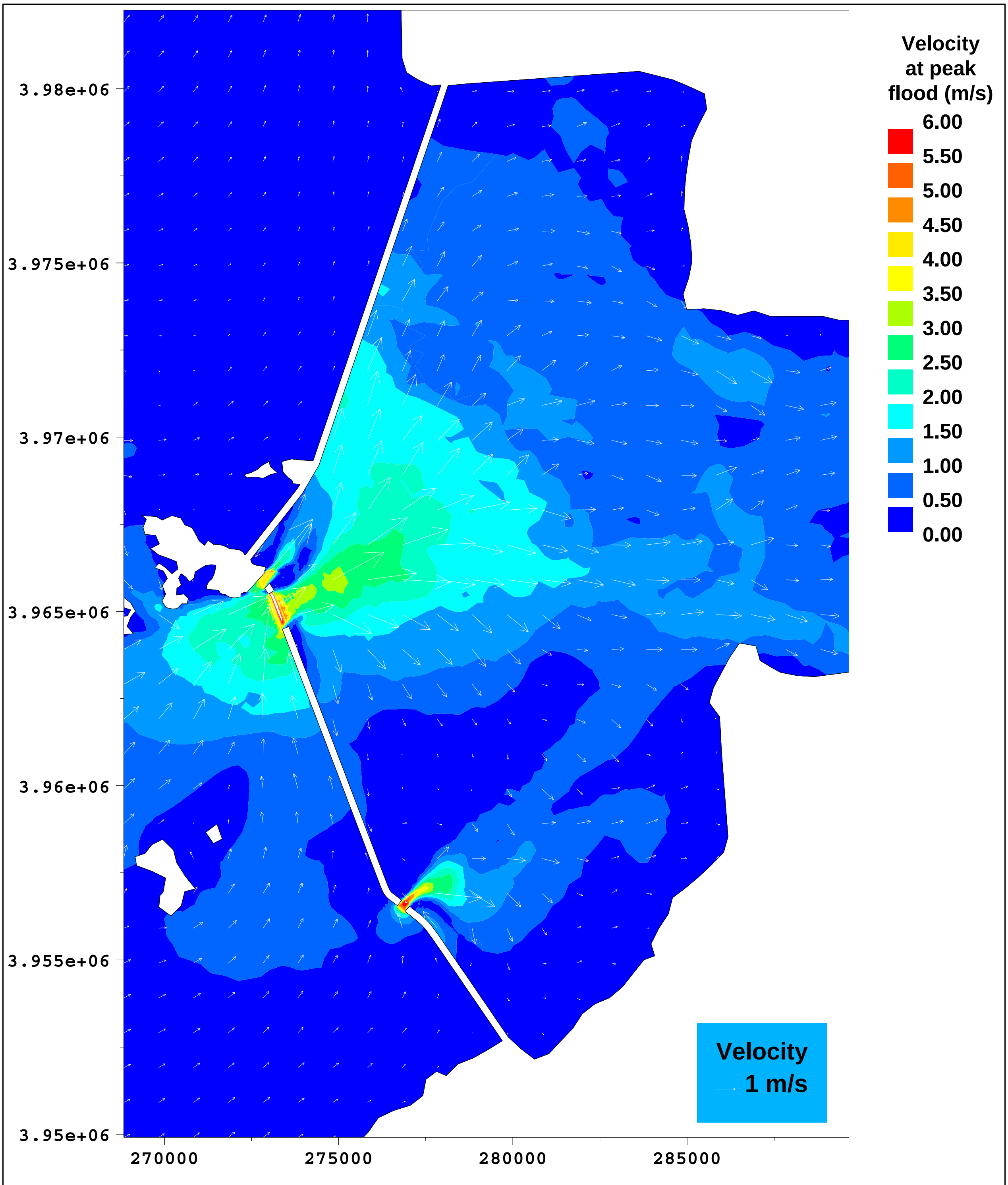

Figure 2.22 Current velocity vectors at peak flood Test 2

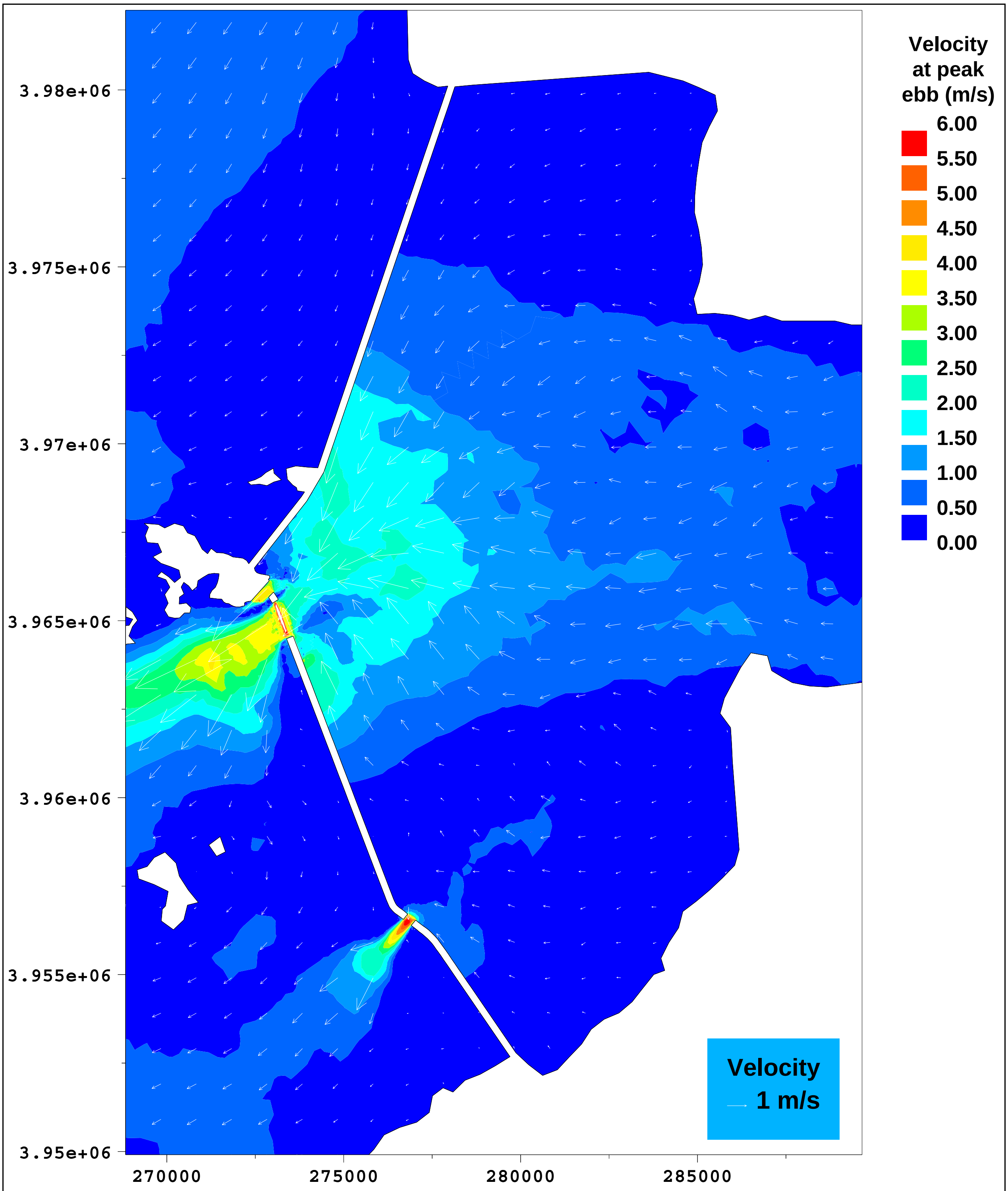

Figure 2.23 Current velocity vectors at peak ebb, Test 2

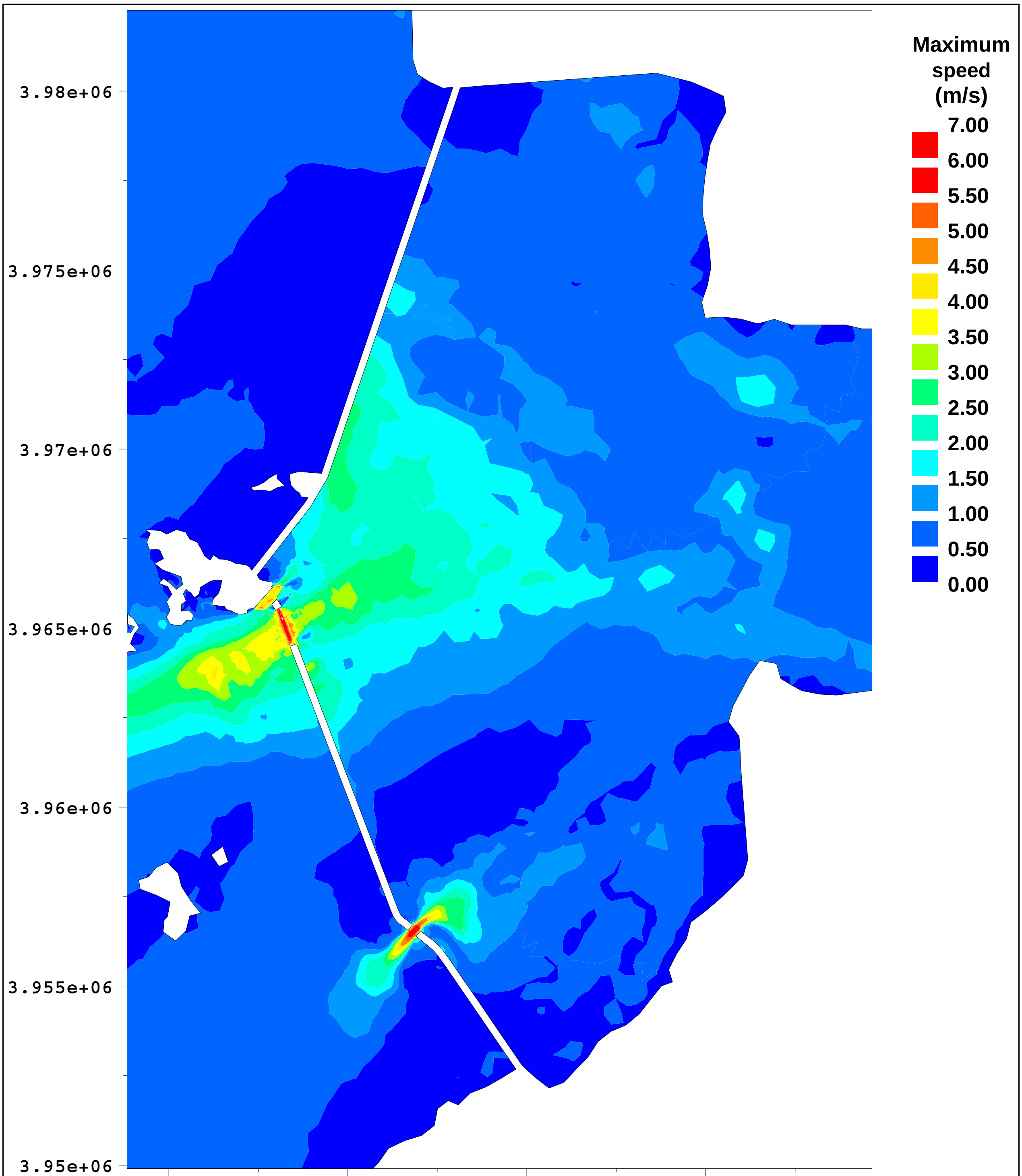

Figure 2.24 Maximum velocity distribution, Test 2

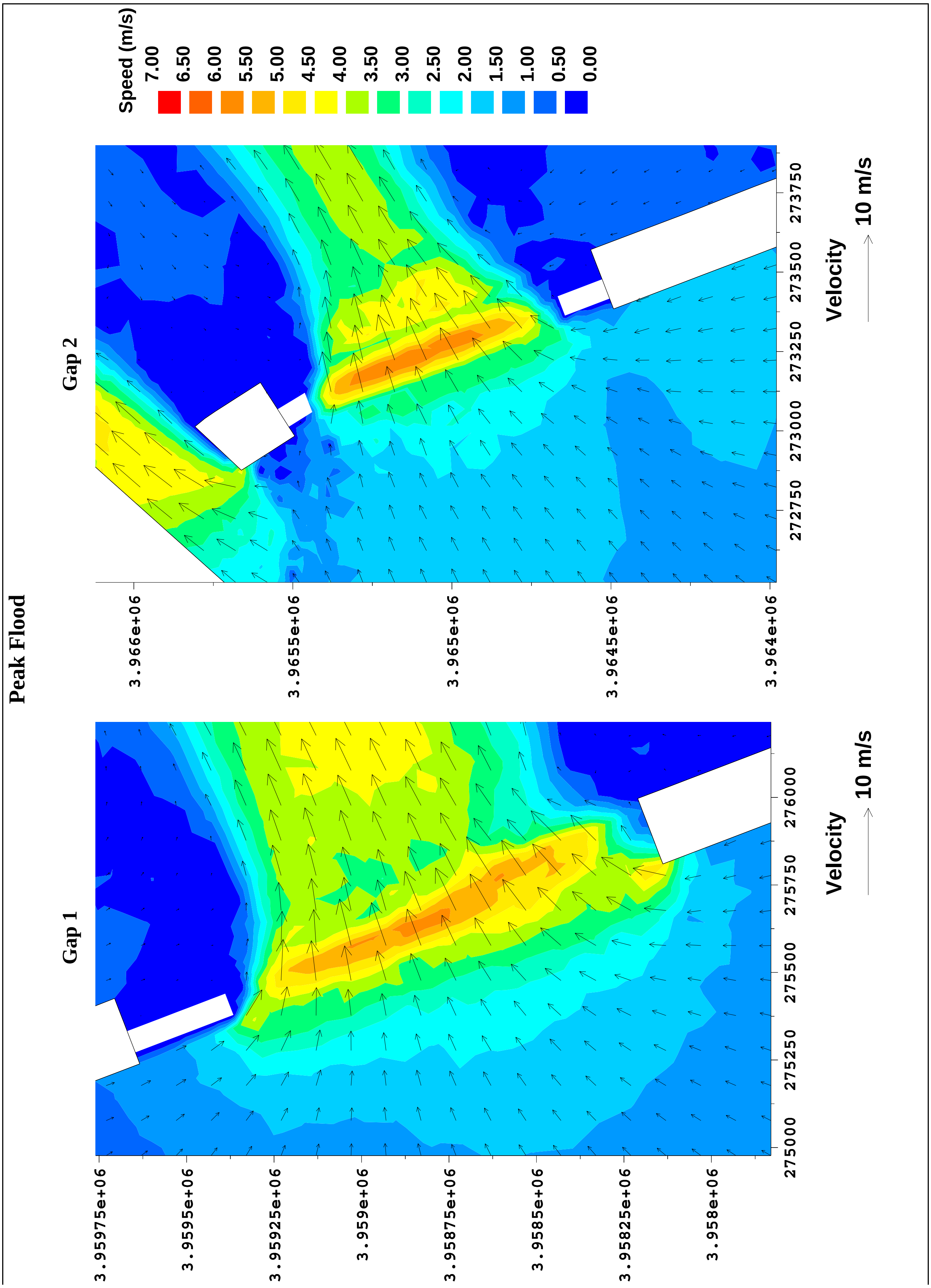

Figure 2.25 Current velocity vectors at peak flood. Spring tide. Test 3. Gap 1 : 1300 m. Gap 2 : 850 m

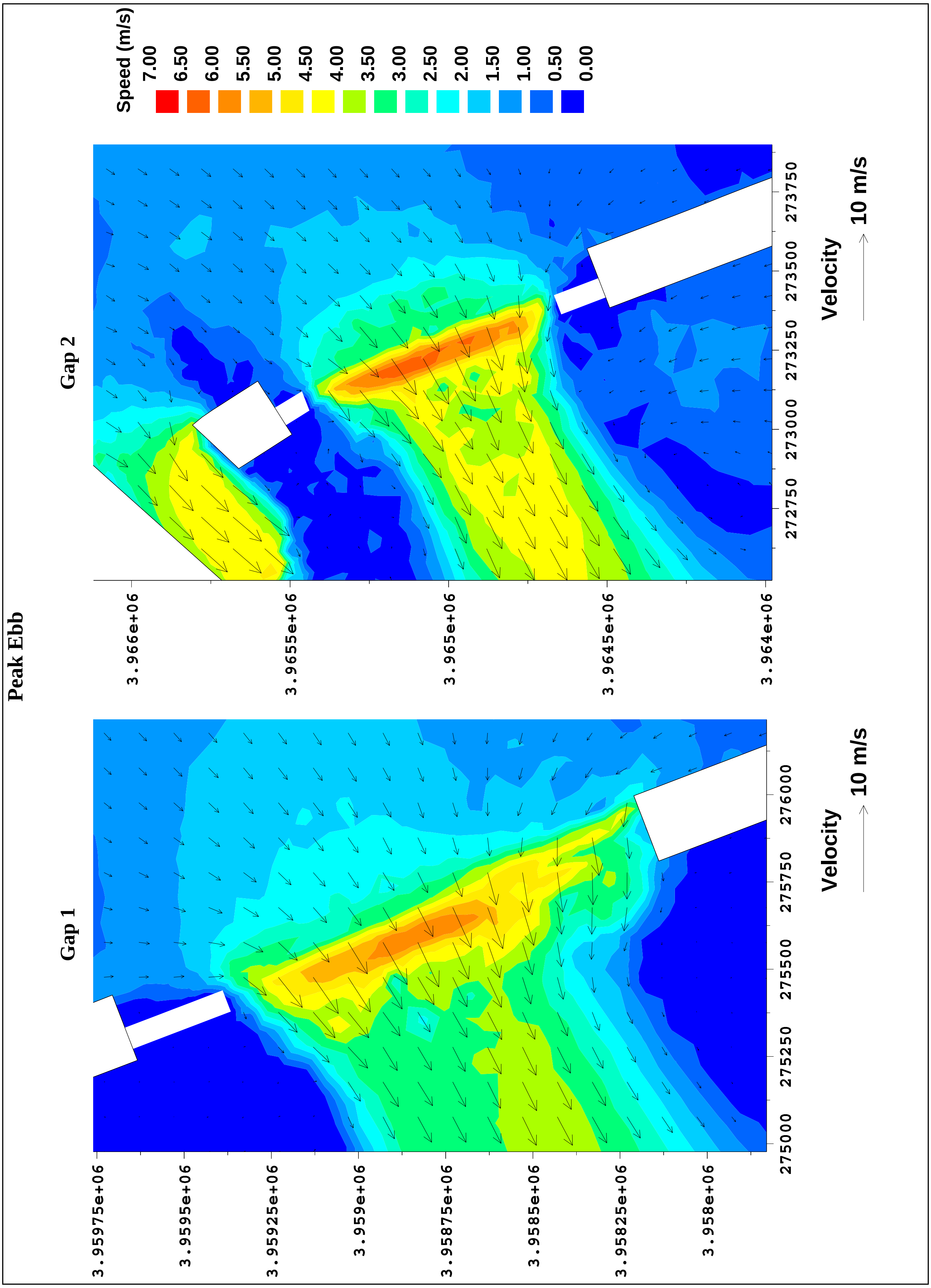

Figure 2.26 Current velocity vectors at peak ebb. Spring tide. Test 3. Gap 1 : 1300 m. Gap 2 : 850 m

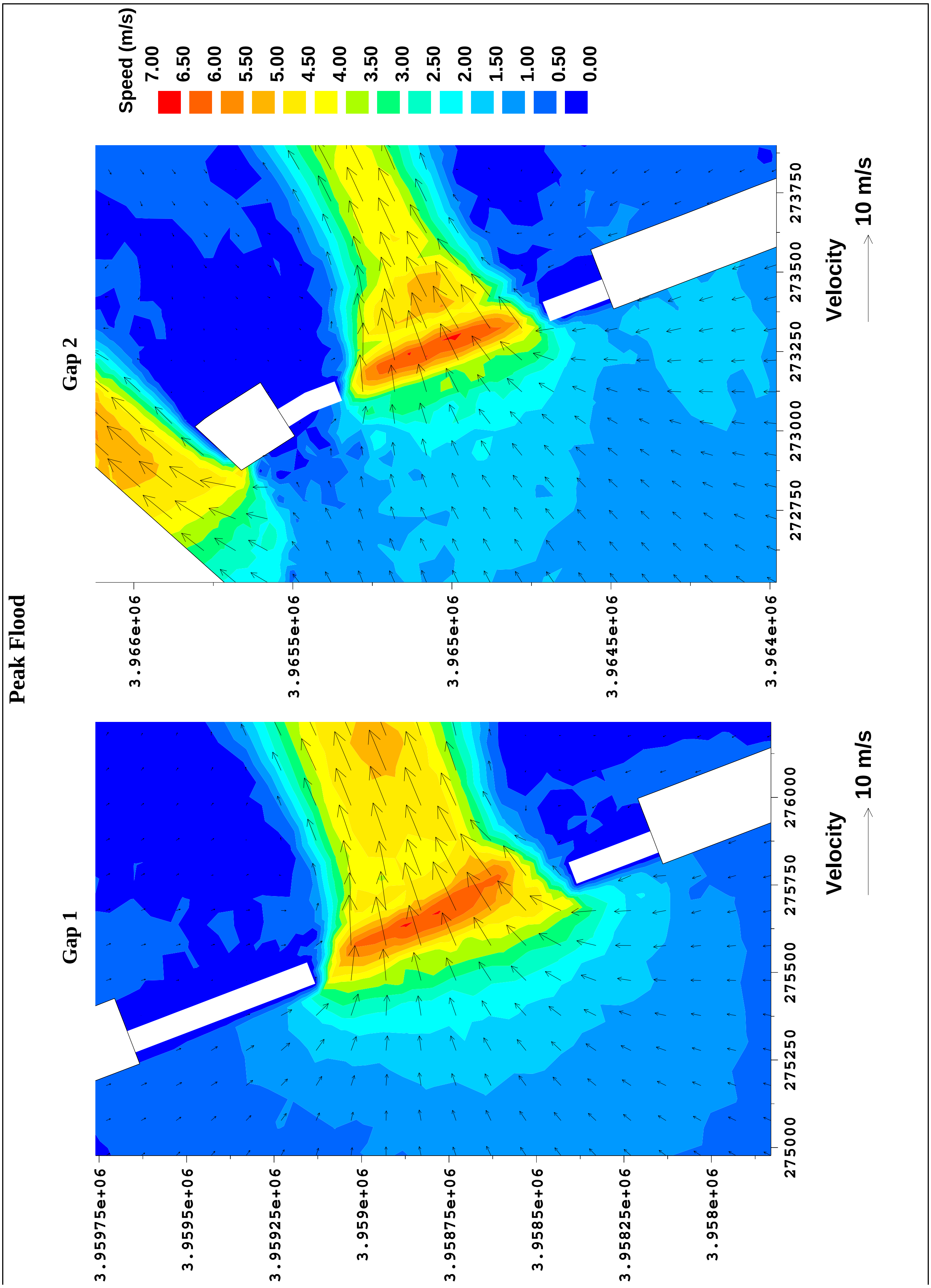

Figure 2.27 Current velocity vectors at peak flood. Spring tide. Test 4. Gap 1 : 800 m. Gap 2 : 700 m

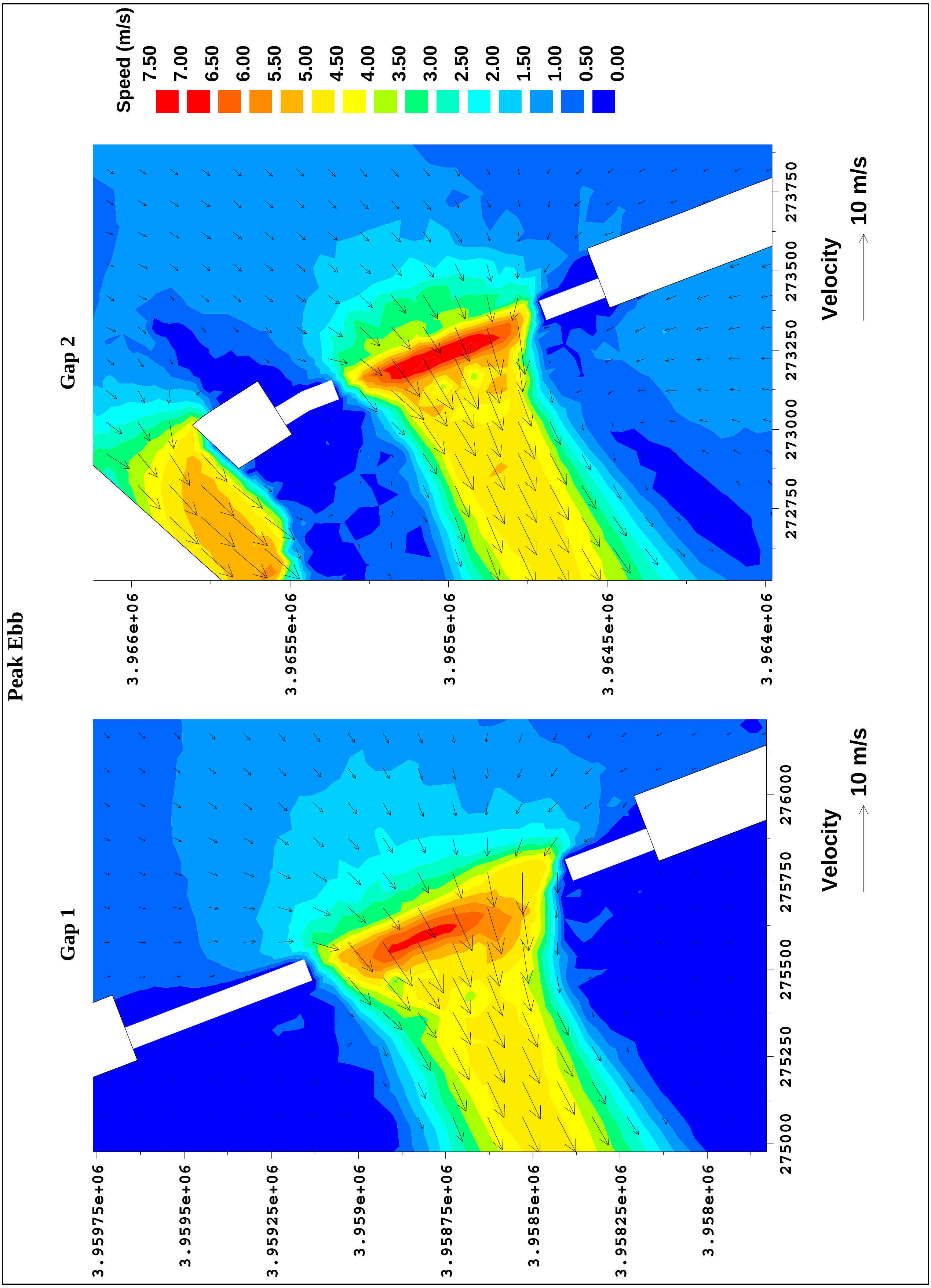

Figure 2.28 Current velocity vectors at peak ebb. Spring tide. Test 4. Gap 1 : 800 m. Gap 2 : 700 m

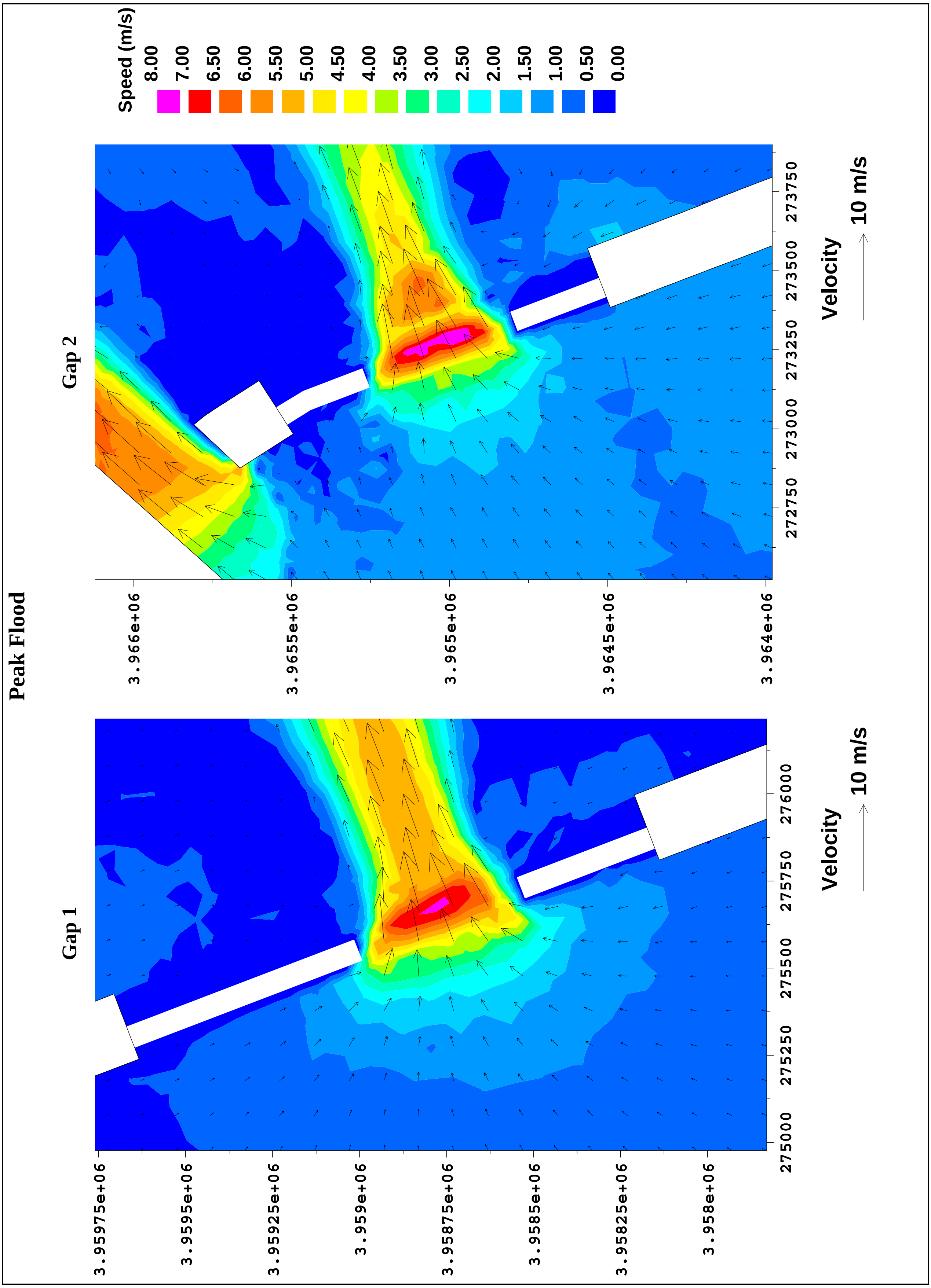

Figure 2.29 Current velocity vectors at peak flood. Spring tide. Test 5. Gap 1 : 500 m. Gap 2 : 500 m

HR Wallingford

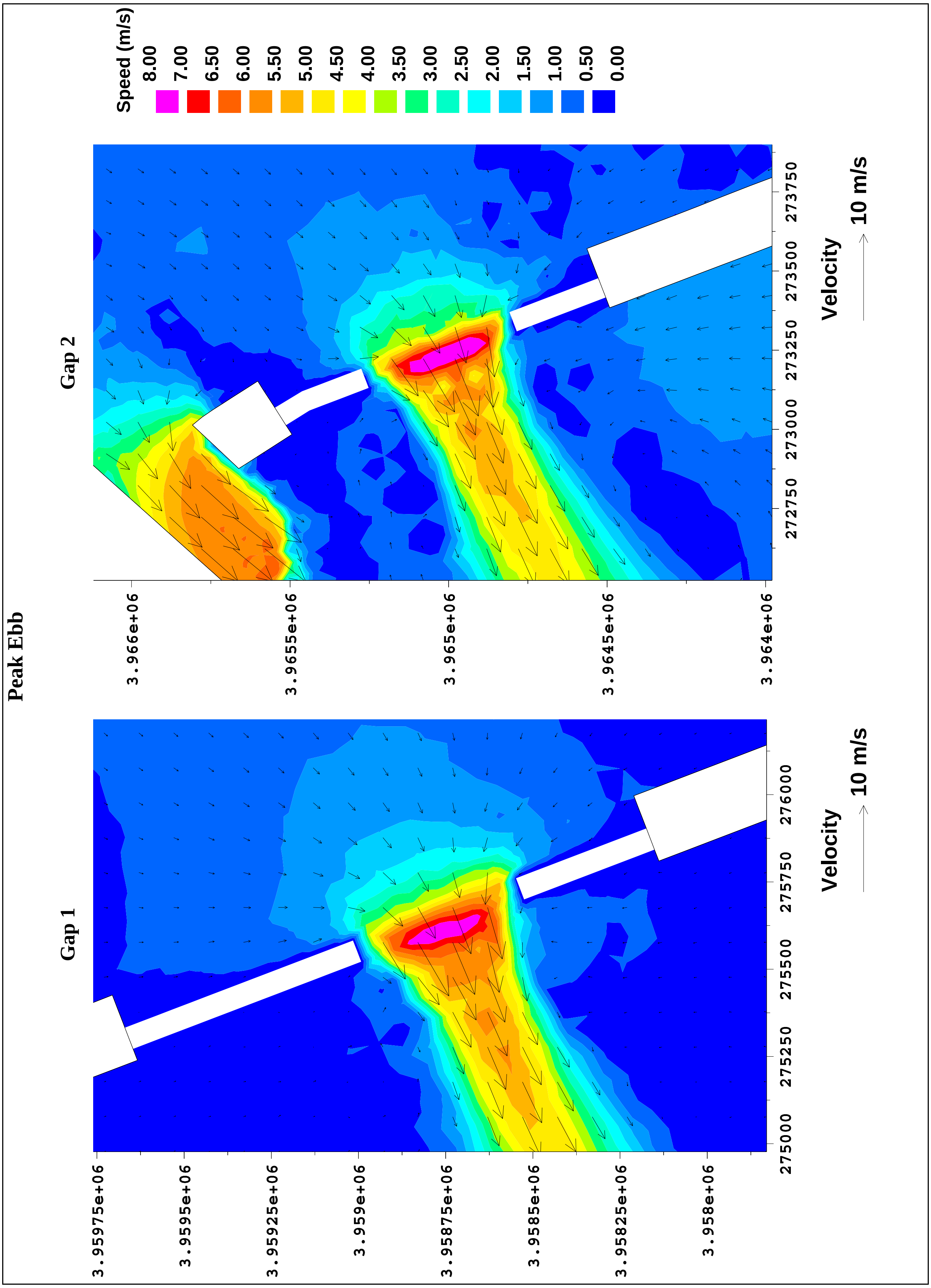

Figure 2.30 Current velocity vectors at peak ebb. Spring tide. Test 5. Gap 1 : 500 m. Gap 2 : 500 m

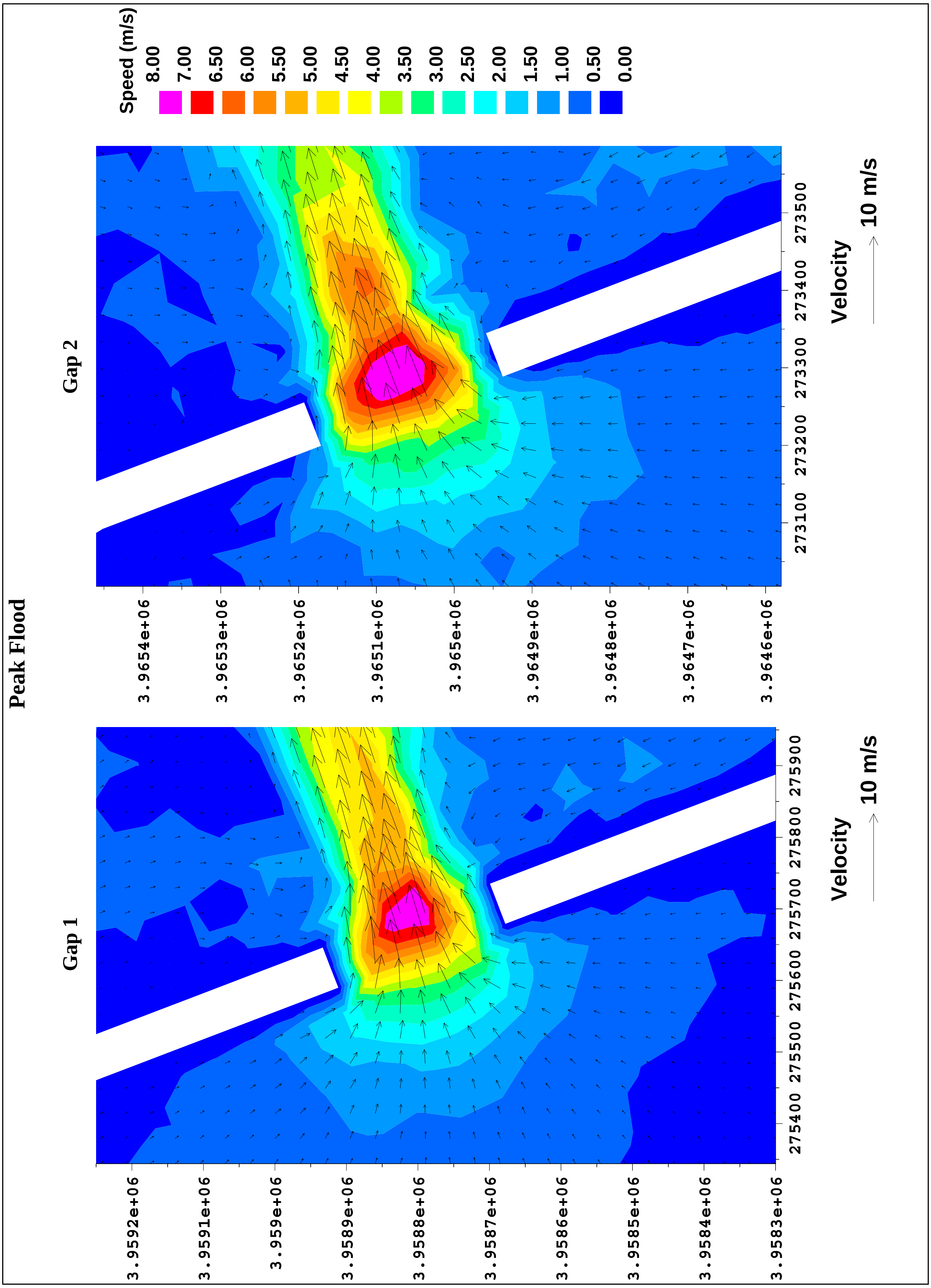

Figure 2.31 Current velocity vectors at peak flood. Spring tide. Test 8. Gap 1 : 200 m. Gap 2 : 200 m

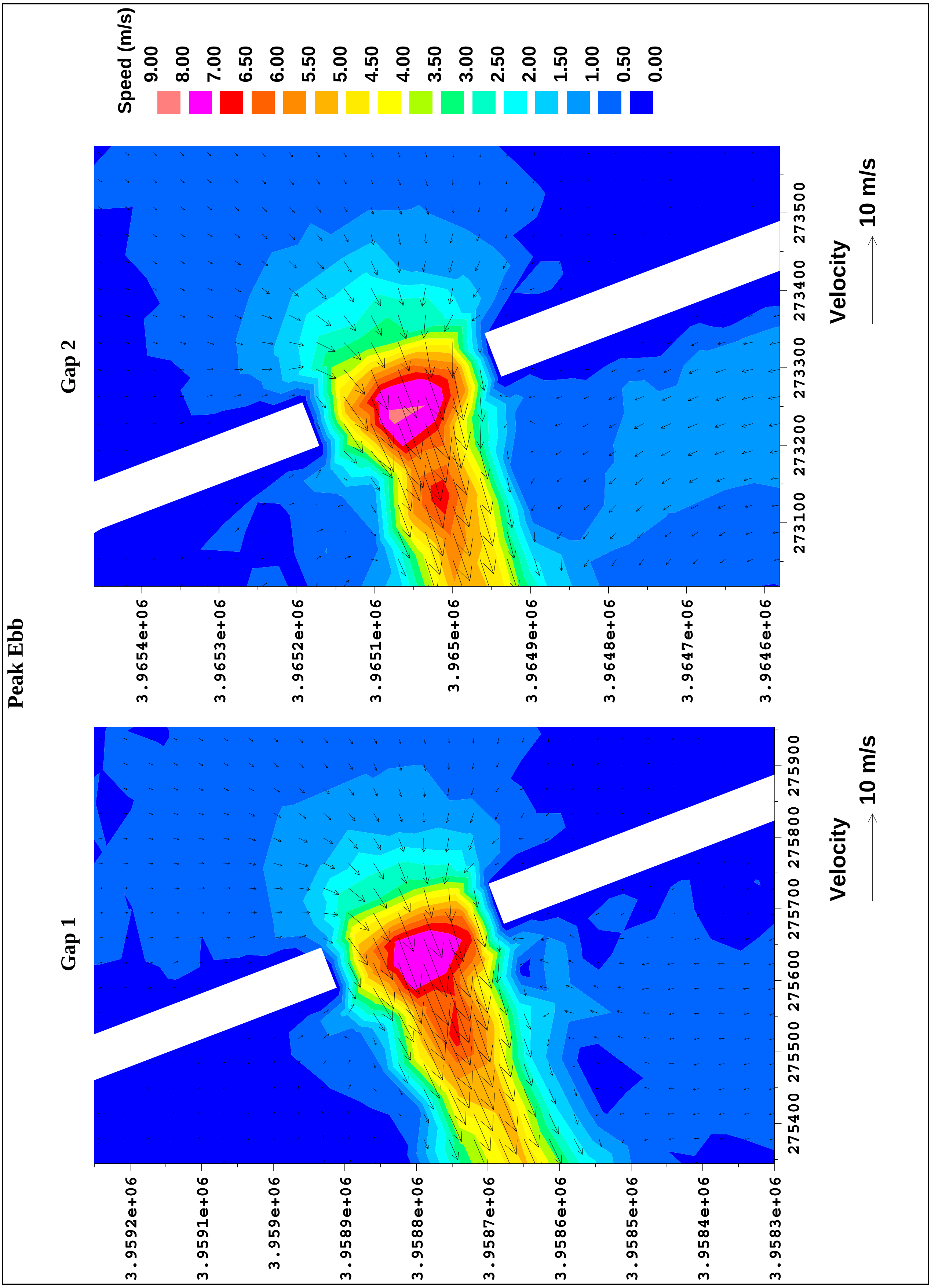

Figure 2.32 Current velocity vectors at peak ebb. Spring tide. Test 8. Gap 1 : 200 m. Gap 2 : 200 m

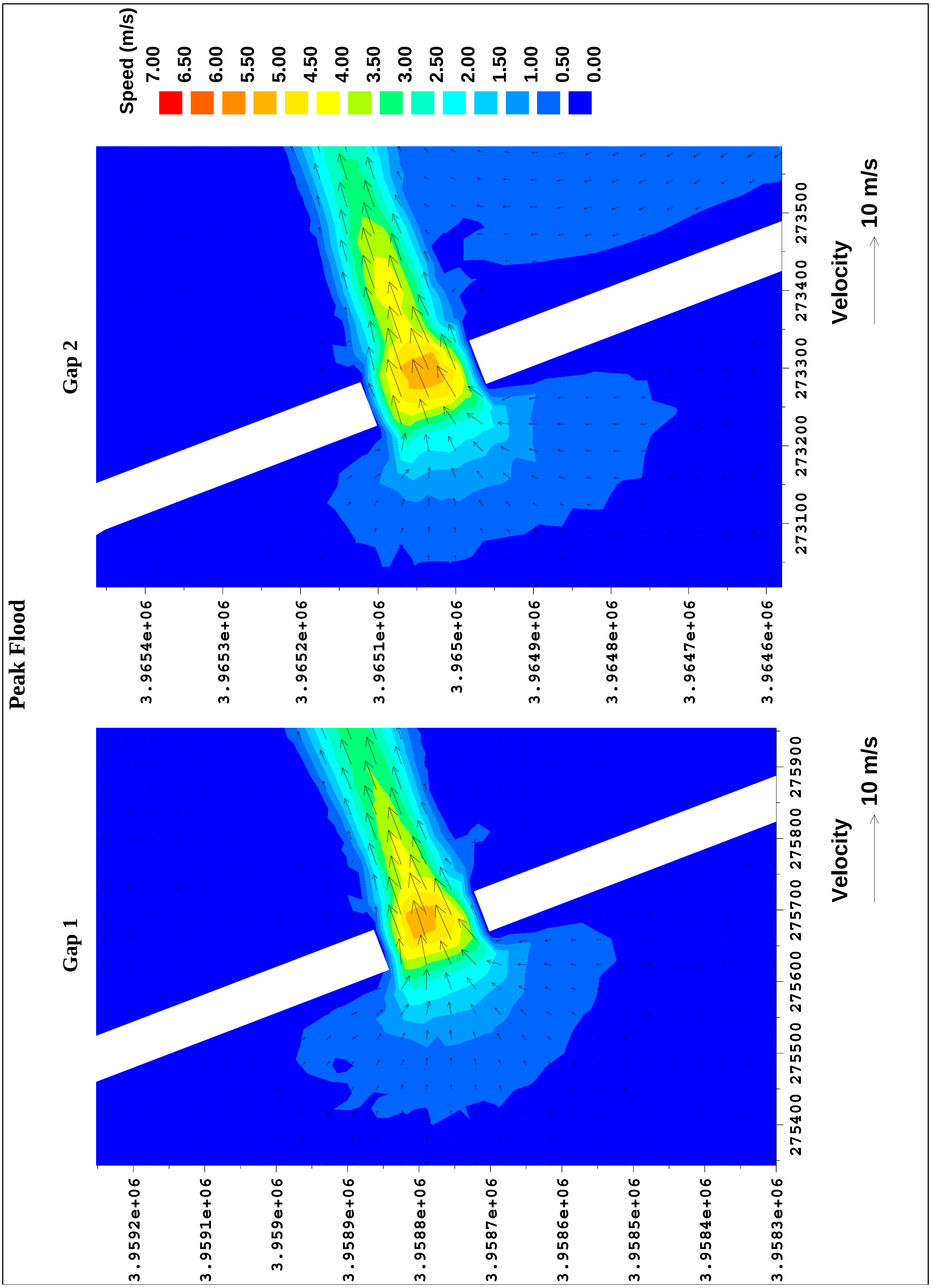

Figure 2.33 Current velocity vectors at peak flood. Neap tide. Test 6. Gap 1 : 100 m. Gap 2 : 100 m

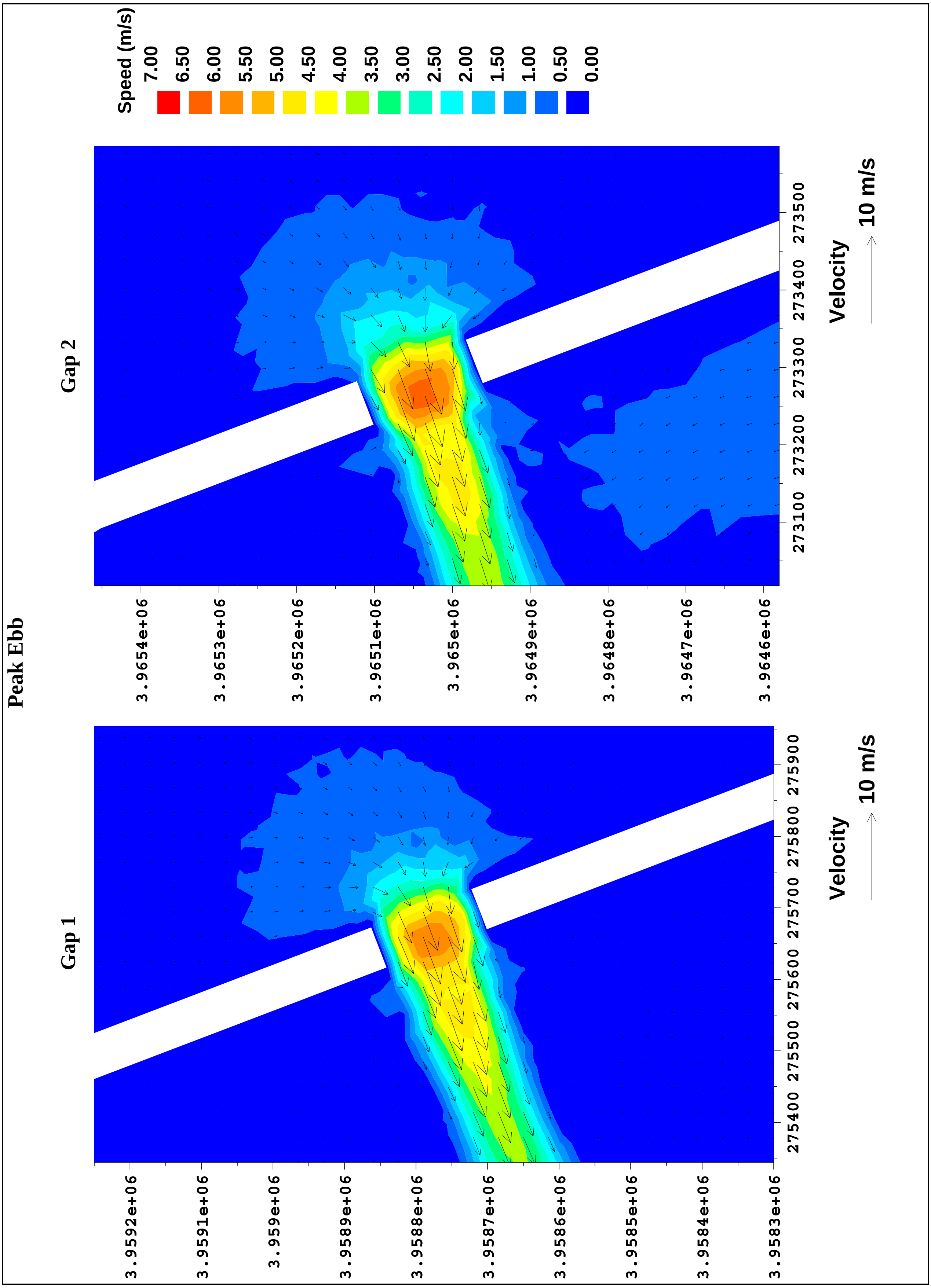

Figure 2.34 Current velocity vectors at peak ebb. Neap tide. Test 6. Gap 1 : 100 m. Gap 2 : 100 m

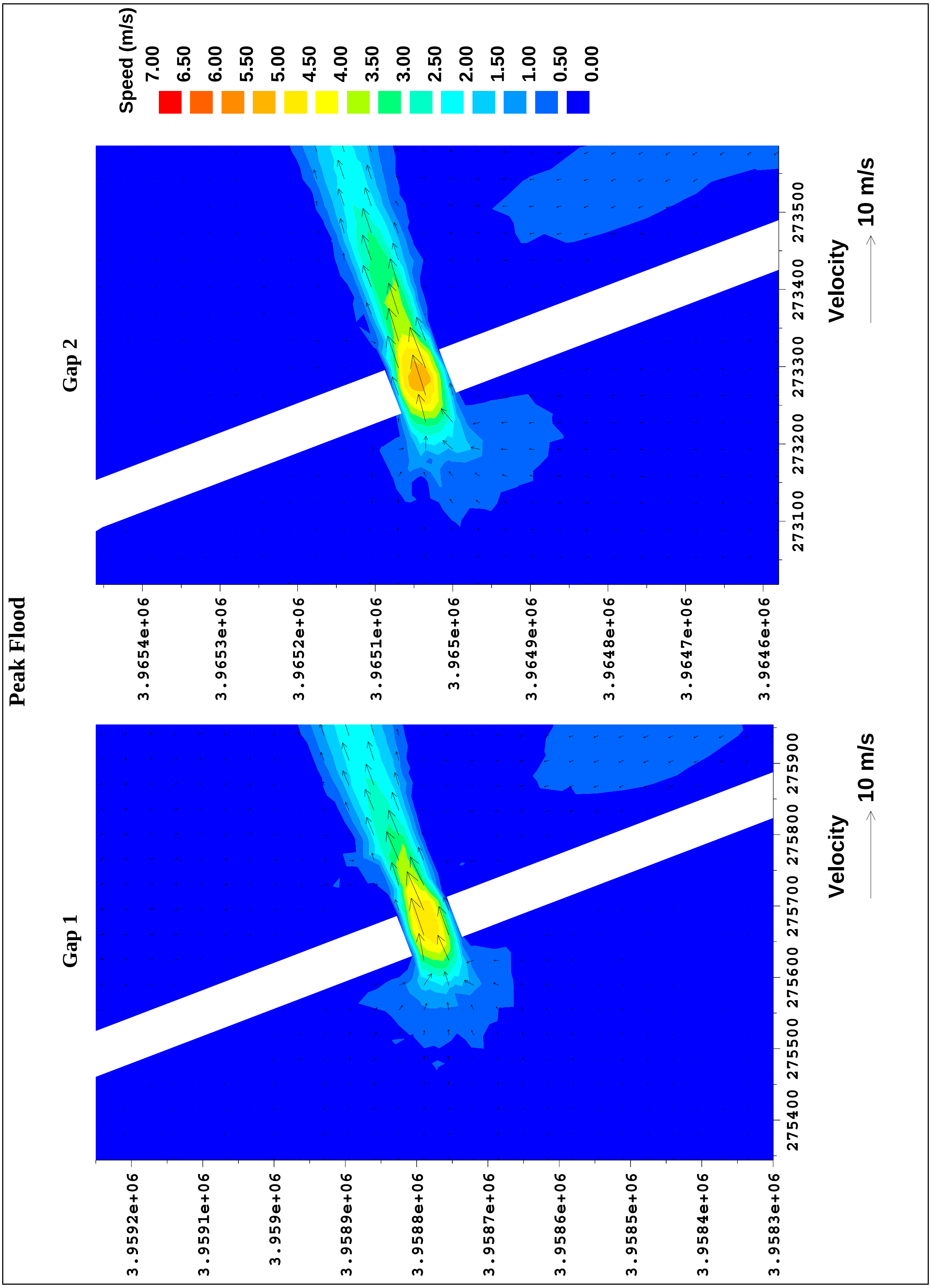

Figure 2.35 Current velocity vectors at peak flood. Neap tide. Test 9. Gap 1 : 50 m. Gap 2 : 50 m

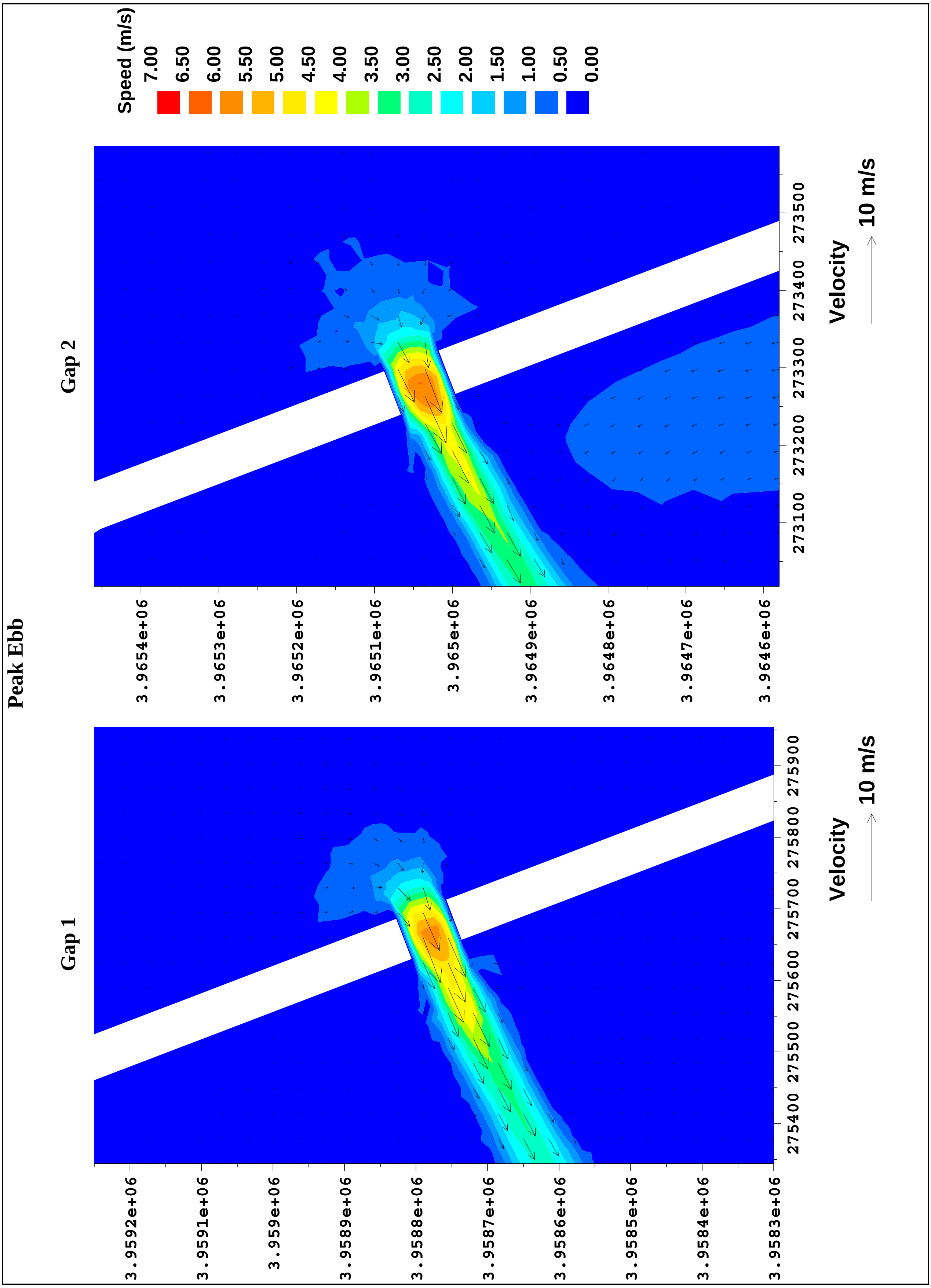

Figure 2.36 Current velocity vectors at peak ebb. Neap tide. Test 9. Gap 1 : 50 m. Gap 2 : 50 m

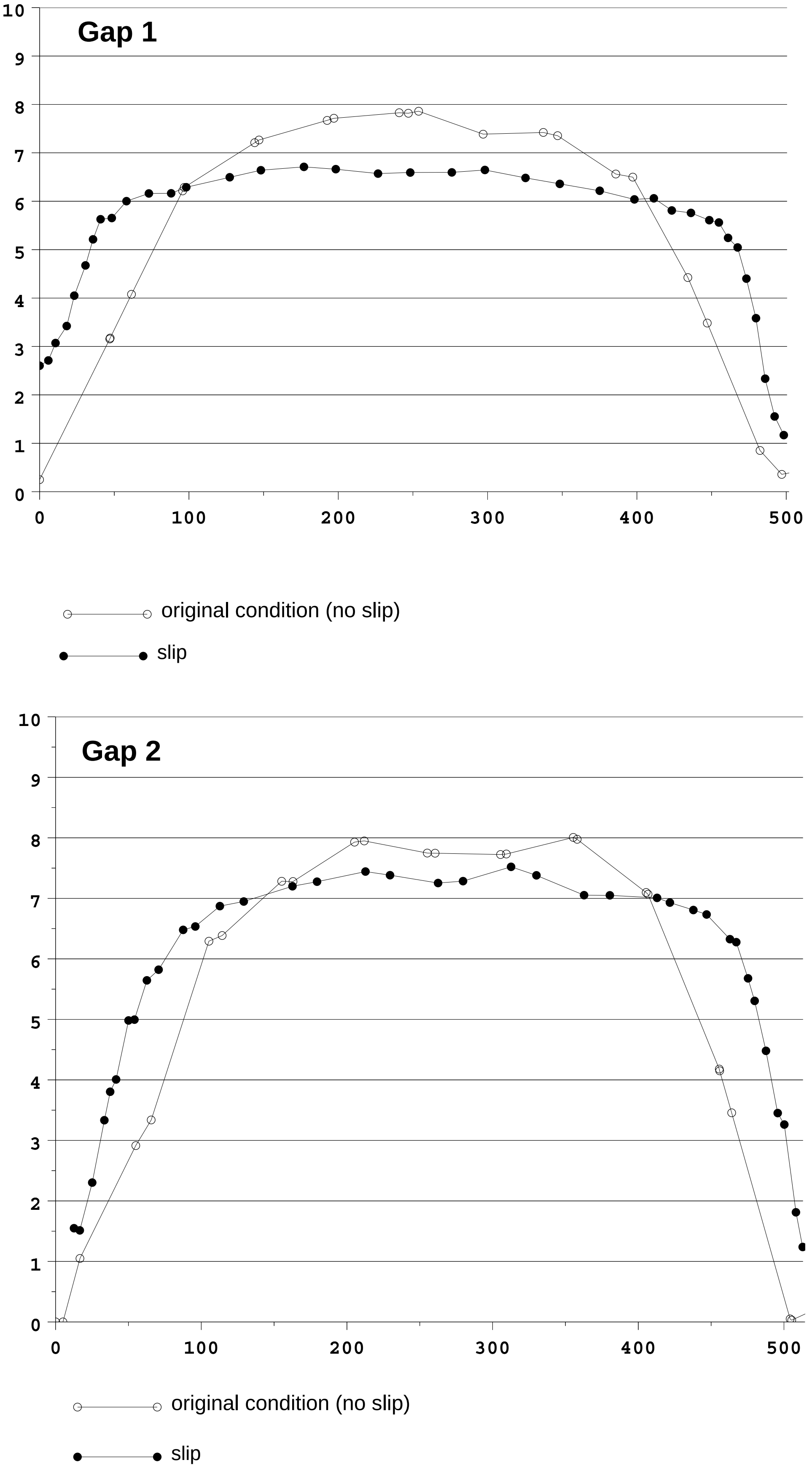

Figure 2.37 Speed profiles from north to south at peak ebb. Test 5, in two different conditions

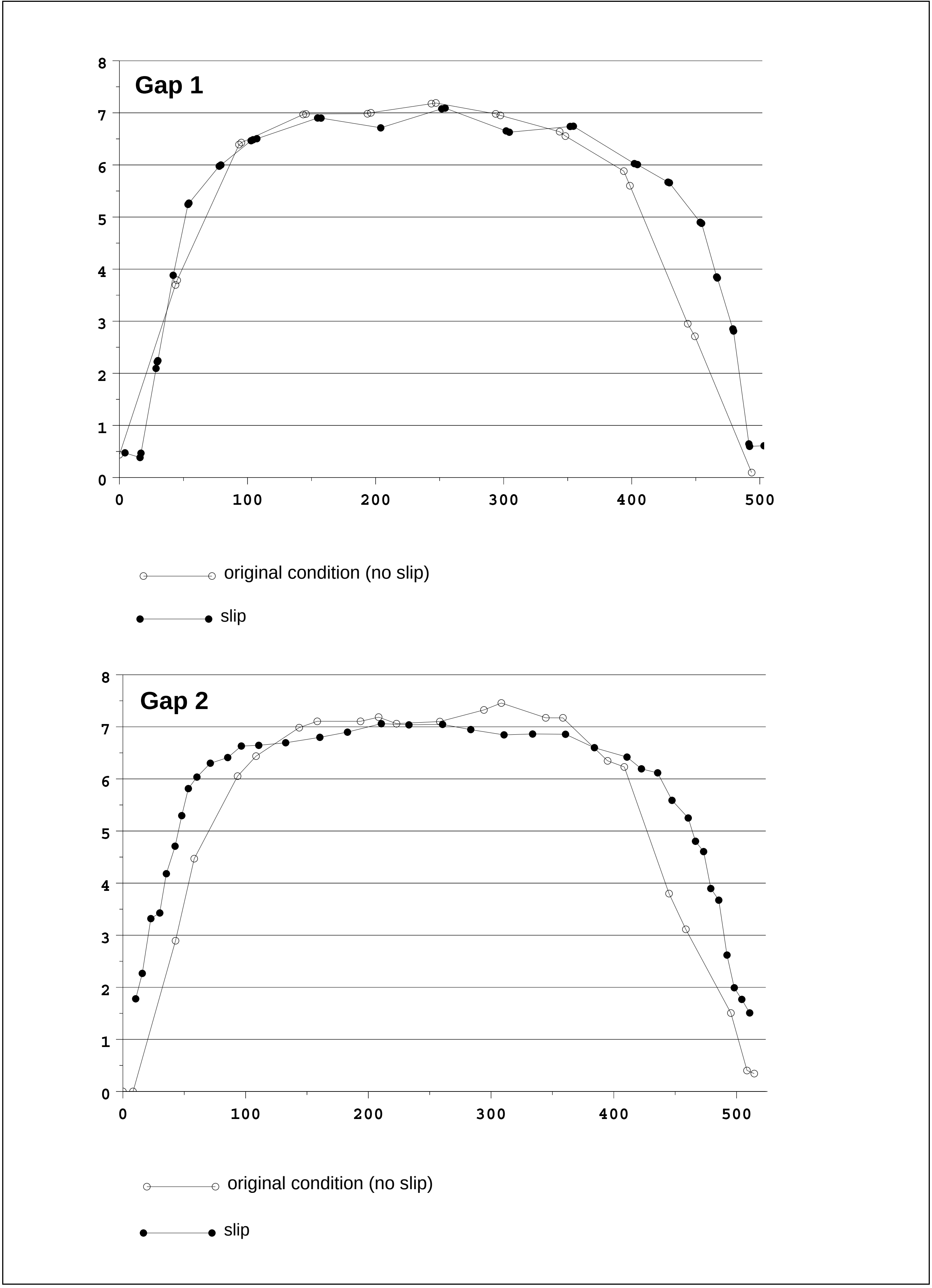

Figure 2.38 Speed profiles from north to south at peak flood. Test 5, in two different conditions

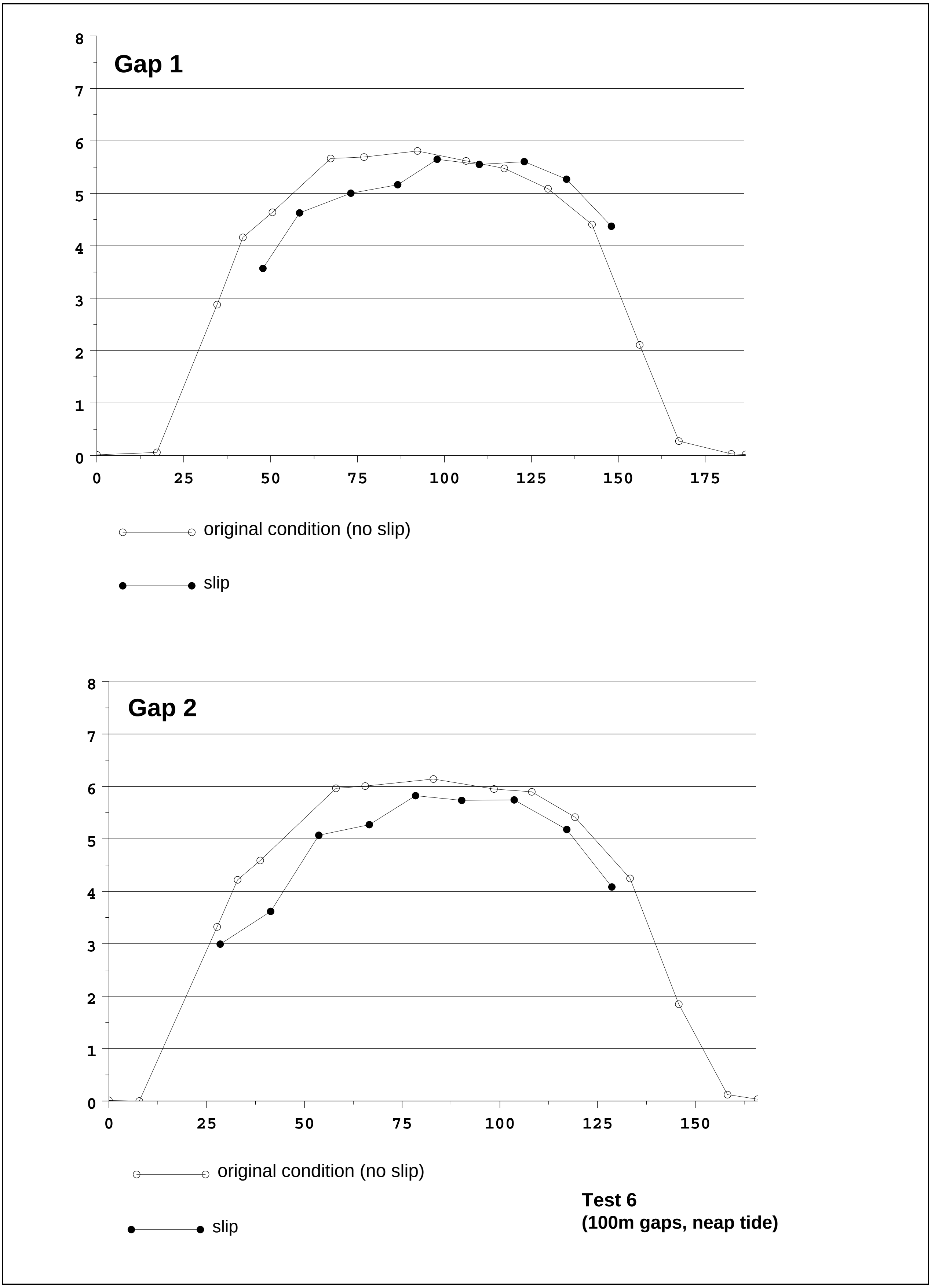

Figure 2.39 Speed profiles from north to south at peak ebb. Test 6, in two different conditions

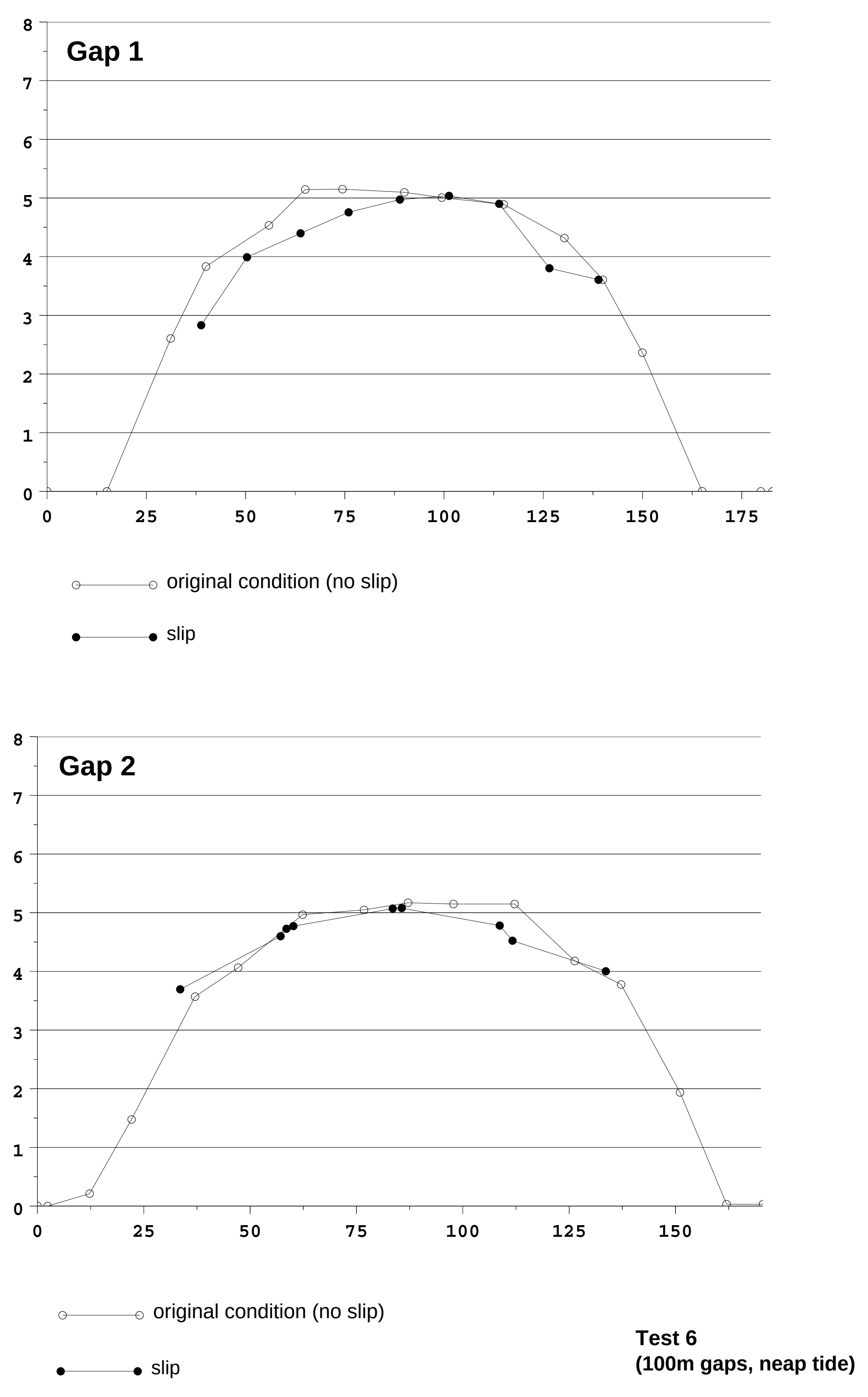

Figure 2.40 Speed profiles from north to south at peak flood. Test 6, in two different conditions

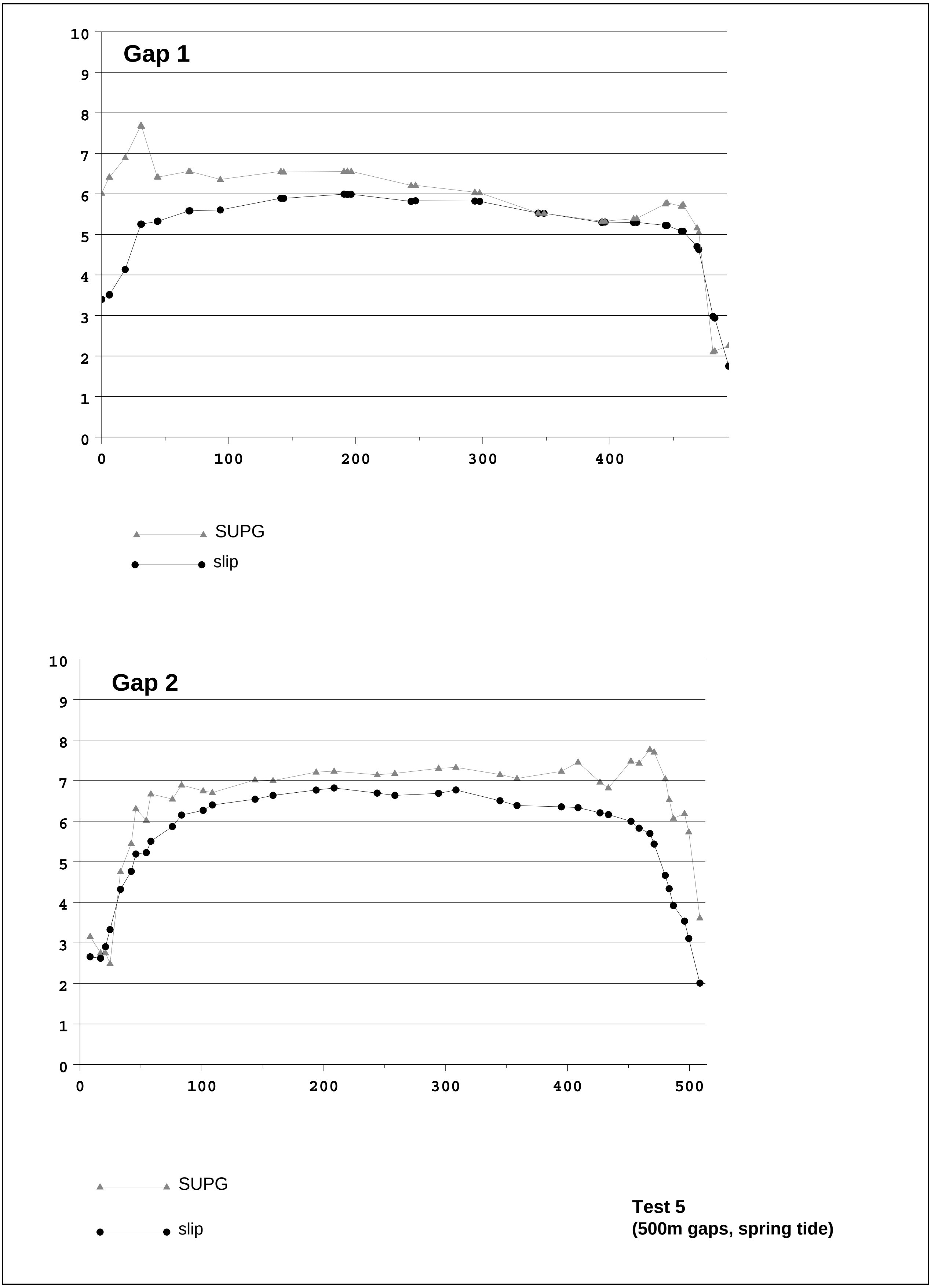

Test 5
(500m gaps, spring tide)

Figure 2.41 Comparison of SUPG vs slip condition, during the ebb tide, Test 5

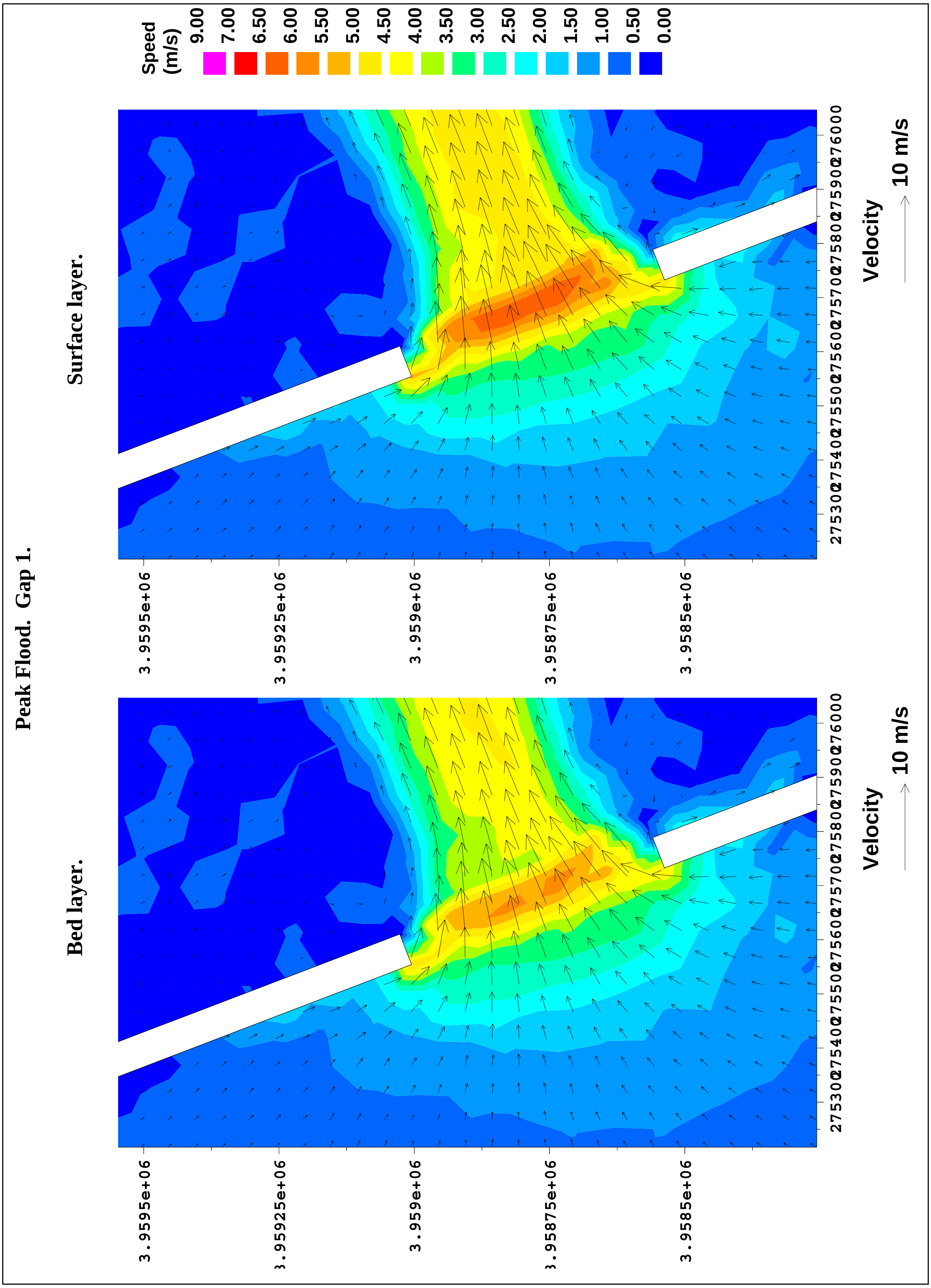

Figure 2.42 Current velocity vectors at peak flood. Gap 1. 3D simulation. 500 m gap width

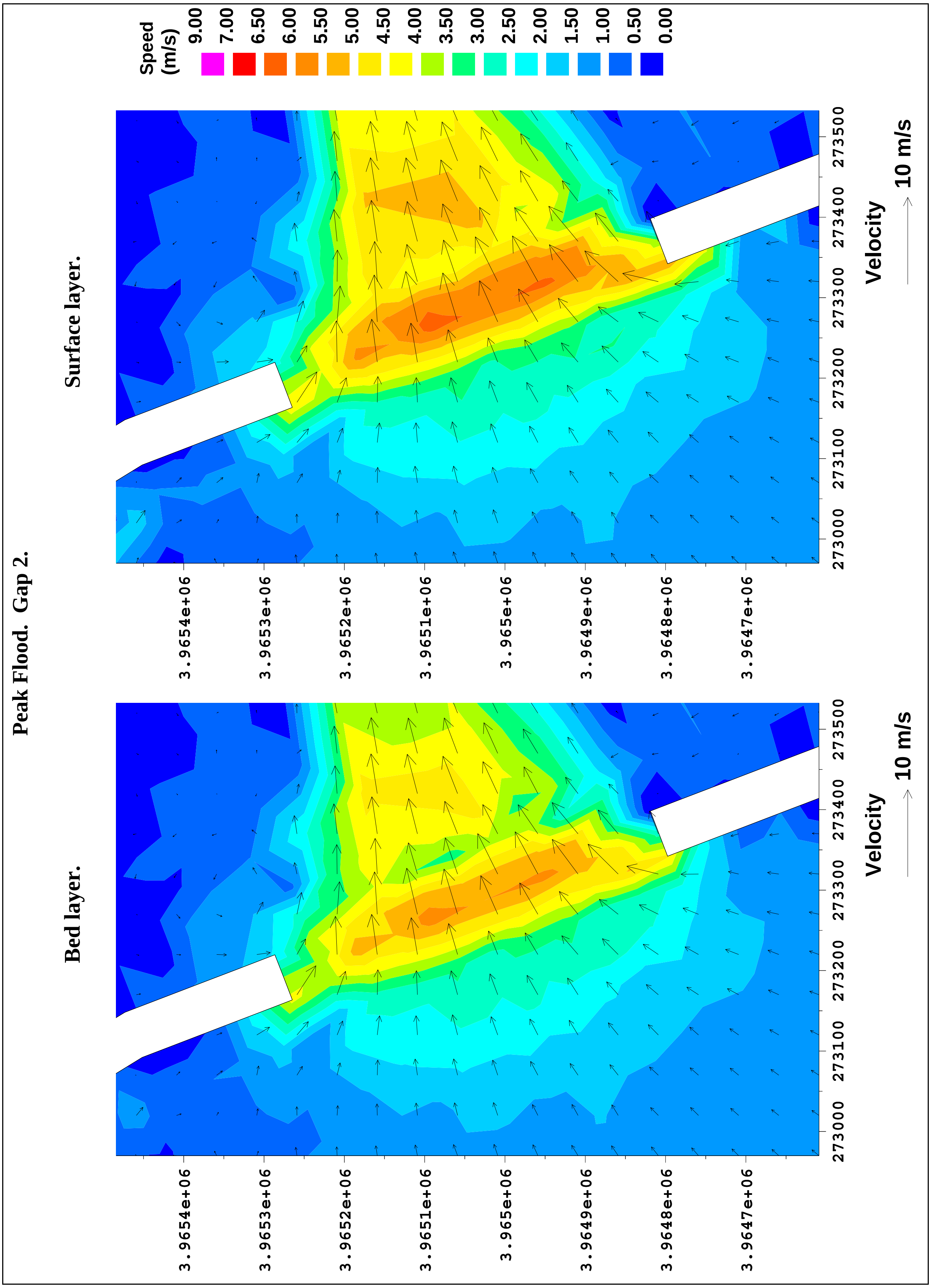

Figure 2.43 Current velocity vectors at peak flood. Gap 2. 3D simulation. 500 m gap width

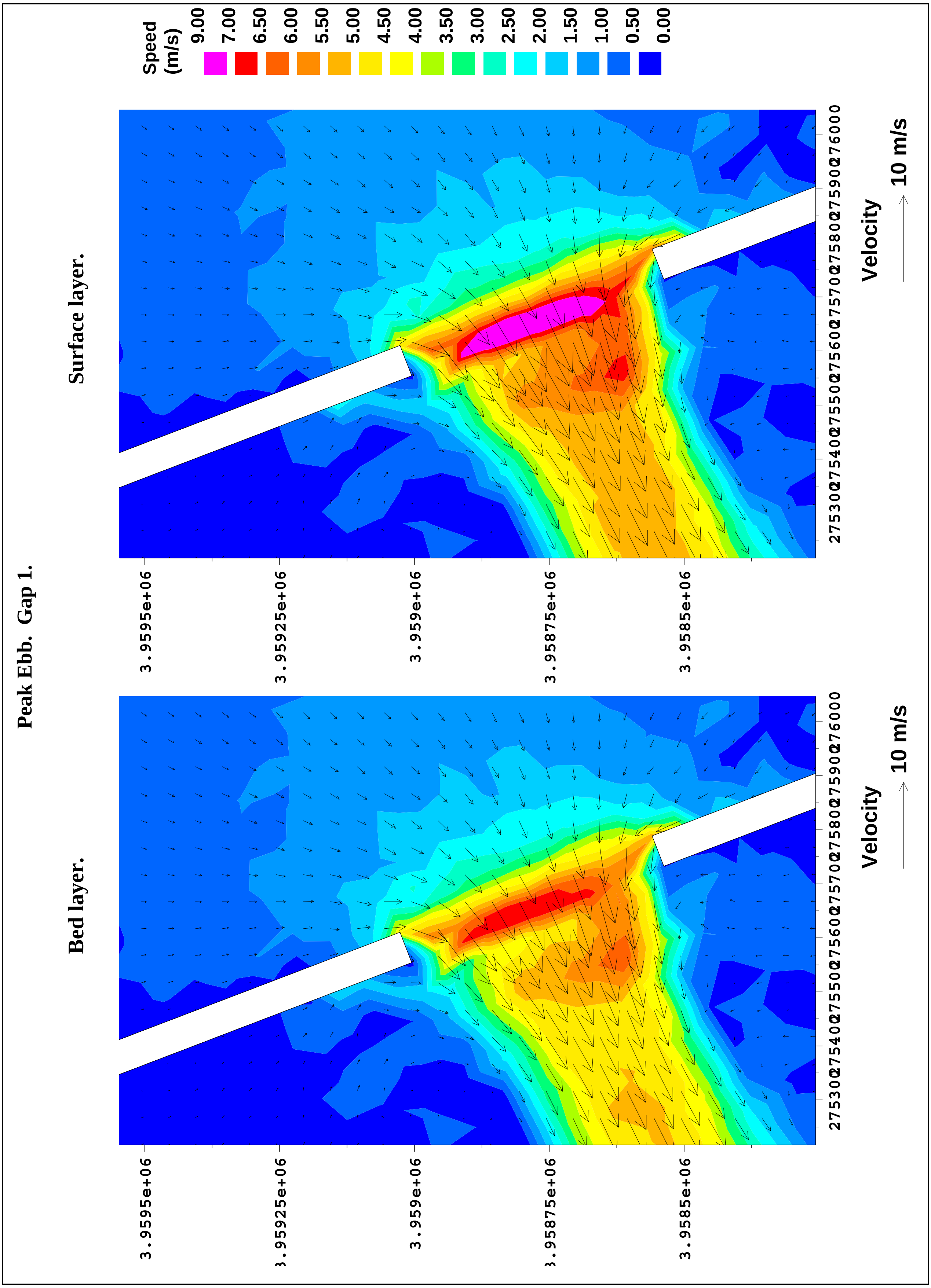

Figure 2.44 Current velocity vectors at peak ebb. Gap 1. 3D simulation. 500 m gap width

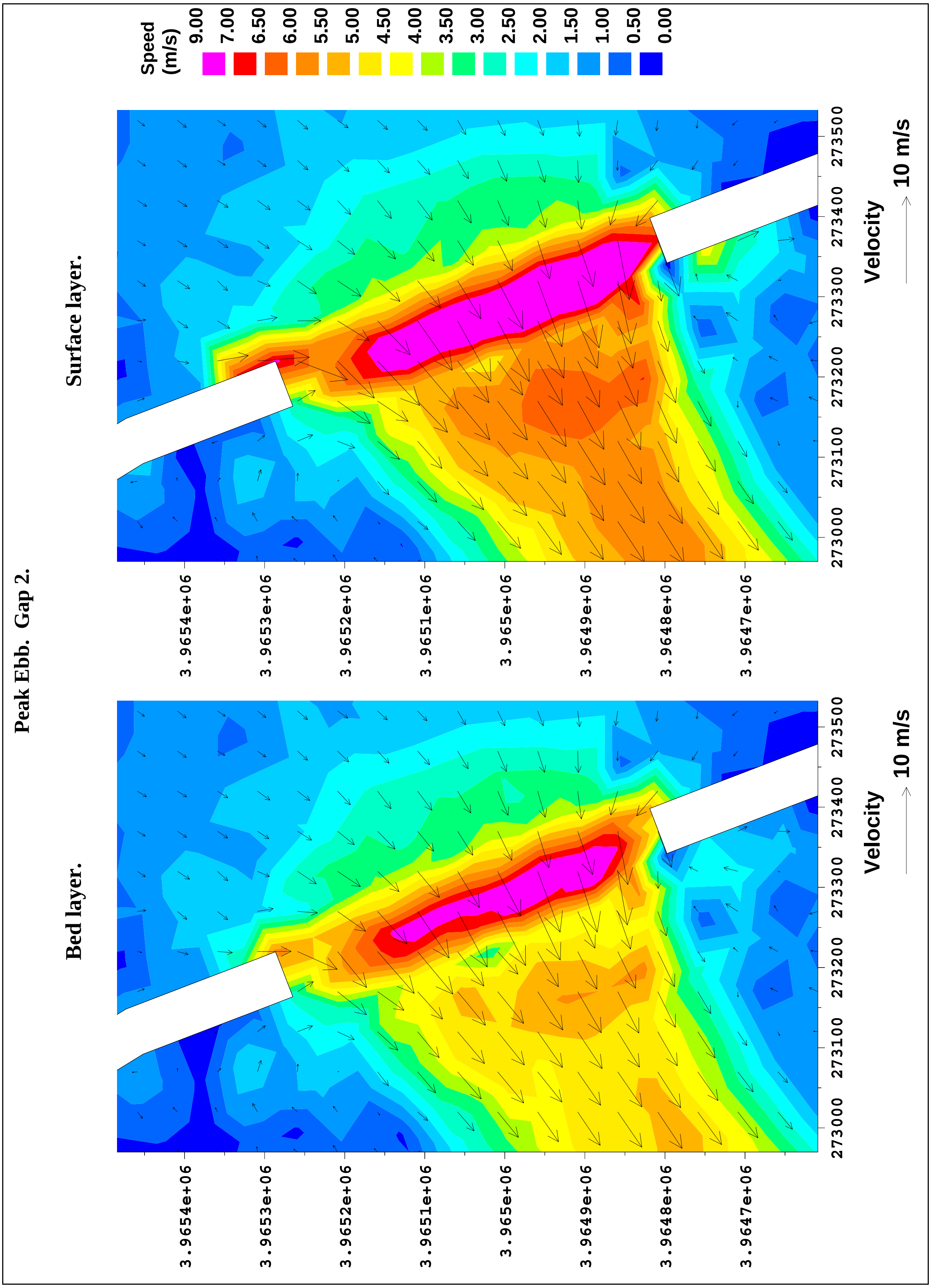

Figure 2.45 Current velocity vectors at peak ebb. Gap 2. 3D simulation. 500 m gap width

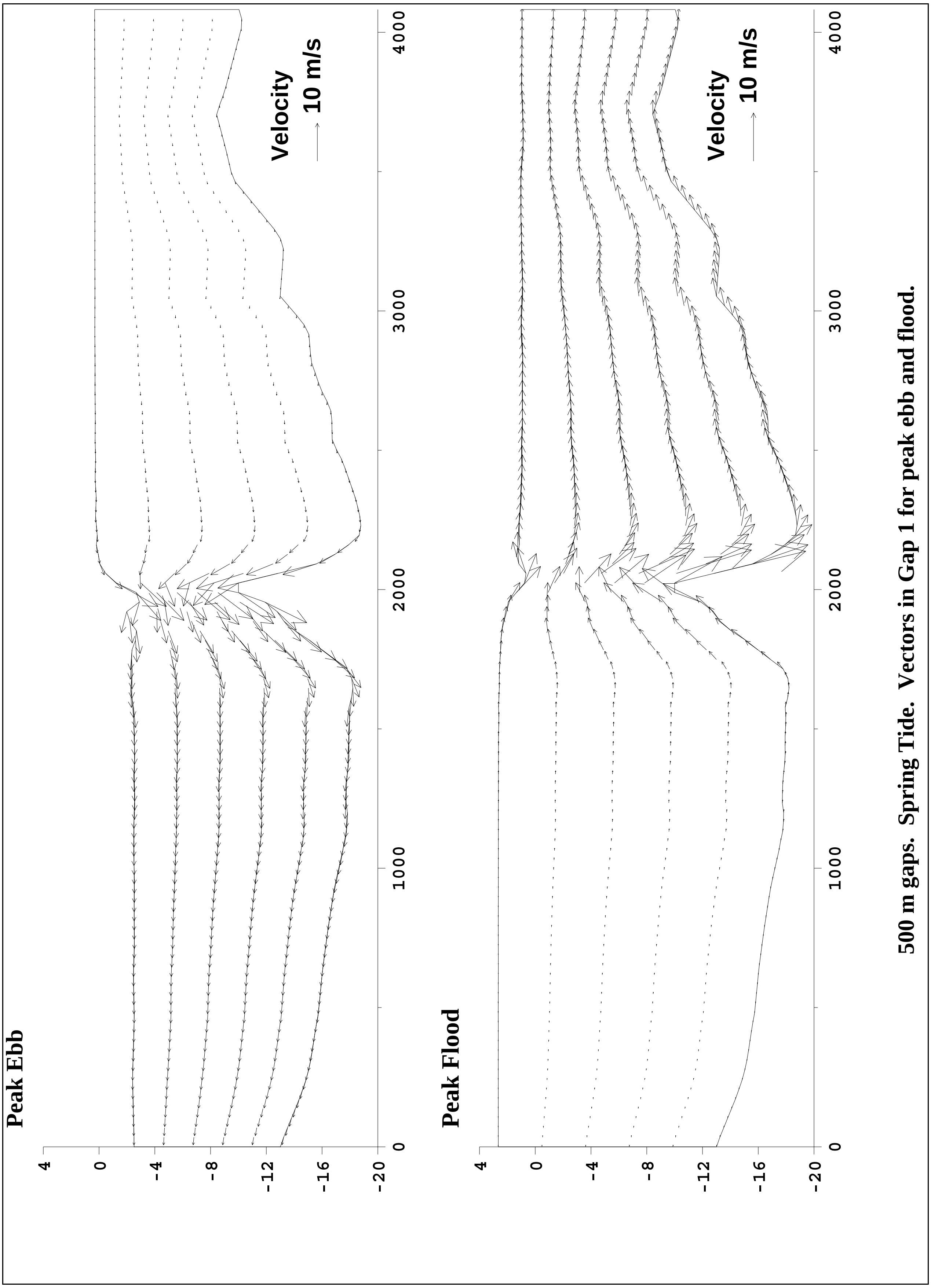

Figure 2.46 500 m gaps. Spring Tide. Vectors in gap 1 for peak flood and peak ebb

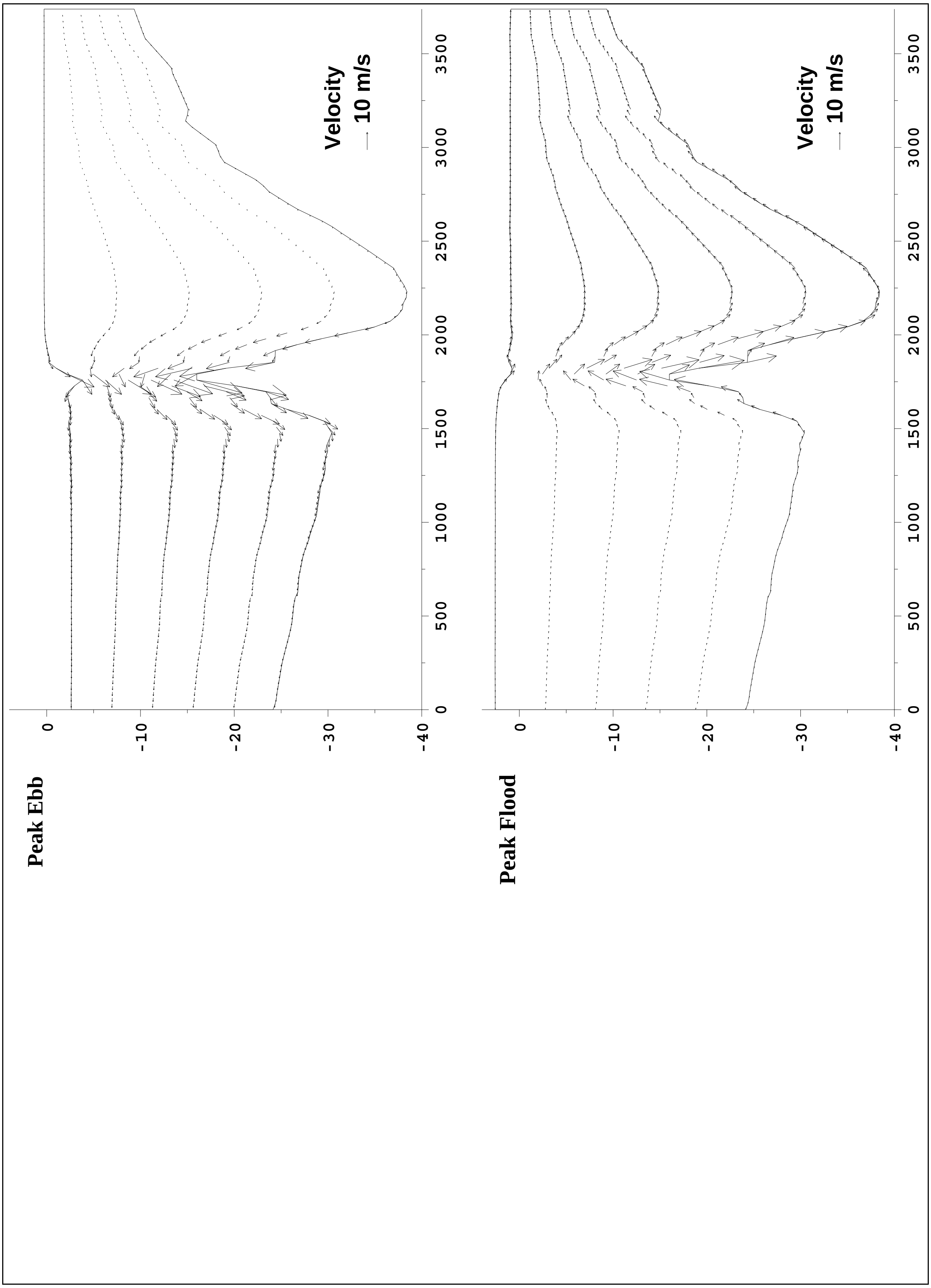

Figure 2.47 500 m gaps. Spring Tide. Vectors in gap 2 for peak flood and peak ebb

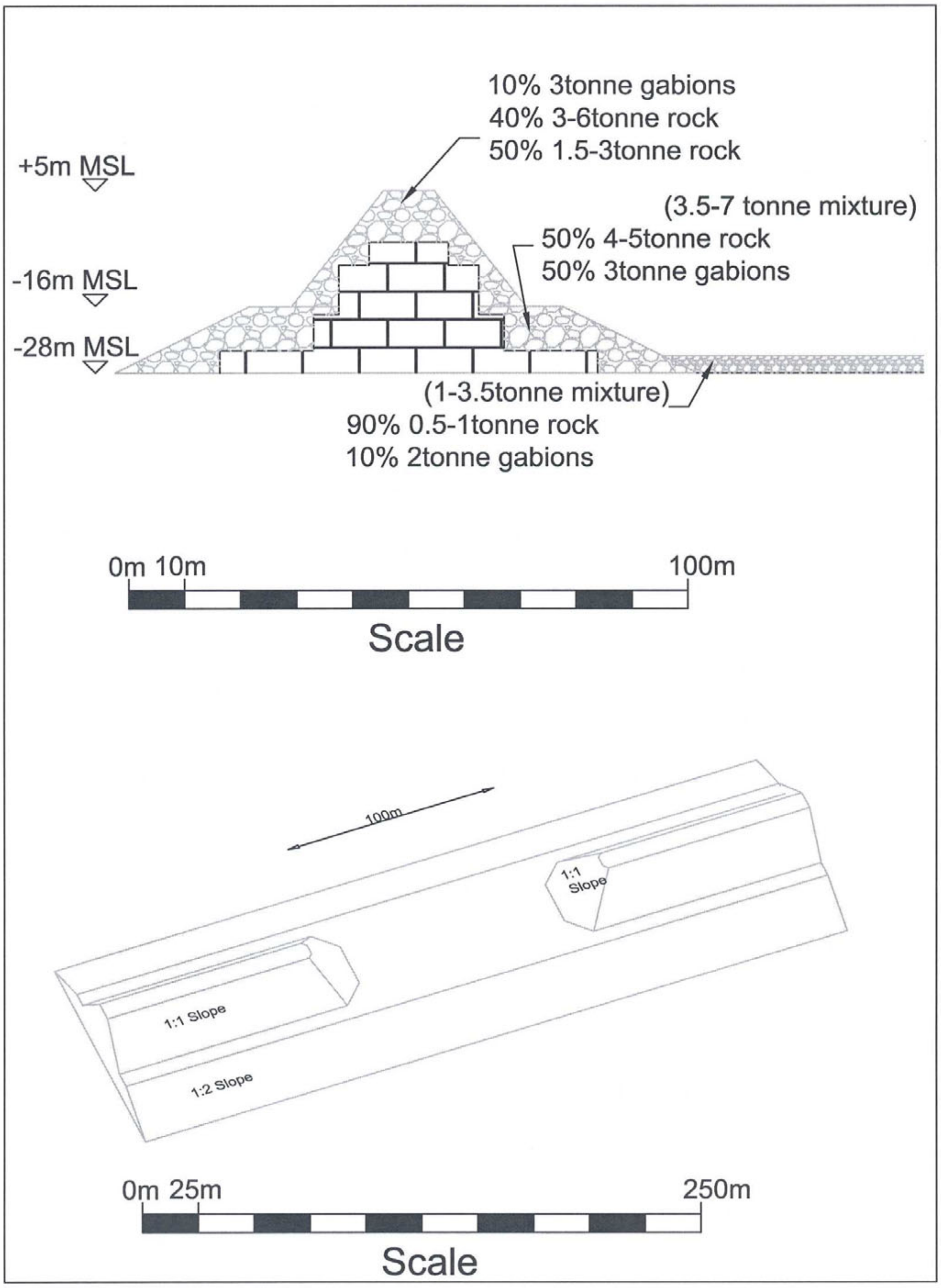

Figure 3.1 Schematised model details

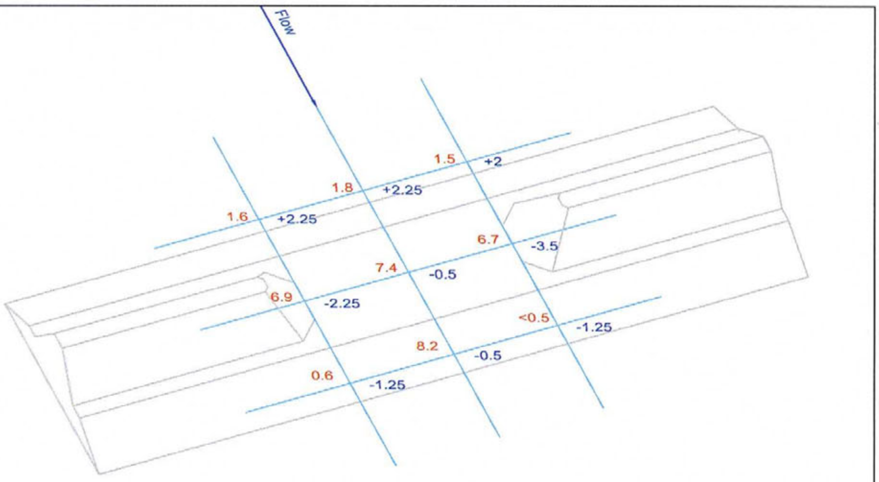

Current speeds and water levels during peak spring tide conditions (50m matrix)

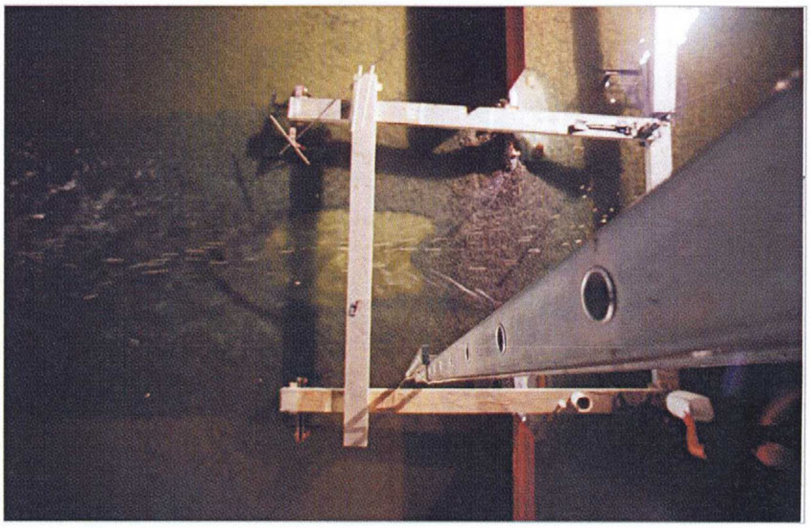

Surface float tracks

Figure 3.2 Summary of peak spring tide conditions

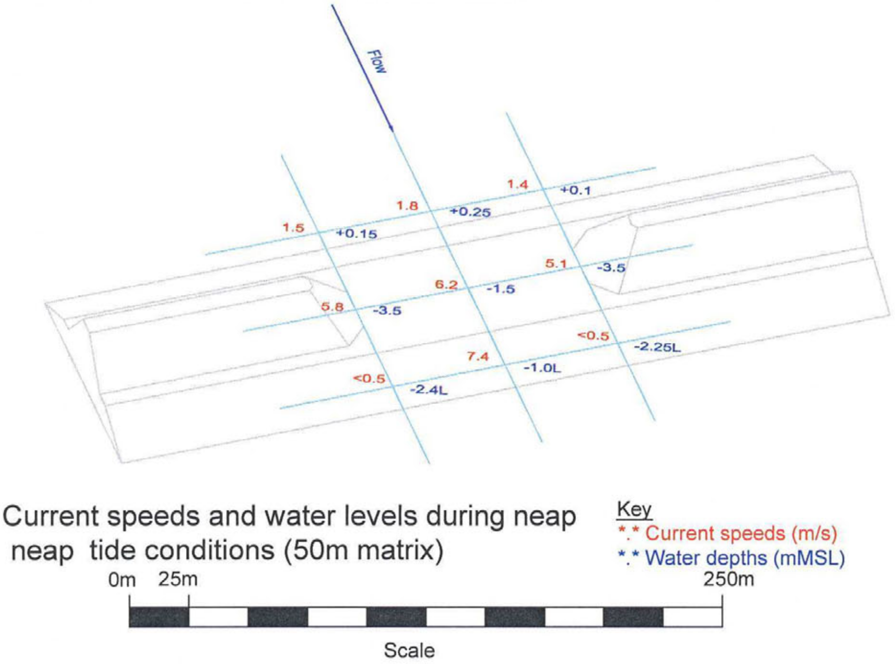

Current speeds and water levels during neap neap tide conditions (50m matrix)

Surface float tracks

Note: Scour of bed protection shown in photograph arose from previous test using spring tide conditions.

Figure 3.3 Summary of peak neap tide conditions

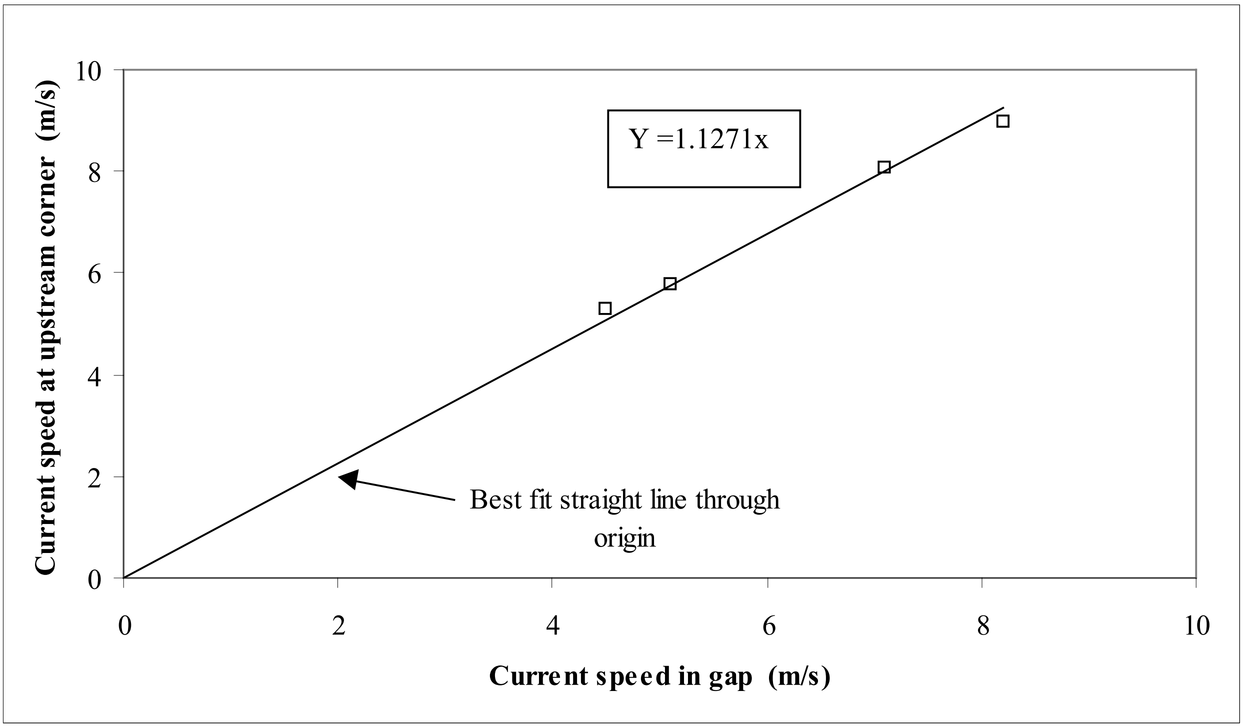

Figure 3.4 Relationship between current speed in centre of gap and at corner of gap

Plates

Plate 3.1 Simulated end dumping of single gabions

Plate 3.2 Flow contraction in closure gap

Plate 3.3a   Results of single gabion placement

Plate 3.3b   Results of single gabion placement

Appendices

Appendix 1

Telemac 2-D Model Description

Appendix 1 TELEMAC-2D Model Description

Description of model and main areas of application

TELEMAC-2D is a sophisticated flow model, which was originated by LNH in Paris, for free surface flows. It solves the 2D depth-integrated shallow water equations which are used to model flows in rivers, estuaries and seas. It uses finite element techniques so that very flexible unstructured triangular grids can be used. It has been developed under a quality assurance system including the application of a standard set of validation tests.

The model can simulate depth integrated tidal flows in estuaries and seas including the presence of drying banks. It can also simulate flows in rivers including turbulence structures resulting from flow obstructions and transcritical flows. The model has been used with up to 30000 elements.

The advantage of using finite elements lies primarily in the possibility of using a very flexible grid. This is much superior to using an orthogonal curvilinear grid as the user has far more complete control over grid refinement with a finite element system.

The applications of TELEMAC have included studies of ports, coastal management, floods in rivers, cooling water dispersion and infill of navigation channels.

Theoretical background and solution methods

TELEMAC solves the shallow water equations on an unstructured finite element grid (usually with triangular elements). The various variables (bed elevation, water depth, ∇ free surface level u and v velocity components) are defined at the nodes (vertices of triangles) and linear variation of the water and bed elevation and of the velocity within the triangles is assumed.

When the model is used a timestep is chosen and the computation is advanced for the required number of timesteps. There is no particular limit on the timestep for a stable computation but it is best to ensure that the Courant number based on propagation speed is less than about 10. It is found that if the solution is nearly steady then few computational iterations are required at each step to achieve the required level of accuracy, which in TELEMAC is computed according to the actual divergence from the accurate solution. The computation at each timestep is split into two stages, an advective step and a propagation-diffusion step.

The advective step

The advective step is computed using characteristics or streamwise upwind Petrov-Galerkin. The characteristic step makes it possible for the code to handle such problems as flow over a bump giving rise to locally supercritical flow and eddies shedding behind flow obstructions.

The propagation/diffusion step

The finite element method used is based on a Galerkin variational formulation. The resulting equations for the nodal values at each timestep are solved using an iterative method based on pre-conditioned conjugate gradient (pcg) methods so that large problems are solved efficiently. Several pcg solvers are coded and a selection is available to the user. The complete matrix is not assembled, rather an element by element method is used so that most of the operations are carried out on the element matrices; this is computationally more efficient, both in speed of execution and in memory requirements. Rather than using Gauss quadrature exact analytical formulae are used for the computation of matrices. A symbolic software was used to draw up the formulae used. The software makes it possible to carry out a second iteration of the solution at each timestep in order to represent the nonlinear terms in a time centred way, otherwise these terms are treated explicitly.

Boundary conditions

Boundary conditions are applied at solid boundaries where a zero normal flow and slip or nonslip boundary condition are applied. At open boundaries a selection of possibilities can be invoked depending on whether the flow is subcritical or supercritical or whether a wave absorbing boundary using a Riemann invariant is needed. A water discharge along a boundary segment can also be applied and the software distributes the flow along the segment chosen. This facility is valuable when running models of river reaches and the discharge in a cross section may be known rather than the velocity at each point in the cross-section.

Grid selection

The model can be run with a Cartesian grid for modelling rivers, estuaries and small areas of sea, with the possibility to apply a uniform Coriolis parameter, or on a spherical grid for larger areas of sea in which case the Coriolis parameter is computed from the latitude at each node. The effect of a wind blowing on the water surface and causing a setup or wind induced current or of an atmospheric pressure variation causing an inverted barometer effect can be included, as can a k-epsilon model of turbulence if required.

Friction

The bed friction can be specified via a Chezy, Strickler or linear coefficient, or a Nikuradse roughness length. A variable friction coefficient over the model area is a possibility. Sidewall friction can also be included if wanted. Viscosity can be imposed as a given eddy viscosity value or a k-epsilon model can be used if needed.

Tracer calculation

TELEMAC-2D includes also the capability to simulate the transport of a tracer substance. The tracer is again computed using an advective step followed by a propagation/diffusion step. Tracer boundary conditions can be applied at model inflow boundaries. The tracer calculation has been used in order to simulate cooling water dispersion and mud transport. Sources of water and/or of tracer can be specified in terms of the discharge required and the x and y coordinates of the location.

INPUTS

TELEMAC requires as input a finite element grid of triangles covering the area to be modelled. Bathymetric data from which the bed elevation at each node can be computed is also required covering the area. A file of keyword values is used to steer the computation (supplies bed roughness, timestep, duration of run etc).

Methods of inputting the data

The finite element grid that may be provided by a standard FE grid generator such as I-DEAS or SIMAIL. The software STBTEL (part of the TELEMAC suite) is used to read the output file from the grid generation software. The bathymetry is input using a digitising tablet and the SINUSX software is used to capture the bathymetry data. The data is stored in a form to be read into the TELEMAC system and depths interpolated to the model nodes.

Methods of checking and amending input data

SINUSX is a powerful interactive graphical software that can be used to check and amend the input data. Bathymetric curves can be duplicated, deleted, smoothed, moved etc.

User interface

A steering file editor EDAMOX with online help is available to edit the keyword steering file for TELEMAC. This software can be used to edit the keywords for any part of the TELEMAC system. It can check on the correctness of keyword values supplied. A study manager for TELEMAC is expected at the end of 1994.

Time to setup/calibrate/run/amend model

This depends on the form in which the data is supplied. Typically 1-2 days to digitise the chart data and 1-2 days to create the finite element grid. Boundary conditions may take a day to prepare. A run may take 1 to 5 hours to run a tide (for a 2000 cell model). The duration of the calibration process is hard to generalise as it depends entirely on particular circumstances.

OUTPUTS

Output parameters

The user can select from a range of output parameters including u and v velocity, u and v discharge, water level, bed level, water depth, tracer concentration and Froude number.

Output files

The TELEMAC output is contained in a single binary file which can be input to the graphics post-processor RUBENS. A listing file contains reflection of the input keywords and information on timestep reached, number of iterations to convergence etc. This file can be used to monitor the progress of a run.

Output plots

Results from any part of the TELEMAC system are processed using the interactive graphics system RUBENS. This is a powerful and friendly environment where colour and black and white figures can be produced interactively. By pointing and clicking time history plots, cross sections, vector plots and contour plots of any parameter at any position can be produced. Moreover parameters other than those input can be calculated in RUBENS and plotted.

HARDWARE REQUIREMENTS

TELEMAC is available on UNIX workstations SUN/HP and DEC. RUBENS requires 8Mb of RAM to run but performance is greatly enhanced with 12Mb. RUBENS and SINUSX can be run using either Open Windows or X Windows.

GENERAL

Interaction and compatibility of the model with other models

The main modules apart from TELEMAC-2D itself (the 2D flow model code) are SINUSX and RUBENS (described above).

The TELEMAC suite includes a bed load transport model (TSEF) and a suspended load model (SUBIEF). Also a wave model ARTEMIS that solves the mild slope equation.

The TELEMAC modelling suite also includes a quasi-3D random walk model for pollution transport modelling and a detailed water quality model with many water quality parameters including dissolved oxygen balance and particulates.

Quality Assurance

The software has been developed under the quality assurance procedures required by the French Electricity Industry. This has included the production of an extensive dossier of validation tests.

Validation

Validation tests on TELEMAC include:

Simulation of the eddies produced behind bridge piers. This test case includes the ability of the model to produce an unsteady solution from steady boundary conditions (von Karman vortex street).

Drying on a beach

Simulation of the tides on the continental shelf including the Bay of Biscay. This model has been closely compared with the observed tides at coastal sites.

Flow over a step in the bed with critical flow and a hydraulic jump. This solution is compared with the analytically known solution to this problem.

Past and current users

Bristol University Agriculture Department
Laboratoire Hydraulique de France
Forth River Purification Board
Franzius Institute
Port Autonome de St Nazaire

Projects where model has been used

Examples of recent projects where TELEMAC has been used at HR Wallingford are:

Location	Client	Date
Port Klang Marine Industrial Park	HICOM-Selangor	Sept 1993
Great Yarmouth Harbour	Great Yarmouth Harbour	May 1994
Southern North Sea	Crown Estate	July 1994
Harwich Harbour	Harwich Harbour Authority	June 1994
Blackwater Estuary	MAFF	May 1994
Dorset coast and the Solent	Poole Borough Council	May 1994
Firth of Forth	Forth River Purification Board	January 1994
Harwich/Felixstowe	Harwich Haven Authority	1995/96
Pipavav, India	Howe Consultants	
Dabhol, India	ENRON	1995
Alderney Harbour, UK	States of Guernsey	1996
Gwadar New Port, Pakistan	Karachi Port Trust	1996

Future developments and timescale for developments

Future developments of the TELEMAC system include TELEMAC-3D, a multilayer shallow water equation model using the same methodology as TELEMAC-2D. Also the TELEMAC study manager. Both are due at the end of 1994.

Appendix 2

The Numerical Model TELEMAC-3D

Appendix 2 The Numerical Model TELEMAC-3D

A. Malcherek [4] and J. M. Janin [5]

In this Appendix the TELEMAC-3D code used in the solution of the momentum and transport equations is described.

The 3D-shallow water and transport equations are given as:

$$\frac{\partial u}{\partial t}+u\frac{\partial u}{\partial x}+v\frac{\partial u}{\partial y}+w\frac{\partial u}{\partial z}=-\frac{1\partial p}{\rho\partial x}+\frac{\partial}{\partial x}\left(\upsilon_H\frac{\partial u}{\partial x}\right)+\frac{\partial}{\partial y}\left(\upsilon_H\frac{\partial u}{\partial y}\right)+\frac{\partial}{\partial z}\left(\upsilon_z\frac{\partial u}{\partial z}\right)+2\omega v\sin\phi \tag{1}$$

$$\frac{\partial v}{\partial t}+u\frac{\partial v}{\partial x}+v\frac{\partial v}{\partial y}+w\frac{\partial v}{\partial z}=-\frac{1\partial p}{\rho\partial y}+\frac{\partial}{\partial x}\left(\upsilon_H\frac{\partial v}{\partial x}\right)+\frac{\partial}{\partial y}\left(\upsilon_H\frac{\partial v}{\partial y}\right)+\frac{\partial}{\partial z}\left(\upsilon_z\frac{\partial v}{\partial z}\right)-2\omega u\sin\phi \tag{2}$$

$$\frac{\partial u}{\partial x}+\frac{\partial v}{\partial y}+\frac{\partial w}{\partial z}=0 \tag{3}$$

$$p=\rho_0 g(S-z)+\rho_o g\int_z^S\frac{\Delta\rho}{\rho_0}dz \tag{4}$$

$$\frac{\partial T}{\partial t}+u\frac{\partial T}{\partial x}+v\frac{\partial T}{\partial y}+w\frac{\partial T}{\partial z}=\frac{\partial}{\partial x}\left(v_{HT}\frac{\partial T}{\partial x}\right)+\frac{\partial}{\partial y}\left(v_{HT}\frac{\partial T}{\partial y}\right)+\frac{\partial}{\partial z}\left(v_{zT}\frac{\partial T}{\partial z}\right)+Q_T \tag{5}$$

where T can be the temperature or salinity or any other variable.

---

[4] Institut für Strömungsmechanik, Universität Hannover, Appelstr. 9A,30167 Hannover, FRG

[5] Diretion des Etudes at Recherches, Departement Laboratoire Nationale d'Hydraulique, E.D.F., 6, Quai Watier, B.P. 49, 78401 Chatou Cedex, France

1 Operator-Splitting

Operator-Splitting is based on the principal that the hyperbolic and the parabolic parts of the Navier-Stokes-equations should be treated separately in order to use well adapted numerical methods for each part. This implies that the hyperbolic part i.e., the advection terms are treated using characteristic methods, and the parabolic part i.e., the diffusion terms using finite elements.

Given the solution at $t=t^n$, we compute the solution at $t^{n+1}=t^n+\Delta t$. The numerical method solves the equations by means of a decomposition into sequential steps (i.e., we split the operators) and each numerical operator is treated by the appropriate method. The solution involves three steps: the advection step, the diffusion step, and the free surface-continuity-pressure step. The time derivatives are thus written as follows:

$$\frac{\partial f}{\partial t}=\frac{f^{n+1}-f^{diff}}{\Delta t}+\frac{f^{diff}-f^{adv}}{\Delta t}+\frac{f^{adv}-f^{n}}{\Delta t} \qquad (6)$$

whereby f can be u, v or T and

f^{n+1}	solution at t^{n+1}
f^{diff}	result of the diffusion step
f^{adv}	result of the advection step
f^{n}	solution at t^{n}

The Advection Step: In the advection step, the equation

$$\frac{\partial f}{\partial t}+u\frac{\partial f}{\partial x}+v\frac{\partial f}{\partial y}+w\frac{\partial f}{\partial z}=0 \qquad (7)$$

is solved using the method of characteristics described in the following section.

The Diffusion Step: In the diffusion step, the equation

$$\frac{\partial f}{\partial t}=\frac{\partial}{\partial x}\left(\upsilon_H\frac{\partial f}{\partial x}\right)+\frac{\partial}{\partial y}\left(\upsilon_H\frac{\partial f}{\partial y}\right)+\frac{\partial}{\partial z}\left(\upsilon_z\frac{\partial f}{\partial z}\right) \qquad (8)$$

is treated using FEM with linear shape functions on prismatic elements. The results from the advection step generate the initial conditions.

For the transport of a variable T the calculation involves only these two steps. The hydrodynamics further requires

The Free Surface-Continuity-Pressure Step: in which the equations

$$\frac{\partial u}{\partial t}=-\frac{1}{\rho}\frac{\partial p}{\partial x} \qquad (9)$$

$$\frac{\partial v}{\partial t}=-\frac{1}{\rho}\frac{\partial p}{\partial y} \qquad (10)$$

$$p=\rho_0 g(S-z)+\rho_0 g\int_z^S\frac{\Delta\rho}{\rho_0}dz \qquad (11)$$

$$\frac{\partial u}{\partial x}+\frac{\partial v}{\partial y}+\frac{\partial w}{\partial z}=0 \qquad (12)$$

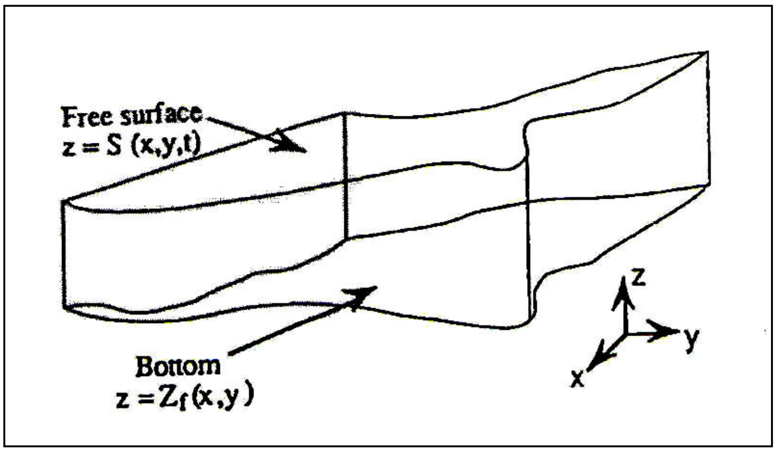

Figure 1 **Computation Domain**

are solved. The movement of the free surface is calculated using the FEM-code TELEMAC-2D (Galland et al, 1991) which solves the depth-integrated equations. In this particular application the full potential of the code is not required, since diffusive and advective terms are not found in this form of the integrated equations.

Once the horizontal velocities, the pressure and the free surface are known, the vertical velocities can be calculated by solving the continuity equation.

Stability is the most important advantage of this method. The entire method is stable if all the fractional steps are stable. The greatest disadvantage is the fact that the method is only of first order accuracy in time even if second order numerical methods like the Crank-Nicholson-scheme are applied in each fractional step. This behaviour is associated with the non-commutativity of the different fractional steps Malcherek, 1995.

2 Space discretization and σ- transformation

The domain to be studied is bounded by a bottom defined as $z = Z_f(x, y)$, a free surface $z = S(x, y)$ and on the sides by a vertical cylinder.

The spatial domain is discretized using prismatic finite elements with vertical quadrangular sides. The interpolation is such that it is linear when restricted to prismatic triangles or quadrangles. In fact computation is hardly ever done on the real prisms since a transformation is made to a reference prism of a much simpler shape. Note that since the prisms in TELEMAC-3D have vertical quadrangular sides the mapping is simpler than if the prisms were truly three-dimensional. The basis functions on the isoparametric reference prisms are expressed as follows (Dhatt and Touzot, 1983):

$$\psi_1=(1-\alpha-\beta)\left(\frac{1-\gamma}{2}\right) \qquad (13)$$

$$\psi_2=\alpha\left(\frac{1-\gamma}{2}\right) \qquad (14)$$

$$\psi_3=\beta\left(\frac{1-\gamma}{2}\right) \qquad (15)$$

$$\psi_4 = (1 - \alpha - \beta)\left(\frac{1+\gamma}{2}\right) \tag{16}$$

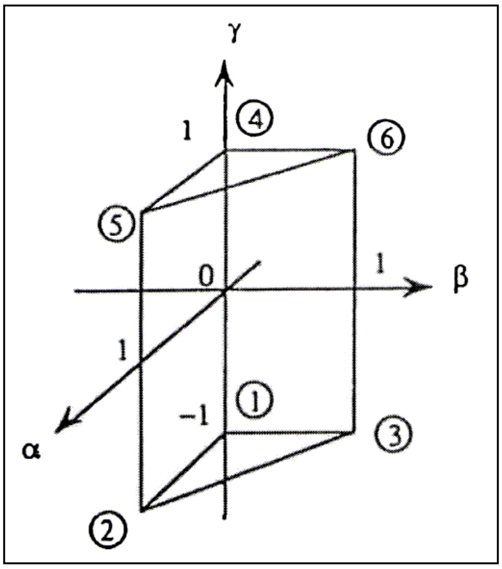

Figure 2 **Reference prism (circled numbers show the local numbering)**

$$\psi_5 = \alpha\left(\frac{1+\gamma}{2}\right) \tag{17}$$

$$\psi_6 = \beta\left(\frac{1+\gamma}{2}\right) \tag{18}$$

Because prisms with vertical quadrangular sides are used, the horizontal 2D projection of the mesh results in triangles, one of the finite element types used by TELEMAC-2D. Note that since TELEMAC-2D can also use quadrangles, a brick could have been used as a finite element for TELEMAC-3D. It is, however, easier to mesh complicated domains with triangles than with quadrangles.

The 3D mesh is generated by reproducing the 2D horizontal mesh along the vertical. Thus, for every point M(x, y) of the 2D mesh, we define several points N(x, y, z) for which:

$$z = Z_f(x,y) + \Theta(S(x,y,t) - Z_f(x,y)) \quad \text{with} \quad 0 \le \Theta \le 1 \tag{19}$$

The choice of the Θ values is made by the user, with no special requirements except that the bottom corresponds to $\Theta = 0$ and the free surface to $\Theta = 1$ (Figure 3).

Due to the free surface, the 3D mesh and thus the co-ordinate z of any point in the mesh is time-dependent. It is, however, possible to work on a mesh independent of time when a change of variables is used. One classical method is to switch from z to z* according to the σ – transformation:

$$z^* = \overline{S}\frac{z - Z_f(x,y)}{S(x,y,t) - Z_f(x,y)} \tag{20}$$

where $\overline{S}$ is a given positive constant. The corresponding mesh will be called afterwards the σ –mesh, which consists of the nodes $N^*\left(x, y, z^* = \Theta\overline{S}\right)$.

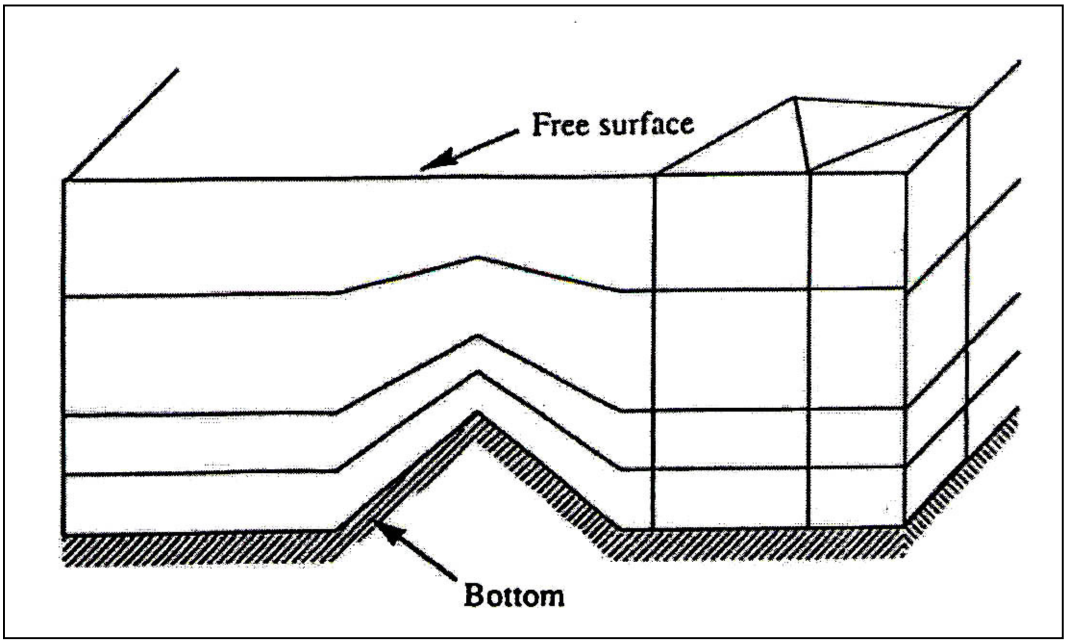

Figure 3 Schematic view of a mesh consisting of 5 planes (Θ = 0,1/6, 1/3, 2/3, 1)

3 The movement of the free surface

Since hydrostatic pressure is assumed, the vertical velocity w is only needed for the advection step. What is in fact required is w*. Therefore, it is advantageous to compute w* directly by solving the continuity equation in the σ –mesh.

Expressed in the set of co-ordinates (x, y, z*, t), the continuity equation is:

$$\left(\frac{\partial h}{\partial t}\right)_{x,y}+\left(\frac{\partial (hu)}{\partial x}\right)_{y,z^*,t}+\left(\frac{\partial (hv)}{\partial y}\right)_{x,z^*,t}+h\left(\frac{\partial w^*}{\partial z^*}\right)_{x,y,t}=0 \qquad (21)$$

The vertical velocity, w*, is known at the bottom and at the free surface where it is either equal to zero in case of an impermeable boundary or to any set value in the case of an inflow or outflow at the bottom or at the free surface. The latter case is encountered, for instance, in the study of thermal plumes.

Equation (21) integrated along the vertical between 0 and z* and between z* and $\bar{S}$ yields:

$$z^*\left(\frac{\partial h}{\partial t}\right)_{x,y}+\int_0^{z^*}\left[\left(\frac{\partial (hu)}{\partial x}\right)_{y,z^*,t}+\left(\frac{\partial (hv)}{\partial y}\right)_{x,z^*,t}\right]dz^*+h\left[w^*(z^*)-w^*(0)\right]=0 \qquad (22)$$

and

$$\left(z^*-\bar{S}\right)\left(\frac{\partial h}{\partial t}\right)_{x,y}+\int_{\bar{S}}^{z^*}\left[\left(\frac{\partial (hu)}{\partial x}\right)_{y,z^*,t}+\left(\frac{\partial (hv)}{\partial y}\right)_{x,z^*,t}\right]dz^*+h\left[w^*(z^*)-w^*(\bar{S})\right]=0 \qquad (23)$$

Recall that w*(0) and w* ($\bar{S}$) are known. By combining (22) and (23), we obtain equation (24) which satisfies both boundary conditions at z* = 0 and z* = $\bar{S}$:

$$\begin{aligned} h\bar{S}w^*(z^*) &= h(\bar{S}-z^*)w^*(0) + hz^*w^*(\bar{S}) \\ &\quad + z^* \int_0^{\bar{S}} \left[\left(\frac{\partial(hu)}{\partial x} \right)_{y,z^*,t} + \left(\frac{\partial(hv)}{\partial y} \right)_{x,z^*,t} \right] dz^* \\ &\quad - \bar{S} \int_0^{z^*} \left[\left(\frac{\partial(hu)}{\partial x} \right)_{y,z^*,t} + \left(\frac{\partial(hv)}{\partial y} \right)_{x,z^*,t} \right] dz^* \end{aligned} \tag{24}$$

Note also that no time discretization is required to solve (24) contrary to (22) or (23). Apart from the advantage of correctly simulating free surface movement, the σ –mesh allows fast and simple computations due to its regularity.

4 The advection step

In the advection step the following equation has to be solved:

$$\frac{\partial f}{\partial t} + u\frac{\partial f}{\partial x} + v\frac{\partial f}{\partial y} + w\frac{\partial f}{\partial z} = 0 \tag{25}$$

On the characteristic curve defined by

$$\frac{\partial x}{\partial t} = u \qquad \frac{\partial y}{\partial t} = v \qquad \frac{\partial z}{\partial t} = w \tag{26}$$

the advection equation can be written as

$$\frac{\partial f}{\partial t} = 0 \tag{27}$$

The problem is solved with an inverse formulation (Benque et al. 1980) i.e. the characteristic curve starts from the node $\left(x_i^{n+1}, y_i^{n+1}, z_i^{n+1}, t^{n+1}\right)$ at the time step to be calculated. Backward in time it crosses the time level t^n at the base point (x_i^b, y_i^b, z_i^b, t^n). The base point can then be calculated by integrating the differential equations of the characteristics. Using the trapezoidal rule:

$$x_i^b = x_i - \frac{1}{2}\left(u_i^b + u_i^{n+1}\right)\Delta t \tag{28}$$

$$y_i^b = y_i - \frac{1}{2}\left(v_i^b + u_i^{n+1}\right)\Delta t \tag{29}$$

$$z_i^b = z_i - \frac{1}{2}\left(w_i^b + u_i^{n+1}\right)\Delta t \tag{30}$$

Unfortunately the velocities at the base point and, therefore, at the new time step are not known and an iterative procedure must be applied.

In TELEMAC-3D a predictor-corrector-scheme is used. In the predictor, the base points of the characteristics are calculated using the velocities u_i^n. After all of the fractional steps are executed, the corrector calculates the base points of the characteristics from:

$$x_i^b = x_i - \left(\left(1-\theta\right)u_i^n + \theta u_i^{n+1}\right)\Delta t \tag{31}$$

$$y_i^b = y_i - \left(\left(1-\theta\right)v_i^n + \theta u_i^{n+1}\right)\Delta t \tag{32}$$

$$z_i^b = z_i - \left(\left(1-\theta\right)w_i^n + \theta u_i^{n+1}\right)\Delta t \tag{33}$$

In most cases the base point of the characteristic curve will not intersect the mesh at a node. The value at the base of the characteristic must, therefore, be interpolated from the surrounding nodes using an interpolation scheme or a FEM approximation (Li and Chen, 1989).

When the value f_i^b at the base of the characteristic curve in known, the value at the new time step t^{n+1} is given as:

$$f_i^{n+1} = f_i^b \tag{34}$$

TELEMAC-3D solves the advection equation as the σ –transformed mesh. Each variable f on the real mesh is given on the σ –mesh as:

$$f\,(x, y, z, t) = f\,(x, y, z^*(x, y, z, t),t) \tag{35}$$

Therefore, first order derivatives transform according to:

$$\frac{\partial f}{\partial t} = \frac{\partial f}{\partial t} + \frac{\partial f}{\partial z^*}\frac{\partial z^*}{\partial t} \tag{36}$$

$$\frac{\partial f}{\partial x} = \frac{\partial f}{\partial x} + \frac{\partial f}{\partial z^*}\frac{\partial z^*}{\partial x} \tag{37}$$

$$\frac{\partial f}{\partial y} = \frac{\partial f}{\partial y} + \frac{\partial f}{\partial z^*}\frac{\partial z^*}{\partial y} \tag{38}$$

$$\frac{\partial f}{\partial z} = \frac{\partial f}{\partial z^*}\frac{\partial z^*}{\partial z}, \tag{39}$$

where derivatives on the left hand side of the equations are in the real, and on the right hand side in the σ – transformed mesh. Therefore, the advection equation on the σ – transformed mesh is given as:

$$\frac{\partial f}{\partial t} + u\frac{\partial f}{\partial x} + v\frac{\partial f}{\partial y} + \left(\frac{\partial z^*}{\partial t} + u\frac{\partial z^*}{\partial x} + v\frac{\partial z^*}{\partial y} + w\frac{\partial z^*}{\partial z}\right)\frac{\partial f}{\partial z^*} = 0 \tag{40}$$

setting

$$w^* = \frac{dz^*}{dt} = \frac{\partial z^*}{\partial t} + u\frac{\partial z^*}{\partial x} + v\frac{\partial z^*}{\partial y} + w\frac{\partial z^*}{\partial z} \tag{41}$$

this equation reduces to

$$\frac{\partial f}{\partial t} + u\frac{\partial f}{\partial x} + v\frac{\partial f}{\partial y} + w^*\frac{\partial f}{\partial z^*} = 0 \tag{42}$$

5 The diffusion step

In the diffusion step, the equation

$$\frac{\partial f}{\partial t}=\frac{\partial}{\partial x}\left(v_x\frac{\partial f}{\partial x}\right)+\frac{\partial}{\partial y}\left(v_y\frac{\partial f}{\partial y}\right)+\frac{\partial}{\partial z}\left(v_z\frac{\partial f}{\partial z}\right)+Q_f \tag{43}$$

is solved using the results from the advection step as the initial condition. The time derivative is approximated using a Crank-Nicolson-scheme:

$$\begin{aligned}\frac{f^{diff}-f^{adv}}{\Delta t}=&\,\theta\left(\frac{\partial}{\partial x}\left(v_x\frac{\partial f^{n+1}}{\partial x}\right)+\frac{\partial}{\partial y}\left(v_y\frac{\partial f^{n+1}}{\partial y}\right)+\frac{\partial}{\partial z}\left(v_z\frac{\partial f^{n+1}}{\partial z}\right)\right)\\&+(1-\theta)\left(\frac{\partial}{\partial x}\left(v_x\frac{\partial f^{n}}{\partial x}\right)+\frac{\partial}{\partial y}\left(v_y\frac{\partial f^{n}}{\partial y}\right)+\frac{\partial}{\partial z}\left(v_z\frac{\partial f^{n}}{\partial z}\right)\right)+Q_f\end{aligned} \tag{44}$$

The diffusion step was originally solved on the real mesh using a standard Galerkin approach with the simplification that prisms without horizontal triangles are replaces by prisms of the same volume with horizontal triangles. Unfortunately this simplification leads to unacceptably bad results when large bottom gradients are present.

Therefore, the diffusion step is now solved in the σ –mesh where the transformation to the σ –mesh is given as:

$$\begin{aligned}\frac{\partial f}{\partial t}+\frac{\partial f}{\partial z^*}\frac{\partial z^*}{\partial t}=&\,\frac{\partial}{\partial x}v_x\left(\frac{\partial f}{\partial x}+\frac{\partial f}{\partial z^*}\frac{\partial z^*}{\partial x}\right)+\frac{\partial z^*}{\partial x}\frac{\partial}{\partial z^*}v_x\left(\frac{\partial f}{\partial x}+\frac{\partial f}{\partial z^*}\frac{\partial z^*}{\partial x}\right)\\&+\frac{\partial}{\partial y}v_y\left(\frac{\partial f}{\partial y}+\frac{\partial f}{\partial z^*}\frac{\partial z^*}{\partial y}\right)+\frac{\partial z^*}{\partial y}\frac{\partial}{\partial z^*}v_y\left(\frac{\partial f}{\partial y}+\frac{\partial f}{\partial z^*}\frac{\partial z^*}{\partial y}\right)\\&+\frac{\partial z^*}{\partial z}\frac{\partial}{\partial z^*}\left(v_z\frac{\partial f}{\partial z^*}\frac{\partial z^*}{\partial z}\right)\end{aligned} \tag{45}$$

The standard Galerkin procedure and integration by parts leads to the formulation now used in the TELEMAC-3D.

6 The free surface-continuity-pressure step

At this point, the advection and diffusion operators have been treated. By integration of the momentum and continuity equations along the vertical (between the bottom and the free surface) we obtain the classical shallow water equations without the advective and diffusive terms. Recall that this is possible because we suppose that the pressure is hydrostatic. This results in:

$$\frac{\partial h}{\partial t}+\frac{\partial(\overline{u}h)}{\partial x}+\frac{\partial(\overline{v}h)}{\partial y}+R=0 \tag{46}$$

$$\frac{\overline{u}_{n+1}-\overline{u}_{diff}}{\Delta t}+g\frac{\partial h}{\partial x}=-g\frac{\partial Z_f}{\partial x}=F_x \tag{47}$$

$$\frac{\overline{v}_{n+1}-\overline{v}_{diff}}{\Delta t}+g\frac{\partial h}{\partial y}=-g\frac{\partial Z_f}{\partial y}+F_y \tag{48}$$

with

$h = S-Z_f$	water height
R	source term due to any inlet or outlet of water at the bottom or at the free surface
$\bar{u}_{n+1}$	mean velocity along x at t_{n+1}
$\bar{v}_{n+1}$	mean velocity along y at t_{n+1}
$\bar{u}_{diff}$	velocity u_{diff} (diffusion result) averaged along vertical
$\bar{v}_{diff}$	velocity v_{diff} (diffusion result) averaged along vertical
F_x, F_y	buoyancy terms

Mean velocities are computed according to the formula:

$$\bar{u} = \frac{1}{(S - Z_f)} \int_{Z_f}^{S} u dz \tag{49}$$

The source term R reads:

$$R = \frac{h}{S}\left[w^*(\bar{s}) - w^*(0)\right] \tag{50}$$

Bouyancy terms are given by:

$$F_x = \frac{g}{S - Z_f} \int_{Z_f}^{S} \frac{\partial}{\partial x} \int_{z}^{S} \frac{\Delta\rho}{\rho_0} dz dz' \tag{51}$$

$$F_y = \frac{g}{S - Z_f} \int_{Z_f}^{S} \frac{\partial}{\partial y} \int_{z}^{S} \frac{\Delta\rho}{\rho_0} dz dz' \tag{52}$$

It is well known that the calculation of the bouyancy terms on σ-structured meshes has to be done very carefully in order to avoid numerical density currents (Janjic, 1977, Mesinger, 1982, Arakawa and Suarez, 1983, Haney, 1991). The vertical integration of the pressure term using the trapezoidal rule leads to:

$$\begin{aligned}
\frac{\partial p}{\partial x} &= g \frac{\partial}{\partial x} \int_{z}^{S_f} \Delta\rho dz \\
&= g \frac{\partial}{\partial x} \sum_{i=1}^{N-1} \int_{zi}^{zi+1} \Delta\rho z \\
&= g \frac{\partial}{\partial x} \sum_{i=1}^{N-1} \left[\frac{1}{2} (z_{i+1} - z_i)(\Delta\rho_{i+1} + \Delta\rho_i) \right]
\end{aligned}$$

Application of the product rule yields the following pressure term:

$$\frac{\partial p}{\partial x} = \frac{g}{2} \sum_{i=1}^{N-1} \left[\frac{\partial}{\partial x} (z_{i+1} - z_i)(\Delta\rho_{i+1} + \Delta\rho_i) + (z_{i+1} - z_i) \frac{\partial}{\partial x} (\Delta\rho_{i+1} + \Delta\rho_i) \right] \tag{53}$$

which has to be vertically averaged.

The integrated shallow water equations are solved in the TELEMAC-2D using finite element methods. As mentioned, one of the finite elements available is the triangle. That code has been written by also taking advantage of Element by Element methods (that is: no assembly of matrices, vectorizable matrix vector products…). Its computing cost is between 0.05 and 0.1 s per time step per thousand points on a vector computer. It is currently used in applications in ocean and river engineering (Hervouet, 1991 and 1992, Labadie, 1991). Note that we do not have to use the full potentiality of TELEMAC-2D since we do not have diffusive and advective terms in the integrated equations.

TELEMAC-2D yields the free surface S at t_{n+1}, which allows us to compute the pressure p_{n+1} and the horizontal components of the velocity u_{n+1}. w_{n+1} is then found by solving the continuity equation.

List of symbols

α,β,γ	co-ordinates in isoparametric space, used to simplify interpolation
Θ	fractional depth parameter
θ	parameter in Crank-Nicholson approximation for diffusion step
ρ	density
ρ_0	reference density
$\Delta\rho$	$\Delta\rho=\rho-\rho_0$
σ-mesh	three dimensional mesh obtained through σ-transformation
ϕ	latitude
$\psi_1 \ldots \psi_6$	basis functions used to define isoparametric reference prisms
ω	angular velocity of the Earth
f	general parameter; can be u, v or T
f^{adv}	result of the advection step
f^{diff}	result of the diffusion step
f^{n+1}	solution at t^{n+1}
f^{n}	solution at t^{n}
F_x, F_y	buoyancy terms
g	acceleration due to gravity
h	water depth, $h=S-Z_f$
M(x,y)	point on 2D mesh
N(x,y,z)	point on 3D mesh
N*(x,y,z*)	point on σ-mesh
p	pressure at the free surface
Q_f	flux term for f
R	source term
S	free surface S=z(x,y,t)
$\overline{S}$	constant in σ-transformation (positive)
t	time
T	any variable, such as temperature or salinity
Δt	timestep length
u,v,w	velocities in Cartesian directions (x,y,z)
$\overline{u}$	mean velocity in x-direction
$\overline{v}$	mean velocity in y-direction
v_H	horizontal eddy viscosity
v_{HT}	horizontal eddy diffusivity
v_z	vertical eddy viscosity
v_{zT}	vertical eddy diffusivity
w*	vertical velocity in σ-mesh
x,y,z	Cartesian co-ordinates
z*	vertical co-ordinate transformed according to the σ-transformation
Z_f	vertical co-ordinate of bottom